SANDIA REPORT
SAND2001-1292
Unlimited Release
Printed May 2001

Chemical reaction Mechanisms for Modeling the Fluorocarbon Plasma Etch of Silicon Oxide and Related Materials

Pauline Ho, Justine E. Johannes, Richard J. Buss, and Ellen Meeks

Prepared by
Sandia National Laboratories
Albuquerque, New Mexico 87185 and Livermore, California 94550

Sandia is a multiprogram laboratory operated by Sandia Corporation, a Lockheed Martin Company, for the United States Department of Energy under Contract DE-AC04-94AL85000.

Issued by Sandia National Laboratories, operated for the United States Department of Energy by Sandia Corporation.

Available to DOE and DOE contractors from
U.S. Department of Energy
Office of Scientific and Technical Information
P.O. Box 62
Oak Ridge, TN 37831

Telephone: (865)576-8401
Facsimile: (865)576-5728
E-Mail: reports@adonis.osti.gov
Online ordering: http://www.doe.gov/bridge

Available to the public from
U.S. Department of Commerce
National Technical Information Service
5285 Port Royal Rd
Springfield, VA 22161

Telephone: (800)553-6847
Facsimile: (703)605-6900
E-Mail: orders@ntis.fedworld.gov
Online order: http://www.ntis.gov/ordering.htm

SAND 2001-1292
Unlimited Release
Printed May 2001

Chemical Reaction Mechanisms for Modeling the Fluorocarbon Plasma Etch of Silicon Oxide and Related Materials

Pauline Ho
Chemical Processing Science Department

Justine E. Johannes
Multiphase Transport Processes Department

Richard J. Buss
Plasma/Aerosol/Non-Continuum Processes Department

Sandia National Laboratories
P.O. Box 5800
Albuquerque, NM 87185

Ellen Meeks
Reaction Design
6440 Lusk Blvd., Suite D209
San Diego, CA 92121

Abstract

As part of a project with SEMATECH, detailed chemical reaction mechanisms have been developed that describe the gas-phase and surface chemistry occurring during the fluorocarbon plasma etching of silicon dioxide and related materials. The fluorocarbons examined are C_2F_6, CHF_3 and C_4F_8, while the materials studied are silicon dioxide, silicon, photoresist, and silica-based low-k dielectrics. These systems were examined at different levels, ranging from in-depth treatment of C_2F_6 plasma etch of oxide, to a fairly cursory examination of C_4F_8 etch of the low-k dielectric. Simulations using these reaction mechanisms and AURORA, a zero-dimensional model, compare favorably with etch rates measured in three different experimental reactors, plus extensive diagnostic absolute density measurements of electron and negative ions, relative density measurements of CF, CF_2, SiF and SiF_2 radicals, ion current densities, and mass spectrometric measurements of relative ion densities.

Acknowledgments

We thank Drs. Greg Hebner and Paul Miller of Sandia National Laboratories, Prof. G. S. Oehrlein of the University of Maryland (previously of SUNY-Albany), Prof. H. M. Anderson, Dr. Lee Perry and Ms. Karla Waters of the University of New Mexico, Prof. R. C. Woods, Dr. Ion Abraham of the University of Wisconsin-Madison, and Prof. R. T. McGrath of Penn State University, plus all their coworkers, for early access to their experimental data. We also thank Dr. W. L. Morgan of the Kinema Research Company and Prof. V. McKoy of the California Institute of Technology for access to their data on electron-impact cross sections and reaction rates, and Ganesh Rajagopalan at SEMATECH for providing the etch rate data for Reactor III. We acknowledge the assistance of Gregory Troup in this work, and thank Drs. Gary Bell, Phil Ryan and John McBrayer for their support and program management efforts. We also thank Profs. D. Economou and D. B. Graves for helpful discussions.

This work was done at Sandia National Laboratories under CRADA No.1082 and WFO No. 17000106 with SEMATECH. It was primarily funded by SEMATECH and the Technology Partnerships Program, Office of Defense Programs, Department of Energy, with some funding from the Office of Basic Energy Sciences within the Office of Science.

Contents

Abstract 1
Acknowledgments 2
Contents 3
List of Figures 4
List of Tables 8
1. Introduction 9
2. General Development of Reaction Mechanisms 11
3. Reactor and Model Description 16
4. C_2F_6 Etch of Silicon Dioxide 19
4.1. Reaction Mechanism 19
4.2. Comparisons with Experiment 30
4.2.1. Etch Rates 30
4.2.2. Electron and Ion Densities 39
4.2.3. Neutral Species Densities 44
4.3. Dominant Reaction Paths 49
5. CHF_3 Etch of Silicon Dioxide 55
5.1. Reaction Mechanism 55
5.2. Comparisons with Experiment 60
5.2.1. Etch Rates 61
5.2.2. Electron and Ion Densities 63
5.2.3. Neutral Species Densities 67
6. C_4F_8 Etch of Silicon Dioxide 70
6.1. Reaction Mechanism 70
6.2. Comparisons with Experiment 74
6.2.1. Etch Rates 74
6.2.2. Electron and Ion Densities 80
6.2.3. Neutral Species Densities 81
7. C_2F_6 Plasma Etch of Photoresist 86
7.1. Reaction Mechanism 86
7.2. Comparisons with Experiment 93
8. CHF_3 Etch of Photoresist 105
9. C_4F_8 Etch of Low-k Dielectrics 107
10. Summary 109
References 111

List of Figures

Figure 1. Schematic diagram showing opposing forces in numerical simulations. 9
Figure 2. Schematic diagram of reaction mechanism development process. 11
Figure 3. Schematic diagram showing relationships between gas-phase reaction mechanisms of different chemical systems. 12
Figure 4. Schematic diagram showing relationships between surface reaction mechanisms of different chemical systems. 13
Figure 5. Schematics of the three plasma reactors used for comparisons between model predictions and experimental data. Drawings are not to scale and are not intended to give accurate geometry information. 17
Figure 6. Oxide etch rate comparisons between model and experiment for C_2F_6 in Reactor IB. Experimental conditions given in Table 6. Data generally in order of increasing power. 32
Figure 7. Blanket oxide etch rates as a function of plasma power in Reactor IB. 33
Figure 8. Blanket oxide etch rates as a function of pressure in Reactor IB. 34
Figure 9. Blanket oxide etch rates as a function of bias power in Reactor IB. 34
Figure 10. Oxide etch rates for a C_2F_6 plasma in Reactor III. 35
Figure 11. Oxide etch rates for C_2F_6 as a function of plasma power for three different pressures and four different flow rates in Reactor II. In (b), open and closed symbols represent older and newer sets of data. 36
Figure 12. Oxide etch rates for C_2F_6 as a function of pressure for three different powers (30 sccm) in Reactor II. Open and closed symbols represent older and newer sets of data. 37
Figure 13. Oxide etch rates for C_2F_6 as a function of flow rate for three different powers and pressures in Reactor II. 38
Figure 14. Oxide etch rates for C_2F_6 as a function of bias power for two different flow rates in Reactor II. 38
Figure 15. Electron density comparisons between model and experiment for C_2F_6 plasmas in Reactor IA. Dependence on: (a) plasma power, (b) pressure, and (c) bias power. 40
Figure 16. Negative ion density comparisons between model and experiment for C_2F_6 in Reactor IA. Dependence on: (a) plasma power, (b) pressure, and (c) bias power. 41
Figure 17. Ion current densities for C_2F_6 as a function of plasma power for three different pressures at four different flow rates in Reactor II. 42
Figure 18. Ion current densities for C_2F_6 as a function of pressure for three powers in Reactor II. 42
Figure 19. Ion current densities for C_2F_6 as a function of flow rate for three different powers and pressures in Reactor II. 43
Figure 20. CF_2 density comparisons between model and experiment (arbitrary units) for C_2F_6 in Reactor IA. Dependence on: (a) plasma power, (b) pressure, and (c) bias power. 45
Figure 21. CF density comparisons between model and experiment (arbitrary units) for C_2F_6 in Reactor IA. Dependence on: (a) plasma power, (b) pressure, and (c) bias power. 46
Figure 22. Gas temperatures from CF LIF experiments for C_2F_6 in Reactor IA. Dependence on: (a) plasma power, (b) pressure, and (c) bias power. 47

Figure 23. SiF density comparisons between model and experiment (arbitrary units) for C_2F_6 in Reactor IA. Dependence on: (a) plasma power, (b) pressure, (c) bias power, and (d) gas mixture with O_2. 48
Figure 24. SiF_2 density comparisons between model and experiment (arbitrary units) for C_2F_6 in Reactor IA. Dependence on: (a) plasma power, (b) pressure, and (c) bias power. 49
Figure 25. Primary gas-phase reaction paths of carbon-containing species for a C_2F_6 plasma in Reactor IA. Silicon wafer, oxide walls. 50
Figure 26. Primary gas-phase reaction paths of silicon-containing species for a C_2F_6 plasma in Reactor IA. Silicon wafer, oxide walls. 51
Figure 27. Primary reaction paths on the silicon wafer surface for a C_2F_6 plasma, Reactor IA... 52
Figure 28. Primary reaction paths on the oxide wall surface for a C_2F_6 plasma, Reactor IA..... 52
Figure 29. Primary gas-phase reaction paths of carbon-containing species for a C_2F_6 plasma in Reactor III. 53
Figure 30. Primary gas-phase reaction paths of silicon-containing species for a C_2F_6 plasma in Reactor III. 54
Figure 31. Primary reaction paths on the oxide wafer surface for a C_2F_6 plasma, Reactor III..... 54
Figure 32. Oxide etch rates for CHF_3 as a function of plasma power for three different pressures and two different flow rates in Reactor II. In (a), open and closed symbols represent older and newer sets of data. 61
Figure 33. Oxide etch rates for CHF_3 as a function of pressure for three different powers and two different flow rates in Reactor II. In (a), open and closed symbols represent older and newer sets of data. 61
Figure 34. Oxide etch rates for CHF_3 as a function of flow rate for three different powers and pressures in Reactor II. 62
Figure 35. Electron density comparisons between model and experiment for CHF_3 plasmas in Reactor IA. Dependence on: (a) plasma power, (b) pressure, and (c) bias power. 63
Figure 36. Negative ion density comparisons between model and experiment for CHF_3 in Reactor IA. Dependence on: (a) plasma power, (b) pressure, and (c) bias power. 64
Figure 37. Ion current densities for CHF_3 as a function of plasma power for three different pressures at four different flow rates in Reactor II. 65
Figure 38. Ion current densities for CHF_3 as a function of pressure for three different powers at two different flow rates in Reactor II. 66
Figure 39. Ion current densities for CHF_3 as a function of flow rate for three different powers and pressures. in Reactor II 66
Figure 40. CF_2 density comparisons between model and experiment (arbitrary units) for CHF_3 in Reactor IA. Dependence on: (a) plasma power, (b) pressure, and (c) bias power. 67
Figure 41. CF density comparisons between model and experiment (arbitrary units) for CHF_3 in Reactor IA. Dependence on: (a) plasma power, (b) pressure, and (c) bias power. 68
Figure 42. SiF density comparisons between model and experiment (arbitrary units) for CHF_3 in Reactor IA. Dependence on: (a) plasma power, (b) pressure, and (c) bias power. 69
Figure 43. Experimental oxide etch rates in two reactors show different C_2F_6 vs. C_4F_8 gas dependencies. (a) Reactor II, (b) Reactor IB, average of 6 repeats. 75
Figure 44. Oxide etch rate comparisons between model and experiment for C_4F_8 in Reactor II. The absence of a bar indicates no etching. 76
Figure 45. Oxide etch rate comparisons between model and experiment for C_4F_8 in Reactor IB. The absence of a bar indicates no etching. 77

Figure 46. Oxide etch rate dependence on bias power for C_4F_8 in: (a) Reactor II, (b) Reactor IB. Open points indicate no etching. 78
Figure 47. Oxide etch rate dependence on plasma power for C_4F_8 in Reactor II. Open point indicates no etching. 79
Figure 48. Oxide etch rate dependence for C_4F_8 in Reactor IB on (a) plasma power, and (b) pressure. Open point indicates no etching. 79
Figure 49. Electron density comparisons between model and experiment for C_4F_8 plasmas in Reactor IA. Dependence on: (a) plasma power, (b) pressure, and (c) bias power. 80
Figure 50. Negative ion density comparisons between model and experiment for C_4F_8 in Reactor IA. Dependence on: (a) plasma power, (b) pressure, and (c) bias power. 81
Figure 51. CF_2 density comparisons between model and experiment (arbitrary units) for C_4F_8 in Reactor IA. Dependence on: (a) plasma power, (b) pressure, and (c) bias power. 82
Figure 52. Simulated CF_2 densities show different bias dependencies with silicon and oxide wafers for C_4F_8 in Reactor IA. 82
Figure 53. SiF density comparisons between model and experiment (arbitrary units) for C_4F_8 in Reactor IA. Dependence on: (a) plasma power, (b) pressure, and (c) bias power. 83
Figure 54. SiF_2 density comparisons between model and experiment (arbitrary units) for C_4F_8 in Reactor IA. Dependence on: (a) plasma power, (b) pressure, and (c) bias power. 84
Figure 55. Simulated densities for (a) SiF and (b) SiF_2 show different bias dependencies with silicon and oxide wafers for C_4F_8 in Reactor IA. 85
Figure 56. Photoresist etch rates from two data sets for C_2F_6 show large between-run uncertainties in Reactor II. 93
Figure 57. Photoresist etch rates for C_2F_6 as a function of bias power for three different flow rates in Reactor II. Data Sets 2 and 3, between-run uncertainty ×3-4. 94
Figure 58. Photoresist etch rates for C_2F_6 as a function of bias power for three different powers in Reactor II. (a) 6.5 mTorr, (b) 20 mTorr. Data Set 1, between-run uncertainty ×3-4. Model expected to be high. 94
Figure 59. Photoresist etch rates for C_2F_6 as a function of (a) power and (b) pressure in Reactor II. Data Set 3, between-run uncertainty ×3-4. 95
Figure 60. Selectivities for oxide etching over photoresist etching for C_2F_6 as a function of (a) power and (b) pressure in Reactor II. Data Set 3. 95
Figure 61. Selectivities for oxide etching over photoresist etching for C_2F_6 as a function of bias voltage in Reactor II. Data Sets 2 and 3. 96
Figure 62. Blanket photoresist etch rate comparisons between model and experiment for C_2F_6 in Reactor IB. Experimental conditions given in Table 6. Data generally in order of increasing power. 97
Figure 63. Blanket photoresist etch rates for C_2F_6 as a function of (a) plasma power, (b) pressure, and (c) bias power, in Reactor IB. 97
Figure 64. Patterned photoresist and oxide etch rate comparisons between model and experiment for C_2F_6 in Reactor IB. Experimental conditions given in Table 20. Data generally in order of increasing power. 98
Figure 65. Patterned photoresist etch rates for C_2F_6 as a function of (a) plasma power, and (b) pressure, in Reactor IB. 99
Figure 66. Experimental photoresist etch rates for C_2F_6 show different (a) power and (b) pressure dependencies at different conditions in Reactor IB. 100

Figure 67. Experimental oxide etch rates for C_2F_6 show different (a) power and (b) pressure dependencies at different conditions in Reactor IB. 100
Figure 68. Simulated photoresist etch rates for C_2F_6 show less difference in (a) power and (b) pressure dependencies for different conditions in Reactor IB. 101
Figure 69. Simulated oxide etch rates for C_2F_6 show less difference in (a) power and (b) pressure dependencies for different conditions in Reactor IB..... 101
Figure 70. Selectivity comparisons between model and experiment for blanket wafers in C_2F_6, Reactor IB. Experimental conditions given in Table 6. Data generally in order of increasing power. 102
Figure 71. Selectivities for blanket wafers in C_2F_6, Reactor IB. Dependence on (a) plasma power, (b) pressure, and (c) bias power. 103
Figure 72. Selectivity comparisons between model and experiment for patterned wafers in C_2F_6, Reactor IB. Experimental conditions given in Table 20. Data generally in order of increasing power. 104
Figure 73. Selectivities for patterned wafers in C_2F_6, Reactor IB. Dependence on (a) plasma power and (b) pressure. 104
Figure 74. Photoresist etch rates for CHF_3 as a function of power for different pressures and flow rates in Reactor II. Data Set 2, between-run uncertainty ×3-4. 105
Figure 75. Selectivities for CHF_3 as a function of power for different pressures and flow rates in Reactor II. Open and closed symbols represent older and newer set of data. 106
Figure 76. Low-k dielectric etch rate dependence for C_4F_8 in Reactor IB. (a) 40% porosity (b) 50% porosity. 107
Figure 77. Etch rate dependence for C_4F_8 in Reactor II on O_2 gas fraction. (a) 67% porosity low-k dielectric, (b) 41% porosity low-k dielectric, (c) silicon dioxide. 108

List of Tables

Table 1. Operating conditions for plasma etch reactors and input parameters for the Aurora model. 18
Table 2. Gas-phase reaction mechanism for C_2F_6 plasma etching of silicon dioxide. 22
Table 3. Surface reaction mechanism for C_2F_6 plasma etching of silicon. 27
Table 4. Surface reaction mechanism for C_2F_6 plasma etching of silicon dioxide. 28
Table 5. Summary of Aurora comparisons to experimental data for C_2F_6 plasmas. 31
Table 6. Conditions for C_2F_6 plasma etching of oxide shown in Figure 6 for Reactor IB. 32
Table 7. Conditions for C_2F_6 plasma etching of oxide shown in Figure 10 for Reactor III. 35
Table 8. Distribution of gas-phase and surface species for a C_2F_6 plasma in Reactor IA. Silicon wafer, oxide walls. 44
Table 9. Additional gas-phase reactions for CHF_3 plasma etching of silicon dioxide. 56
Table 10. Additional surface reactions for CHF_3 plasma etching of silicon. 57
Table 11. Additional surface reactions for CHF_3 plasma etching of silicon dioxide. 58
Table 12. Summary of Aurora comparisons to experimental data for CHF_3 plasmas. 60
Table 13. Additional gas-phase reactions for C_4F_8 plasma etching of silicon dioxide. 71
Table 14. Additional surface reactions for C_4F_8 plasma etching of silicon. 71
Table 15. Additional surface reactions for C_4F_8 plasma etching of silicon dioxide. 72
Table 16. Summary of Aurora Comparisons to Experimental Data for C_4F_8 Plasmas. 75
Table 17. Conditions for C_4F_8 plasma etching of oxide shown in Figure 44 for Reactor II. 76
Table 18. Conditions for C_4F_8 plasma etching of oxide shown in Figure 45 for Reactor IB. 77
Table 19. Surface reactions for fluorocarbon plasma etching of photoresist. 87
Table 20. Conditions for C_2F_6 plasma etching of patterned photoresist and oxide shown in Figure 62 for Reactor IB. 98

Chemical Reaction Mechanisms for Modeling the Fluorocarbon Plasma Etch of Silicon Oxide and Related Materials

1. Introduction

The plasma etch of dielectric oxide layers is an important step in the fabrication of modern microelectronics devices. The gases used in these processes are becoming increasingly controlled because of environmental concerns, which makes it important to ensure that these processes are efficient and well optimized. Computational modeling of materials-processing technologies is proving to be useful in accelerating equipment and process development. However, an accurate simulation of such processes requires an understanding of the chemistry occurring in the system, which can be quite complex.

As part of a project with SEMATECH, we have been studying chemistry of the fluorocarbon (C_2F_6, CHF_3 and C_4F_8) plasmas used to etch silicon dioxide and related materials. This work is now ending; this report presents the final reaction mechanisms and documents the results. Most of the work on C_2F_6 and CHF_3 is described elsewhere [1]. The present report reproduces much of that description, but adds a number of figures that were left out of the journal publication in the interest of space, as well as comparisons to data that were delivered after completion of that manuscript. This report also describes work on C_4F_8 plasmas, as well as preliminary work on etching of photoresist and low-k dielectrics that are not described elsewhere.

Developing numerical models for these complex reacting flow systems requires constant trade-offs between opposing forces, some of which are shown schematically in Figure 1. On one axis, the desire to treat the reactor geometry in detail (two or three dimensions) is counterbalanced by the desire to get answers in a reasonable amount of time (hours of computational time rather than weeks). In the other dimension, the desire to treat the chemistry in a complete and rigorous manner is counterbalanced by the absence of fundamental kinetic data for all the molecules and reactions of interest (as well as computational resources).

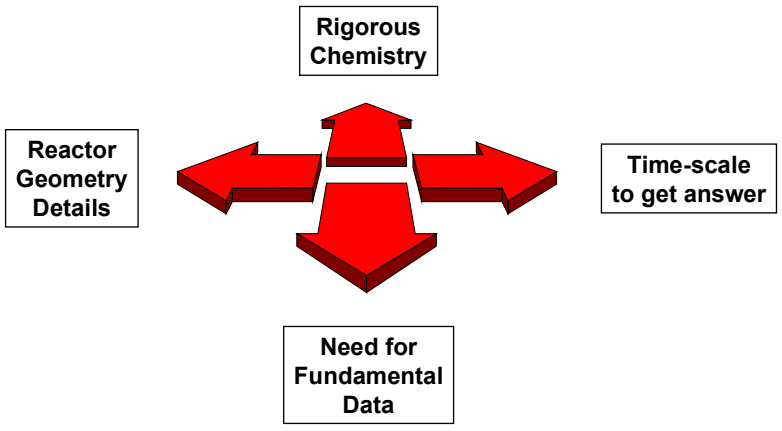

Figure 1. Schematic diagram showing opposing forces in numerical simulations.

This work is focused on the chemistry occurring in these plasma systems, so we use a 0-D (zero-dimensional) description of the mass transport in the system. This allows the consideration of large numbers of chemical reactions while keeping computational requirements reasonable. We focus on etch rates and diagnostic measurements of gas-phase species densities for three specific, well-characterized plasma systems, that were provided by other researchers as part of the larger, overall project.

Our work has resulted in a detailed chemical reaction mechanism for fluorocarbon plasma etching of silicon oxide that includes all the important gas-phase and surface processes, and validate it by comparison with experimental data. Rate parameters are generally taken from independent studies in the literature, or estimated from rates measured for related species. A wide range of experimental data were used to develop and test the chemical reaction mechanisms for these fluorocarbon plasmas, especially for C_2F_6. These include measurements of etch rates, electron densities, negative ion densities, relative densities of CF, CF_2, SiF and SiF_2, gas temperatures, and ion current densities in these three reactors. The challenge lies not in matching model predictions to any one set of experimental data, but rather in attaining the best overall match for all the measurements in the three different reactor systems over the entire range of experimental conditions. This leads to compromises, where rate parameters that gave satisfactory agreement with two sets of measurements were chosen over rate parameters that gave good agreement with one set of data and poor agreement with a different set.

Many of the commercial plasma etching reactors currently in use are high-density plasma (HDP) reactors, and thus this work is targeted at such systems. HDP reactors combine high power densities with lower pressures (generally a few mTorr) than other plasma processes. These conditions have several implications for the chemistry to be included in the model: a) A high power density leads to large reactant dissociation fractions, and thus the need to include dissociation reactions for these fragments as well as the initial reactant; b) A low pressure decreases the importance of gas-gas reactions relative to gas-surface reactions for loss of ions and radicals; c) A low pressure decreases the importance of collisionally-activated unimolecular decomposition reactions, as well as their inverse collisionally-stabilized bimolecular recombination reactions, which should be well into their pressure dependent regimes. Finally, low pressures can also reduce the importance of mass transport limitations relative to chemical kinetics. The surface part of the reaction mechanism uses multiple surface species and multiple materials, and includes neutral adsorption, spontaneous etching, ion-assisted etching, ion neutralization and radical abstraction reactions.

In general, we try to base our choice of reactions and rate parameters on independent fundamental studies as much as possible. But this is a very complex chemical system, so despite a philosophical inclination to include all possible chemical species and reactions, there are still simplifications in the chemistry. For example, we do not include the full range of plausible chemical species on the surfaces. Also, we do not include an elaborate growth mechanism for polymer growth, which would be more important under extremely low bias conditions where polymer deposition completely overwhelms oxide etching and a production reactor would rarely be operated.

2. General Development of Reaction Mechanisms

The actual mechanisms are given in the relevant sections, along with a description of the reactions for specific molecules. Here we describe general features of the mechanism development process. Our general approach has been described elsewhere [2, 3] and is shown schematically in Figure 2. This is an iterative process that starts by assembling cross section and kinetic data for gas-phase reactions for the molecules of interest. In the early stages, it is preferable to err on the side of too many rather than too few reactions, so we try to consider all reactions that might be important in the system. But the literature rarely contains all the desired information, so often estimates based on related molecules must be used. The gas-phase data are combined with a set of postulated surface reaction paths and rates. Surface reactions generally have far less information in the literature than gas-phase reactions, which means that most postulated surface species and reactions will have estimated rate parameters. This, in turn, encourages the use of "lumped" and "effective" reactions, which helps to minimize the number of species and reactions, which in turn helps deal with computational resource limitations.

This initial reaction mechanism is compared, using a low-order (low-dimensionality) plasma model, against an experimental data set. The results of the initial comparisons are invariably highly unsatisfactory, but generally provide some direction as to what reaction paths need to be added and/or have the rate parameters adjusted. The mechanism is then tested against experiment again. These iterations continue until satisfactory agreement is attained, or when new experimental data is acquired. As presented in this report, the reaction mechanisms contain many reactions that may not be important under any given set of conditions, but are retained to make the mechanism as broadly applicable and complete as possible. For higher-dimensionality simulations, i.e. 2D simulations of a particular tool, it is best to then reduce the reaction mechanism to a subset of reactions that are most important for the parameter space of interest.

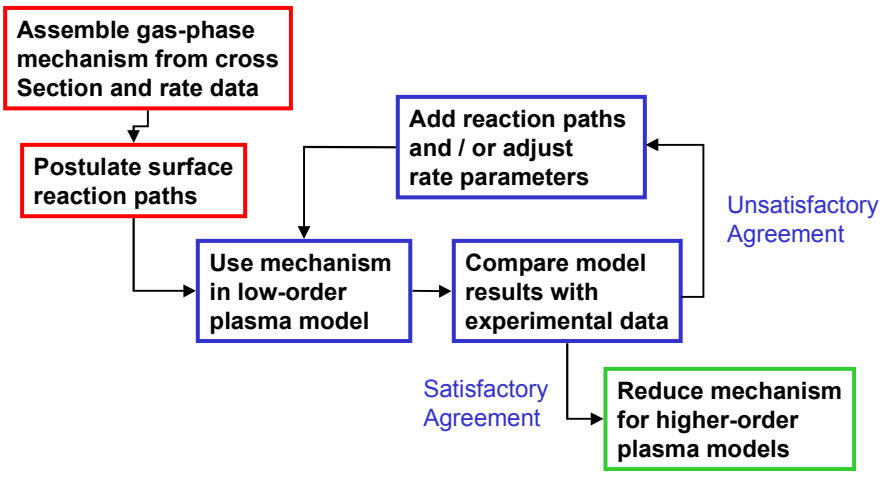

Figure 2. Schematic diagram of reaction mechanism development process.

The reaction mechanisms themselves are modular, with newer parts building on previous work. Figure 3 schematically shows the relationships between the gas-phase reaction mechanisms for the different plasmas of interest in this report, while Figure 4 shows the analogous parts of the surface reaction mechanisms. The chemical reaction mechanism for C_2F_6 plasmas was developed and validated first. The CHF_3 mechanism consists predominantly of the C_2F_6 mechanism with added reactions for CHF_3 and other hydrogen containing species. Likewise, the C_4F_8 mechanism consists predominantly of the C_2F_6 mechanism with added reactions for C_4F_8 and a few of its fragment species. Modeling the etching of a different solid phase involves the development of a surface reaction mechanism for that material, as well as the addition of any new etch product species to the gas-phase mechanism. This approach results in a self-consistent set of reaction mechanisms for these related plasma etching systems, although the agreement with experiment for any individual system may be improved by accepting worse fits elsewhere. During the course of the project, several interim versions of these mechanisms were distributed. These are not included in this report, as we believe that these earlier versions should be discarded and only the final versions used for simulations.

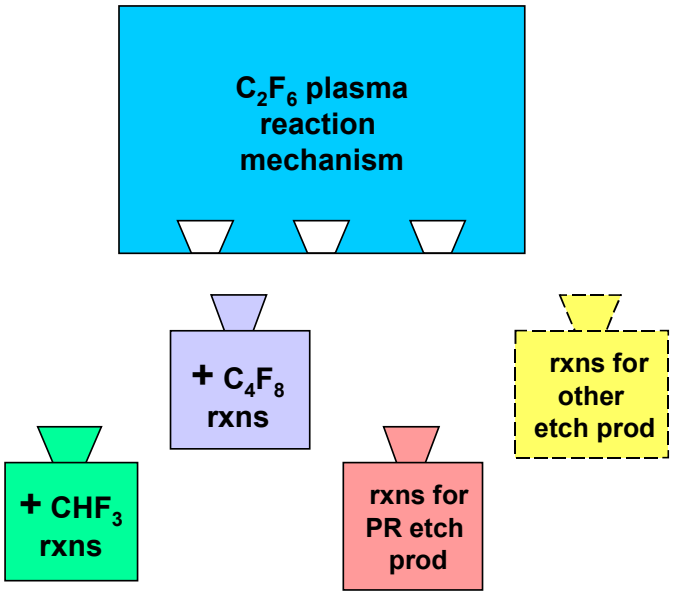

Figure 3. Schematic diagram showing relationships between gas-phase reaction mechanisms of different chemical systems.

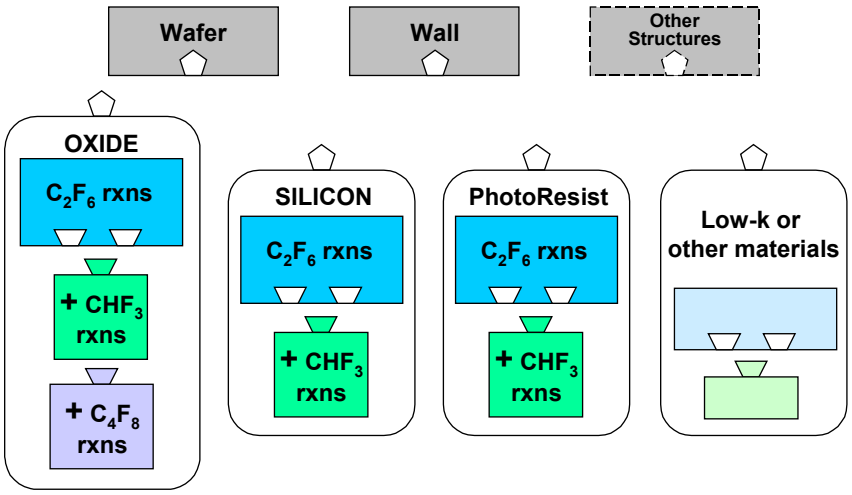

Figure 4. Schematic diagram showing relationships between surface reaction mechanisms of different chemical systems.

Our models employ the CHEMKIN software [4], for describing the kinetics of the homogeneous and heterogeneous reactions. The chemical reaction mechanism is therefore given in terms of rate coefficients of the form: $k = A\ T^B \exp(-C/T)$, where T can be one of several different temperatures (gas, electron, ion, or surface). In the gas-phase mechanism, the units for A depend on the order of the reaction, but are in molecules, cm and s, B is for temperature in Kelvin, and the units for C are Kelvin. For electron-impact reactions, there is an additional parameter ε, the electron collision energy loss in eV. For surface reactions, sticking and Bohm coefficients are of the form: $k_f = A \exp(-C/T)$. The units of A again vary, but either give a unitless sticking coefficient / Bohm parameter, or give a reaction rate in molecules $cm^{-2}\ s^{-1}$. C is in units of Kelvin, and applies to the temperature of the surface. It is generally set to zero to minimize the number of adjustable parameters unless independent data are available for the surface temperature dependence. A # in the reaction description indicates a species with an ion energy dependent yield given by: $h\ (E_{ion}^{0.5} - E_{th}^{0.5})$, where E_{th}, unless otherwise indicated, is 4 eV. A number of the surface reactions are written involving fractional or multiple surface species, in order to produce a chemically balanced reaction, in situations where the kinetics of the reaction should be first order in that species. In these situations, we used the FORD (forward reaction order) option within the Surface-CHEMKIN software to override the default based on the reaction stoichiometry and set it to the desired first order dependence.

For the gas-phase part of the mechanisms, electron impact reactions are the most prevalent. The use of rate coefficients and temperatures for electron-impact reactions implicitly assumes that the electron energy distribution function (EEDF) is known *a priori*. We assume that the EEDF is Maxwellian to derive the rate coefficients from reaction cross sections. Although the EEDF may have non-Maxwellian characteristics that vary with plasma conditions, we believe that the

uncertainties in the chemical rate parameters (cross sections) are likely to dwarf the errors caused by this assumption. A number of ion-molecule and ion-ion reactions are also included. However, reactions among neutral species are generally not part of the mechanism, although many such reactions were collected and included in early versions. The very low pressures used in these plasma reactors means that the relative importance of gas-wall vs. gas-gas collisions becomes higher than usual in reacting gas systems. Reactions requiring collisional activation of a reactant or collisional stabilization of a product also become unimportant.

The electron impact reactions in the mechanisms generally include vibrational and electronic excitations, dissociative ionizations, dissociations to neutral fragments, and dissociative attachment reactions. These reaction paths are included for electron impact with reactants, major dissociation fragments, and etch products. The rates of reactions involving electrons are dependent on the electron temperature, rather than the neutral gas temperature. For the electron-impact reactions, rate parameters were obtained by integrating electron-impact cross-section data from the literature with a Maxwellian EEDF. In a few cases, the rate constants that resulted from this integration have been altered somewhat from the literature-generated values, within the uncertainty of the cross-section data, in order to improve the agreement between model predictions and the experimental data. Rates that have been modified in this way are generally indicated in the Notes column of the Tables, and by comments in the input file, which also provide some information on the sources of the rate parameters.

Solving energy balances requires thermochemical data for the chemical species in the mechanism. For the CHEMKIN software, these data are input in the form of polynomial fits to temperature. These data are used to calculate reverse reaction rates, as well as for determining heats of reaction for the energy balance. The prevalence of irreversible reactions in this reaction mechanism means that the accuracy of these data are less critical than for other thermal reacting flows, but they are still important for determining heats of reaction for the energy balance. Thermochemical data for the gas-phase species were primarily obtained from standard sources such as the CHEMKIN [4], JANAF [5], or NASA [6] Thermodynamic Databases. For a few of the ionic species, however, such data were not available so the data for the corresponding neutral species were used after adjusting the heat of formation by the appropriate ionization energy or electron affinity.

Developing a surface reaction mechanism is less straightforward than developing a gas-phase reaction mechanism. Although the Surface CHEMKIN formalism is flexible enough to include any number of surface species on a variety of sites, phases, and materials, there is generally far less independent chemical-kinetic data in the literature to use in constructing the mechanism. As a result, rate parameters for surface reactions are often derived by fitting to experimental etch or deposition rate data. Despite this "fitting" procedure, using a set of fundamental reaction-path descriptions provides much more accurate and predictive models than would purely phenomenological models. Physically based models are applicable to a wider range of conditions and can predict effects not directly measured in the calibration process.

Many of the diagnostic experiments, which were used for mechanism development and model validation, were done with a silicon wafer rather than an oxide wafer in the reactor. Therefore, each surface mechanism includes a set of reactions for silicon substrates in addition to the

reactions for silicon dioxide. The latter describes both the chemistry of the desired etching of oxide layers as well as the unintentional erosion of quartz or glass walls. We note, however, that the reaction mechanism has not been validated to quantitatively describe the fluorocarbon etching of silicon surfaces, but rather to roughly represent the consumption of ions and F atoms at the surface, plus the production of volatile etch products. The use of a silicon wafer rather than an oxide wafer in the simulations has minor effects (<10%) on the electron and negative ion densities, but sometimes lead to more significant changes (up to ×3) in the predicted CF_2, SiF and SiF_2 densities. The LIF measurements for these radicals give relative density only, so trends are more important than the actual values. The trends in these species densities are generally the same with the two materials, except for the dependence on bias power. As discussed below, these molecules are consumed or produced by the etching of the oxide surface, so their densities would be expected to be more sensitive to the reactions occurring on the wafer surface.

3. Reactor and Model Description

The simulations presented here use a well-mixed plasma reactor model, AURORA, which has been described in detail elsewhere [7,8]. Our use of a 0-D model is a direct result of our focus on the chemistry occurring in these plasmas. By using a very simple description of the transport, the repeated simulations over a large region of parameter space that are needed to develop these large mechanisms can be done in a reasonable amount of time. These mechanisms can then be reduced for use in higher-dimensionality simulations to address issues of etch uniformity for a more limited set of conditions. However, the models used in this work are modular in nature, so the reaction mechanisms, although developed with AURORA, should be usable with other simulation tools.

This model assumes that the plasma is essentially rate-limited by chemical kinetic processes and not by transport effects, which is reasonable for simulating low-pressure (~10 mTorr) plasma reactors. The model solves equations for the energy balances of electrons and neutrals, as well as species and mass balances over a specified reactor volume. The model also solves the surface site balances at surfaces for one or more materials comprising the reactor boundaries, which can have different sets of chemical reactions occurring on them. The species balance for each gas-phase species includes the net production and loss rates on surfaces weighted by the specified surface area of each material with which the species interacts. The gas energy balance requires a heat transfer coefficient to describe the heat losses from the reactor volume to the external environment.

Experimental data from 3 different high density plasma reactors, schematically shown in Figure 5, were used to develop and test these chemical reaction mechanisms. Reactor I is a laboratory-scale "GEC" (Gaseous Electronics Conference) reference reactor that has been described in detail elsewhere [9,10]. For the experimental data used in this study, this reactor has been modified from the original configuration by using inductive coupling of the plasma power, and the addition of a quartz ring above the wafer/chuck to help confine the plasma [11]. Two versions of Reactor I with slightly different geometries were used for the experiments being modeled here and discussed in the next section. Version A was used for the diagnostic measurements done by Hebner and coworkers [11,12,13,14]. Version B was used for sets of etch rate data acquired by Anderson and coworkers [15,16]. Reactor II is a different laboratory-scale reactor that has been described elsewhere by Oehrlein and coworkers [17,18]. For this reactor, etch rate data and ion current density measurements were available. Reactor III is a Lam commercial high-density plasma etch reactor, and was used to acquire C_2F_6 etch rate data only.

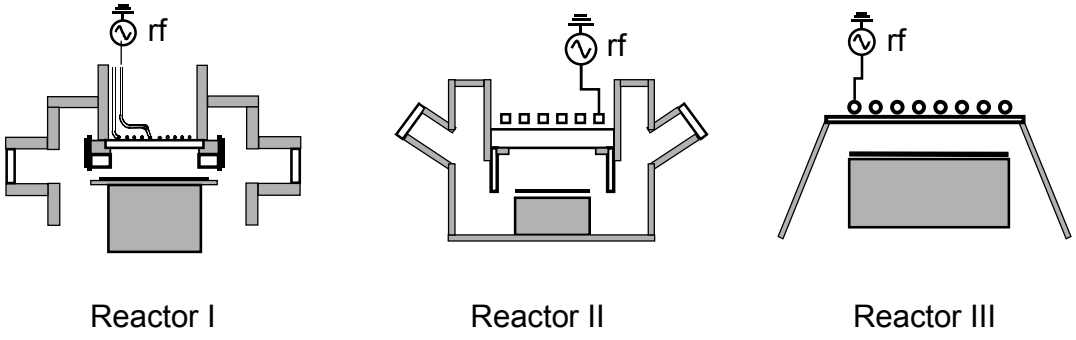

Figure 5. Schematics of the three plasma reactors used for comparisons between model predictions and experimental data. Drawings are not to scale and are not intended to give accurate geometry information.

The operating conditions of interest for each of the reactors, along with the various parameters used to describe these reactors/experiments with the AURORA model, are given in Table 1. In Reactor I, the plasma expands past the electrodes at lower pressures, so we use pressure dependent volumes, total surface areas and wafer surface areas in modeling this system. As in our previous work on $BCl_3/Cl_2/Ar$ plasmas [19], a limited number of two-dimensional simulations were used to estimate these dependencies. Values for wafer temperatures were generally provided by the experimentalists; the differences between reactors mostly reflect differences in wafer cooling. Wall temperatures were estimated to increase with power, based on CF rotational temperatures determined in laser-induced fluorescence measurements by Hebner [12] in Reactor I that yielded temperatures of 400-700K. Ion temperatures were estimated to be 5000K. Once a set of parameters for describing a given reactor in the model was determined, it was used for simulating all of the chemical systems included in this report.

Corrections to plasma powers, in the form of coupling efficiencies, have been shown to be necessary in experimental measurements of currents and voltages in C_2F_6 and CHF_3 plasmas [11]. Measurements in Reactor I over a range of powers and pressures showed that only 80% of the power from the main rf supply actually reaches the plasma, but that the bias power needed no such correction. Coupling efficiencies for Reactor II were estimated from similar considerations [20]. No power correction was used for Reactor III.

Table 1. Operating conditions for plasma etch reactors and input parameters for the Aurora model.

Parameter	Reactor IA	Reactor IB	Reactor II	Reactor III
Volume (cm^3)	374.4-629.4 [422.4][a]	423.6-759.7	2778.2	4020
Total Surface Area (cm^2)	288.5-713.5 [368.5][a]	288.5-683.9	949.5	1630
Etch Area Fraction	0.256-0.341 [0.376][a]	0.119-0.281	0.129	0.198
Plasma Power (W)	100-400 [200][a]	205-495	600-1400	1550-1650
Coupling Efficiency	0.8	0.8	0.6-0.7	1.0
Bias Power (W)	0-140 [20][a]	22-148	--	1000-1800
Ion Energy (eV)	--	--	100	--
Pressure (mTorr)	5-40 [10][a]	5.2-24.8	6.5-20	10-30
Gas Flow Rate (sccm)	10	10	10-40	20-40
Wafer Temperature (K)	373	293	300	353
Wall Temperature (K)	373-493 [413][a]	413-533	428-593	373
Heat Transfer Coefficient to Ambient (cal/K-s)	4.66E–4	4.66E–4	4.66E–4	4.66E–4
ξ for Bohm Fluxes	0.4	0.4	0.6	0.7
Energy Transfer to Ions in Sheath (kT_e)	4	4	7	7

[a] [ ] indicates the value at the base conditions used for this reactor.

4. C_2F_6 Etch of Silicon Dioxide

The reaction mechanism for the hexafluoroethane plasma etch of silicon dioxide was the most completely studied and validated system of those examined in this project. It forms the basis of the reaction mechanisms for the other plasma gases, and had the most experimental data available for model validation.

4.1. Reaction Mechanism

The reaction mechanism for this system is given at the end of this subsection. It consists of three Tables, one for each of the CHEMKIN and Surface-CHEMKIN input files. Table 2 gives the gas-phase chemistry, and involves 28 species and 132 reactions. Table 3 gives the surface reactions for silicon surfaces, and Table 4 for oxide surfaces. The surface part of the mechanism involves 2 materials, 6 species, and 85 reactions.

Electron impact reactions for C_2F_6 have recently been reviewed by Christophorou and Olthoff [21], and the reaction rates in the mechanism are derived from cross section data by Hayashi [22] and by Poll and Meichsner [23]. Using these reaction rates in our simulations shows that, under the reactor conditions of interest, most of the C_2F_6 dissociates in the plasma, so that electron impact reactions for a number of smaller CF_x species need to be included in the mechanism. Rates for CF_4 reactions were obtained from the cross section data suggested by Christophorou, et al. [24], who also provided some information for CF_3 and CF_2. Other data for CF_x (x=0-3) species were computed by McKoy [25], obtained from Morgan [26], Tarnovsky [27], or, for cases where no data were available, by copying the analogous CF_4 reaction and adjusting the electron energy loss appropriately [2]. Rate data for C atoms are based on cross sections from Henry, et al. [28]. Those for F atom excitations are based on calculations of Baliyan and Bahtia [29], and ionization data from Hayes, et al. [30]

For some reactor conditions, especially those with high oxide etch rates, the etch products constitute a substantial fraction of the plasma species, so electron impact reactions of SiF_x (x=1–4), CO and O_2 are included in the mechanism. Data for SiF_4 were obtained either from Morgan [26] based on unpublished swarm data [31], or by copying CF_4. Ionization data for SiF_x (x=1–3) were obtained from Hayes and coworkers [32,33,34], while dissociation and dissociative attachment reactions were adapted from SiF_4 or CF_4. The rate parameters for O_2 are based on the work of Itikawa [35], Phelps [36], and Cosby [37], while data for O atoms are from Itikawa [38]. Data for CO are primarily from the cross section set published by Land [39], with dissociation data from Cosby [40] and ionization data from Rapp and Englander-Golden [41].

The remaining reactions in Table 2 represent a variety of reaction types. Reactions 102-109 are dissociative recombination reactions between electrons and all the positive ions with estimated rate parameters. Reactions 110-119 are associative detachment reactions of negative ions (F^-) with a variety of radicals. In this case, rate parameters are estimates that have been scaled by the size of the neutral radical. Reactions 120 and 121 are charge exchange reactions with rate parameters from Anicich [42]. Reactions 122-132 are ion-ion neutralization reactions with estimated rate constants from information in Smirnov [43]. In many of these cases, the

uncertainties in the rate parameters were large and the estimated rate parameters were adjusted within these uncertainties to improve agreement between model predictions and experiment.

As for the gas-phase mechanism, the surface reaction mechanisms contain a number of different types of reactions, and parallel reactions often occur on the silicon and silicon dioxide surfaces. The first reaction in both cases is the direct etching of Si and SiO_2 by F atoms. Although this turns out to be only a minor contribution to the etch rate under the conditions of interest, they are included for completeness, with rate parameters taken from the experimental measurements by Flamm, et al. [44,45]. The reaction is reported as a sticking coefficient that is first order in the gas-phase species, but requires the use of non-integer stoichiometric coefficients for the other species in the reaction in order to balance the reaction. When non-integer coefficients are used in the mechanism, the FORD (forward reaction order adjustment) feature of the Surface CHEMKIN software [4] is required to make the global reaction kinetics first order in the species of interest rather than the default fractional order that would result from the law of mass action.

The second type of reaction on both surfaces is the adsorption of F atoms on open silicon Si(S) and oxide SiO_2(S) sites. F reactions with silicon surfaces have been extensively studied and are known to create the full array of SiF_x (x=1-4) surface species. However, in the interest of minimizing the number of species and reactions in the mechanism, we have chosen to use only one "lumped" species, Si_F_2(S), which represents a surface silicon atom with two F atoms bonded to it. On the oxide surface, we use a corresponding species SiO_2_F_2(S), which does not specify in any detail how the F is bonded to the surface. The sticking coefficient values for F atom adsorption on silicon surfaces is ten times higher than for oxide surfaces, and both values are taken from the beam/surface experimental work by Gray, et al.[46].

In fluorocarbon plasmas, the deposition of polymeric materials on surfaces is known to play an important role in enabling selective and anisotropic etching. We simulate the effects of polymer deposition on the oxide surfaces by including the adsorption of CF_x (x=1-3) species on the surface in our mechanism. This captures the effects of surface site occupation by fluorocarbon radicals produced by the plasma, although we do not track the actual deposition or sputter rates of the polymer. Although the SiO_2_CF_2(S) species participates in ion-assisted etching reactions, its presence on the surface also blocks the direct F atom etching reactions. In the interest of mechanism simplification, we only include SiO_2_CF_2(S) rather than including the full array of SiO_2_CF_x(S) species. The value for the CF_2 sticking coefficient in the mechanism is taken from the work of Butterbaugh, et al. [47]. Based on the degree of coordinative unsaturation, the sticking coefficients for CF and CF_3 are set to be higher and lower, respectively, than that for CF_2. The values were chosen to be in accord with this criteria while providing optimal fits to the experimental data.

The primary etching reactions are the ion-assisted etching processes given by reactions 3-13 in Table 3 and reactions 6-27 in Table 4. In these reactions, an incident ion neutralizes at a covered site [Si_F_2(S), SiO_2_F_2(S), or SiO_2_CF_2(S)], while causing a certain number of concomitant reactions between the bulk and surface species that lead to the desorption of SiF_4 plus O_2 or CO etch products. The number of etching/desorption reactions caused by a single ion is given by the ion-energy dependent yield: $Y = h\,(E_{ion}^{0.5} - E_{th}^{0.5})$, where E_{th} is set to 4 eV for all ion-yield reactions. The values of the yield parameters are generally higher for silicon surfaces than for

oxide surfaces, and are derived from the work of Gray and coworkers [46,47] on the etching of silicon and silicon oxide with beams of F/F_2 and/or CF_2. These workers reported yields using argon ions at a range of ion energies, and their results in the 150-250 ion energy range were used as starting points for our mechanism. The reported yields for Ar^+ were scaled by the mass of the incident ion to obtain initial values for the h parameters in the Tables. These could then be adjusted in groups to get better agreement with experimental etch rates. For example, for etching via the $SiO_2\_CF_2(S)$ species, the yields have been increased by a factor of 1.5 from their initial values.

The mechanism includes the neutralization of positive ions on open surface sites, which is the default reaction event for ions and surface sites. If no other reaction is identified for a given ion and site, then we assume that the neutralization process will occur. If another reaction is included with a reaction probability less than 1, neutralization is put it with a reaction probability that makes up the difference. These surface reactions are given high reaction probabilities and, under some conditions, represent a significant pathway for loss of ions and electrons in the plasma. In contrast, the contributions of ion deposition on open sites were generally small. However, in cases where the surface was mostly open, they could contribute a noticeable amount of F to the surface. Such cases were used to determine the rate parameters by fitting to the experimental data.

The remaining surface reactions are radical abstraction or recombination reactions. The abstraction of F atoms by neutral radicals is a reasonable path for "cleaning" fluorinated surface sites in addition to ion-assisted desorption. Si-F bonds are generally stronger than C-F bonds, so abstractions by SiF_x radicals, but not CF_x radicals, are included. Abstraction by C atoms is included to counter an unphysical buildup of C and in recognition of the fact that an atomic species should be quite reactive. However, the bond in F_2 is fairly weak, so F abstraction by F atoms is not included. Including the abstraction reactions with estimated sticking coefficients on the order of a few percent (with higher values for species with more unsaturation), improved the agreement between model and experiment. F atom abstraction from $SiO_2\_CF_2(S)$ species presented some mechanistic difficulties in producing balanced reactions that were physically meaningful, but we decided to have these reactions produce a gas-phase CF and an open site rather than introduce a $SiO_2\_CF(S)$ species. The rate parameter for O atom recombination on a surface is taken from Greaves and Linnett [48].

Table 2. Gas-phase reaction mechanism for C_2F_6 plasma etching of silicon dioxide. [a]

No.	Reaction	A	B	C	ε	Notes	Ref.
	electron impact reactions						
1.	$e^- + C_2F_6 \rightarrow C_2F_6 + e^-$	2.128E–7	–0.3252	3.676E3	0.14	V5 [b]	22
2.	$e^- + C_2F_6 \rightarrow C_2F_6 + e^-$	6.788E–8	–0.4328	6.072E3	0.09	V6 [b]	22
3.	$e^- + C_2F_6 \rightarrow C_2F_6 + e^-$	3.797E–4	–0.7779	2.192E4	0.15	V7 [b]	22
4.	$e^- + C_2F_6 \rightarrow C_2F_6 + e^-$	3.830E–3	–1.142	1.154E5	7.2	E [c]	22
5.	$e^- + C_2F_6 \rightarrow C_2F_6 + e^-$	1.898E–12	0.6096	1.316E5	11.1	E [c]	22
6.	$e^- + C_2F_6 \rightarrow 2CF_3 + e^-$	3.124E–8	0.1003	1.591E5	12.3	[d]	22
7.	$e^- + C_2F_6 \rightarrow CF_3^+ + CF_3 + 2e^-$	2.483E–12	0.8790	1.637E5	15.5	[e]	23
8.	$e^- + C_2F_6 \rightarrow CF_2^+ + CF_4 + 2e^-$	3.291E–13	0.8655	2.408E5	17.3	[e]	23
9.	$e^- + C_2F_6 \rightarrow CF^+ + CF_4 + F + 2e^-$	7.899E–14	1.009	1.977E5	18.0	[e]	23
10.	$e^- + C_2F_6 \rightarrow F^- + CF_2 + CF_3$ LT [g]	2.514E–7 9.106E4	–0.6587	–6847.0 –7.61E9	2.5	[d, f]	22
11.	$e^- + CF_4 \rightarrow CF_4 + e^-$	6.423E–7	–0.3186	3.999E3	0.11	V3 [b]	24
12.	$e^- + CF_4 \rightarrow CF_4 + e^-$	9.884E–9	–0.2602	1.168E3	0.05	V4 [b]	24
13.	$e^- + CF_4 \rightarrow CF_4 + e^-$	0.2	–1.367	7.734E4	4.0	V [h]	24
14.	$e^- + CF_4 \rightarrow CF_3 + F + e^-$	1.190E–16	1.309	1.446E5	5.6	[i]	24, Table 21
15.	$e^- + CF_4 \rightarrow CF_2 + 2F + e^-$	7.775E–17	1.184	1.663E5	9.5	[i, j]	24, Table 21
16.	$e^- + CF_4 \rightarrow CF + 3F + e^-$	1.039E–16	1.187	2.203E5	14.9	[i, j]	24, Table 21
17.	$e^- + CF_4 \rightarrow CF_3^+ + F + 2e^-$	1.159E–11	0.7645	1.993E5	15.9		24, Table 15
18.	$e^- + CF_4 \rightarrow CF_2^+ + 2F + 2e^-$	2.886E–11	0.5108	2.649E5	22.0	[j]	24, Table 15
19.	$e^- + CF_4 \rightarrow CF^+ + 3F + 2e^-$	2.296E–14	1.090	3.132E5	27.0	[j]	24, Table 15
20.	$e^- + CF_4 \rightarrow F^+ + CF_3 + 2e^-$	1.482E–13	0.9375	4.023E5	23.1	[i]	24, Table 15
21.	$e^- + CF_4 \rightarrow F^+ + CF_3^+ + 3e^-$	3.614E–17	1.413	3.966E5	36.0		24, Table 16
22.	$e^- + CF_4 \rightarrow F^+ + CF_2^+ + F + 3e^-$	1.809E–22	2.431	3.912E5	40.0		24, Table 16
23.	$e^- + CF_4 \rightarrow F^+ + CF^+ + 2F + 3e^-$	4.867E–30	3.880	3.531E5	42.0	[j]	24, Table

[a] Rate coefficients of form: $k_f = A\ T^B \exp(-C/T)$. Units for A depend on the order of the reaction, but are in molecules, cm and s. B is for temperature in K. Units for C are K. ε is the electron collision energy loss in eV.
[b] V indicates a vibrational excitation. If a number is given, it denotes the number of the vibrational mode.
[c] E indicates an electronic excitation. If a state designation is given, it identifies the excited state.
[d] The products of this reaction were guessed.
[e] The neutral products of this reaction were guessed.
[f] The negative ion produced in this reaction has been set to F^-.
[g] Indicate that a blended Arrhenius and Landau-Teller form for the rate expression was used: $k = A\ T^B \exp(-C\ T^{-1} + D\ T^{-1/3} + E\ T^{-2/3})$. The two parameters on this line are D and E.
[h] This is an indirect vibrational excitation. The reaction rate from the indicated reference has been multiplied by a factor of 0.8.
[i] ε has been set to the reaction endothermicity.
[j] This reaction actually produces F_2 rather than 2F.

							16
24.	$e^- + CF_4 \rightarrow CF_3 + F^-$	2.369E–8	–0.4893	5.876E4	3.0	[f]	24, Fig.34
25.	$e^- + CF_3 \rightarrow CF_2 + F + e^-$	4.163E–4	–0.9407	1.301E5	3.8	[i]	26
26.	$e^- + CF_3 \rightarrow CF_3^+ + 2e^-$	1.4E–11	0.6481	1.133E5	10.0	[k]	24, 27
27.	$e^- + CF_3 \rightarrow CF_2^+ + F + 2e^-$	1.378E–10	0.4367	1.987E5	17.1		24, 27
28.	$e^- + CF_3 \rightarrow CF^+ + 2F + 2e^-$	5.005E–11	0.5060	2.455E5	21.4		24, 27
29.	$e^- + CF_3 \rightarrow F^+ + CF_2 + 2e^-$	5.581E–10	0.2896	3.336E5	21.3	[i]	24, 27
30.	$e^- + CF_3 \rightarrow CF_2 + F^-$	2.369E–8	–0.4893	5.876E4	0.40	[f, i]	copy CF_4
31.	$e^- + CF_2 \rightarrow CF_2 + e^-$	3.419E–4	–0.8606	9.01E4	5.6	E A $^1B_1$ [c]	25
32.	$e^- + CF_2 \rightarrow CF_2 + e^-$	1.795E–4	–0.838	4.225E4	2.2	E a $^3B_1$ [c]	25
33.	$e^- + CF_2 \rightarrow CF + F + e^-$	1.190E–16	1.309	1.446E5	5.4	[i]	copy CF_4
34.	$e^- + CF_2 \rightarrow CF_2^+ + 2e^-$	1.579E–11	0.6287	1.125E5	10.0		24, 27
35.	$e^- + CF_2 \rightarrow CF^+ + F + 2e^-$	2.454E–12	0.7803	1.602E5	14.23		24, 27
36.	$e^- + CF_2 \rightarrow F^+ + CF + 2e^-$	1.676E–9	0.2519	4.446E5	22.9	[i]	24, 27
37.	$e^- + CF_2 \rightarrow CF + F^-$	2.369E–8	–0.4893	5.876E4	1.9	[f, i]	copy CF_4
38.	$e^- + CF \rightarrow C + F + e^-$	1.190E–16	1.309	1.446E5	5.6	[i]	copy CF_4
39.	$e^- + CF \rightarrow CF^+ + 2e^-$	1.270E–13	1.038	1.027E5	9.11		27
40.	$e^- + CF \rightarrow C + F^-$	2.369E–8	–0.4893	5.876E4	2.1	[f, i]	copy CF_4
41.	$e^- + C \rightarrow e^- + C$	4.882E–6	–0.5042	2.459E4	1.264	E ^1D [c]	28
42.	$e^- + C \rightarrow e^- + C$	6.939E–7	–0.5041	4.163E4	2.684	E ^1S [c]	28
43.	$e^- + F \rightarrow e^- + F$	1.56E–6	–0.6504	166287.	12.7	E 3s ^4P [c, l]	29
44.	$e^- + F \rightarrow e^- + F$	5.93E–9	–0.0528	160465.	12.985	E 3s ^2P [c]	29
45.	$e^- + F \rightarrow F^+ + 2e^-$	7.489E–13	0.8595	2.042E5	17.42		30
46.	$e^- + SiF_4 \rightarrow SiF_4 + e^-$	4.78E–3	–1.351	4.704E3	0.032	V [b]	26
47.	$e^- + SiF_4 \rightarrow SiF_4 + e^-$	4.73E–3	–1.35	4.799E3	0.052	V [b]	26
48.	$e^- + SiF_4 \rightarrow SiF_4 + e^-$	2.947E–6	–0.4119	4.606E3	0.10	V [b]	26
49.	$e^- + SiF_4 \rightarrow SiF_3 + F + e^-$	2.268E–12	0.8182	1.302E5	7.25	[i]	26
50.	$e^- + SiF_4 \rightarrow SiF_2 + 2F + e^-$	1.223E–8	0.01834	1.86E5	11.9	[i, j]	26
51.	$e^- + SiF_4 \rightarrow SiF + 3F + e^-$	1.039E–16	1.187	2.203E5	18.6	[i, j]	copy CF_4
52.	$e^- + SiF_4 \rightarrow SiF_3^+ + 2e^- + F$	2.291E–11	0.6641	2.022E5	16.0		26
53.	$e^- + SiF_4 \rightarrow SiF_2^+ + 2F + 2e^-$	2.886E–11	0.5108	2.649E5	23.4	[i, j]	copy CF_4
54.	$e^- + SiF_4 \rightarrow SiF^+ + 2F + F + 2e^-$	2.296E–14	1.090	3.132E5	25.1	[i, j]	copy CF_4
55.	$e^- + SiF_4 \rightarrow F^+ + SiF_3 + 2e^-$	1.482E–13	0.9375	4.023E5	24.75	[i]	copy CF_4
56.	$e^- + SiF_4 \rightarrow SiF_3 + F^-$	1.245E–8	–0.3792	1.14E5	3.8	[i]	26
57.	$e^- + SiF_3 \rightarrow SiF_2 + F + e^-$	1.190E–16	1.309	1.446E5	4.6	[i]	copy CF_4
58.	$e^- + SiF_3 \rightarrow SiF + 2F + e^-$	1.039E–16	1.187	2.203E5	11.4	[i, j]	copy CF_4
59.	$e^- + SiF_3 \rightarrow SiF_3^+ + 2e^-$	3.265E–10	0.3633	1.185E5	9.60		32
60.	$e^- + SiF_3 \rightarrow SiF_2^+ + F + 2e^-$	1.939E–10	0.4660	1.752E5	15.90		32
61.	$e^- + SiF_3 \rightarrow SiF^+ + 2F + 2e^-$	7.0474–12	0.6944	1.974E5	17.43		32
62.	$e^- + SiF_3 \rightarrow Si^+ + 3F + 2e^-$	1.801E–10	0.3139	3.343E5	25.6	[i, j]	32
63.	$e^- + SiF_3 \rightarrow SiF_2 + F^-$	1.245E–8	–0.3792	1.14E5	3.0		copy SiF_4
64.	$e^- + SiF_2 \rightarrow SiF + F + e^-$	1.190E–16	1.309	1.446E5	6.8	[i]	copy CF_4
65.	$e^- + SiF_2 \rightarrow SiF_2^+ + 2e^-$	2.620E–9	0.2530	1.348E5	10.80		33
66.	$e^- + SiF_2 \rightarrow SiF^+ + F + 2e^-$	3.597E–13	0.9855	1.592E5	15.2		33
67.	$e^- + SiF_2 \rightarrow Si^+ + 2F + 2e^-$	7.940E–11	0.4722	3.459E5	22.4		33
68.	$e^- + SiF_2 \rightarrow SiF + F^-$	1.245E–8	–0.3792	1.14E5	3.0		copy SiF_4
69.	$e^- + SiF \rightarrow Si + F + e^-$	1.190E–16	1.309	1.446E5	6.0	[i]	copy CF_4
70.	$e^- + SiF \rightarrow SiF^+ + 2e^-$	2.963E–9	0.3258	9.052E4	7.26		34

[k] The reaction rate from the indicated reference has been multiplied by a factor of 3.
[l] Metastable state.

71.	$e^- + SiF \rightarrow Si^+ + F + 2e^-$	3.888E–10	0.4391	1.628E5	14.3		34
72.	$e^- + SiF \rightarrow Si + F^+ + 2e^-$	7.116E–11	0.3962	2.580E5	23.1		34
73.	$e^- + SiF \rightarrow Si + F^-$	1.245E–8	–0.379	1.14E5	3.0		copy SiF_4
74.	$e^- + O_2 \rightarrow O_2 + e^-$	3.1064E–7	–0.967	–2.21E4	0.19	V, part 1[m]	36
75.	$e^- + O_2 \rightarrow O_2 + e^-$	3.070E–4	–1.02	5.332E4	0.19	V, part 2[m]	36
76.	$e^- + O_2 \rightarrow O_2 + e^-$	4.792E–5	–0.9297	5.65E4	0.38	V [n]	36
77.	$e^- + O_2 \rightarrow O_2 + e^-$	2.987E–4	–1.133	5.656E4	0.57	V [n]	36
78.	$e^- + O_2 \rightarrow O_2 + e^-$	1.88E–3	–1.338	5.662E4	0.75	V [n]	36
79.	$e^- + O_2 \rightarrow O_2 + e^-$	1.426E–6	–0.5896	5.782E4	0.98	E $a^1\Delta_g$ [c]	36
80.	$e^- + O_2 \rightarrow O_2 + e^-$	3.020E–7	–0.5739	6.214E4	1.63	E $b^1\Sigma_g^+$ [c]	36
81.	$e^- + O_2 \rightarrow O_2 + e^-$	2.288E–10	0.4019	6.865E4	6.2	E [o]	35
82.	$e^- + O_2 \rightarrow O + O + e^-$	1.88E–3	–1.267	5.466E4	4.5	[p]	36
83.	$e^- + O_2 \rightarrow O + O + e^-$	4.854E–7	–0.4485	5.719E4	6.0	[p]	36
84.	$e^- + O_2 \rightarrow O + O + e^-$	4.247E–10	0.3654	5.611E4	8.4	[p]	36
85.	$e^- + O_2 \rightarrow O + O + e^-$	1.703E–16	1.29	7.557E4	10.0	[p]	36
86.	$e^- + O_2 \rightarrow O + O + e^-$	8.486E–16	1.121	7.535E4	14.7	[p]	36
87.	$e^- + O_2 \rightarrow O_2^+ + 2e^-$	1.404E–15	1.419	6.549E4	12.1		36
88.	$e^- + O \rightarrow O + e^-$	9.606E–7	–0.4471	5.505E4	1.97	E ^1D [c]	38
89.	$e^- + O \rightarrow O + e^-$	2.736E–8	–0.3368	6.291E4	4.19	E ^1S [c]	38
90.	$e^- + O \rightarrow O^+ + 2e^-$	2.314E–15	1.328	6.65E4	13.6		38
91.	$e^- + CO \rightarrow CO + e^-$	0.06564	–1.434	2.253E4	0.27	V [b]	39
92.	$e^- + CO \rightarrow CO + e^-$	0.03333	–1.433	2.149E4	0.53	V [n]	39
93.	$e^- + CO \rightarrow CO + e^-$	0.01319	–1.421	2.077E4	0.79	V [n]	39
94.	$e^- + CO \rightarrow CO + e^-$	0.0136	–1.471	2.149E4	1.04	V [n]	39
95.	$e^- + CO \rightarrow e^- + CO$	4.056E–5	–0.647	9.68E4	6.22	E $a^3\Pi_r$ [c]	39
96.	$e^- + CO \rightarrow e^- + CO$	5.203E–4	–0.9815	1.35E5	6.8	E $a'^3\Sigma^+$ [c]	39
97.	$e^- + CO \rightarrow e^- + CO$	1.742E–6	–0.3538	1.776E5	7.9	E $A^1\Pi$ [c]	39
98.	$e^- + CO \rightarrow e^- + CO$	6.127E–5	–0.8693	1.685E5	10.4	E $b^3\Sigma^+$ [c]	39
99.	$e^- + CO \rightarrow e^- + CO$	4.756E–7	–0.2813	2.052E5	10.6	E $C^1\Sigma^+$ + $E^1\Pi$ [c]	39
100.	$e^- + CO \rightarrow C + O + e^-$	3.70E–12	0.731	125795.	13.5		40
101.	$e^- + CO \rightarrow CO^+ + 2e^-$	2.199E–7	–0.0487	2.762E5	14.0		41
	dissociative recombinations						
102.	$e^- + CF_3^+ \rightarrow CF_2 + F$	4.0E–8	0.0	0.0	0.0		Estimate
103.	$e^- + CF_2^+ \rightarrow CF + F$	4.0E–8	0.0	0.0	0.0		Estimate
104.	$e^- + CF^+ \rightarrow C + F$	4.0E–8	0.0	0.0	0.0		Estimate
	$e^- + SiF_3^+ \rightarrow SiF_2 + F$	4.0E–8	0.0	0.0	0.0		Estimate

[m] The rate expression for excitation into the first vibrationally excited state has been divided into two parts.
[n] Excitation into higher vibrationally-excited states.
[o] This electronic excitation is a sum over the $B^3\Sigma_u^-$, $A^3\Sigma_u^+$, $C^3\Delta_u$, and $c^1\Sigma_u^-$ states.
[p] Represents production of electronically excited O_2 which then dissociates.

105.	$e^- + SiF_2^+ \rightarrow SiF + F$	4.0E–8	0.0	0.0	0.0		Estimate
106.	$e^- + SiF^+ \rightarrow Si + F$	4.0E–8	0.0	0.0	0.0		Estimate
107.	$e^- + CO^+ \rightarrow C + O$	4.0E–8	0.0	0.0	0.0		Estimate
108.	$e^- + O_2^+ \rightarrow 2O$	4.0E–8	0.0	0.0	0.0		Estimate
109.	detachment reactions						
110.	$F^- + CF_3 \rightarrow CF_4 + e^-$	4.0E–10	0.0	0.0			Estimate
111.	$F^- + CF_2 \rightarrow CF_3 + e^-$	3.0E–10	0.0	0.0			Estimate
112.	$F^- + CF \rightarrow CF_2 + e^-$	2.0E–10	0.0	0.0			Estimate
113.	$F^- + C \rightarrow CF + e^-$	1.0E–10	0.0	0.0			Estimate
114.	$F^- + F \rightarrow 2F + e^-$	1.0E–10	0.0	0.0		[j]	Estimate
115.	$F^- + SiF_3 \rightarrow SiF_4 + e^-$	4.0E–10	0.0	0.0			Estimate
116.	$F^- + SiF_2 \rightarrow SiF_3 + e^-$	3.0E–10	0.0	0.0			Estimate
117.	$F^- + SiF \rightarrow SiF_2 + e^-$	2.0E–10	0.0	0.0			Estimate
118.	$F^- + Si \rightarrow SiF + e^-$	1.0E–10	0.0	0.0			Estimate
119.	$F^- + O \rightarrow F + O + e^-$	1.0E–10	0.0	0.0		[q]	Estimate
120.	charge exchange reactions $O^+ + O_2 \rightarrow O_2^+ + O$	2.10E–11	0.0	0.0			42
121.	$F^+ + O_2 \rightarrow O_2^+ + F$	7.007E–10	0.0	0.0			42

[q] The products of this reaction are really FO + e^-, but FO is not included in the mechanism.

	ion-ion neutralization				
122.	$F^- + CF_3^+ \rightarrow 2F + CF_2$	4.0E–7	–0.5	0.0	Estimate
123.	$F^- + CF_2^+ \rightarrow F + CF_2$	4.0E–7	–0.5	0.0	Estimate
124.	$F^- + CF^+ \rightarrow 2F + C$	4.0E–7	–0.5	0.0	Estimate
125.	$F^- + F^+ \rightarrow 2F$	4.0E–7	–0.5	0.0	Estimate
126.	$F^- + Si^+ \rightarrow F + Si$	4.0E–7	–0.5	0.0	Estimate
127.	$F^- + SiF^+ \rightarrow F + SiF$	4.0E–7	–0.5	0.0	Estimate
128.	$F^- + SiF_2^+ \rightarrow 2F + SiF$	4.0E–7	–0.5	0.0	Estimate
129.	$F^- + SiF_3^+ \rightarrow 2F + SiF_2$	4.0E–7	–0.5	0.0	Estimate
130.	$F^- + O^+ \rightarrow F + O$	4.0E–7	–0.5	0.0	Estimate
131.	$F^- + O_2^+ \rightarrow F + O_2$	4.0E–7	–0.5	0.0	Estimate
132.	$F^- + CO^+ \rightarrow F + CO$	4.0E–7	–0.5	0.0	Estimate

Table 3. Surface reaction mechanism for C_2F_6 plasma etching of silicon. [a]

No.	Reaction	A	C	h [b]	Notes[c]
	Direct etch by F atoms				
1.	$F + 0.25Si(B) \rightarrow 0.25SiF_4$	0.116	1250.		S [d]
	Adsorption of F atoms				
2.	$F + 0.5Si(S) \rightarrow 0.5Si\_F_2(S)$	0.2	0.0		S [e,f]
	Ion-enhanced etch				
3.	$CF_2^+ + e^- + \#Si(B) + 2\#Si\_F_2(S) \rightarrow CF_2 + \#SiF_4 + 2\#Si(S)$	1.0	0.0	0.860	B [g]
4.	$CF_3^+ + e^- + \#Si(B) + 2\#Si\_F_2(S) \rightarrow CF_3 + \#SiF_4 + 2\#Si(S)$	1.0	0.0	1.186	B [g]
5.	$CF^+ + e^- + \#Si(B) + 2\#Si\_F_2(S) \rightarrow CF + \#SiF_4 + 2\#Si(S)$	1.0	0.0	0.533	B [g]
6.	$F^+ + e^- + \#Si(B) + 2\#Si\_F_2(S) \rightarrow F + \#SiF_4 + 2\#Si(S)$	1.0	0.0	0.327	B [g]
7.	$Si^+ + e^- + \#Si(B) + 2\#Si\_F_2(S) \rightarrow Si + \#SiF_4 + 2\#Si(S)$	1.0	0.0	0.483	B
8.	$SiF^+ + e^- + \#Si(B) + 2\#Si\_F_2(S) \rightarrow SiF + \#SiF_4 + 2\#Si(S)$	1.0	0.0	0.810	B
9.	$SiF_2^+ + e^- + \#Si(B) + 2\#Si\_F_2(S) \rightarrow SiF_2 + \#SiF_4 + 2\#Si(S)$	1.0	0.0	1.136	B
10.	$SiF_3^+ + e^- + \#Si(B) + 2\#Si\_F_2(S) \rightarrow SiF_3 + \#SiF_4 + 2\#Si(S)$	1.0	0.0	1.463	B
11.	$O^+ + e^- + \#Si(B) + 2\#Si\_F_2(S) \rightarrow O + \#SiF_4 + 2\#Si(S)$	1.0	0.0	0.275	B [g]
12.	$O_2^+ + e^- + \#Si(B) + 2\#Si\_F_2(S) \rightarrow O_2 + \#SiF_4 + 2\#Si(S)$	1.0	0.0	0.550	B [g]
13.	$CO^+ + e^- + \#Si(B) + 2\#Si\_F_2(S) \rightarrow CO + \#SiF_4 + 2\#Si(S)$	1.0	0.0	0.482	B [g]
	Ion neutralizations on open sites,				
14.	$CF_3^+ + e^- + Si(S) \rightarrow CF_3 + Si(S)$	1.0	0.0		B
15.	$CF_2^+ + e^- + Si(S) \rightarrow CF_2 + Si(S)$	1.0	0.0		B
16.	$CF^+ + e^- + Si(S) \rightarrow CF + Si(S)$	1.0	0.0		B
17.	$O^+ + e^- + Si(S) \rightarrow O + Si(S)$	1.0	0.0		B
18.	$O_2^+ + e^- + Si(S) \rightarrow O_2 + Si(S)$	1.0	0.0		B
19.	$CO+ + e^- + Si(S) \rightarrow CO + Si(S)$	1.0	0.0		B
	Ion deposition reactions				
20.	$F^+ + e^- + 0.5Si(S) \rightarrow 0.5Si\_F_2(S)$	1.0	0.0		B [e]
21.	$Si^+ + e^- + Si(S) \rightarrow Si(B) + Si(S)$	1.0	0.0		B
22.	$SiF^+ + e^- + 0.5Si(S) \rightarrow 0.5Si\_F_2(S) + Si(B)$	1.0	0.0		B [e]
23.	$SiF_2^+ + e^- + Si(S) \rightarrow Si\_F_2(S) + Si(B)$	1.0	0.0		B
24.	$SiF_3^+ + e^- + 1.5Si(S) \rightarrow 1.5Si\_F_2(S) + Si(B)$	1.0	0.0		B [e]
	Radical abstraction/recombination reactions at surface				
25.	$Si + Si\_F_2(S) \rightarrow SiF_2 + Si(S)$	0.04	0.0		S
26.	$SiF + Si\_F_2(S) \rightarrow SiF_3 + Si(S)$	0.03	0.0		S
27.	$SiF_2 + Si\_F_2(S) \rightarrow SiF_4 + Si(S)$	0.02	0.0		S
28.	$SiF_3 + 0.5Si\_F_2(S) \rightarrow SiF_4 + 0.5Si(S)$	0.01	0.0		S [g]
29.	$C + Si\_F_2(S) \rightarrow CF_2 + Si(S)$	0.01	0.0		S
30.	$O \rightarrow 0.5O_2$	3.55E−4	0.0		S [h]

[a] Rate parameters of form: $k_f = A \exp(-C/T)$. Units for A depend on the reaction order. Units for C are Kelvin. # indicates a species with an ion energy dependent yield.

[b] Yield coefficients: yield = $h\,(E_{ion}^{0.5} - E_{th}^{0.5})$, where E_{th} is 4 eV.

[c] S in this column indicates that the rate parameters give a sticking coefficient. B indicates a Bohm reaction. Unless otherwise noted, rate parameters were estimated or fit in this work.

[d] From Ref. 44.

[e] The FORD option has been used to make this reaction first order in Si(S) coverage.

[f] Sticking coefficient from Ref.46.

[g] The FORD option has been used to make this reaction first order in $Si\_F_2(S)$ coverage.

[h] From Ref. 48

Table 4. Surface reaction mechanism for C_2F_6 plasma etching of silicon dioxide. [a]

No.	Reaction	A	C	h [b]	Notes[c]
	Direct etch by F atoms				
1.	$F + 0.25SiO_2(B) \rightarrow 0.25SiF_4 + 0.25O_2$	0.01582	1890.		S [d]
	Adsorption of radicals				
2.	$F + 0.5SiO_2(S) \rightarrow 0.5SiO_2\_F_2(S)$	0.02	0.0		S [e,f]
3.	$CF_2 + SiO_2(S) \rightarrow SiO_2\_CF_2(S)$	0.66	0.0		S [g]
4.	$CF_3 + 1.5SiO_2(S) \rightarrow SiO_2\_CF_2(S) + 0.5SiO_2\_F_2(S)$	0.2	0.0		S [e]
5.	$CF + 0.5SiO_2\_F_2(S) + 0.5SiO_2(S) \rightarrow SiO_2\_CF_2(S)$	1.0	0.0		S [e,h]
	Ion-enhanced etch				
6.	$CF_2^+ + e^- + \#SiO_2(B) + 2\#SiO_2\_F_2(S) \rightarrow CF_2 + \#SiF_4 + \#O_2 + 2\#SiO_2(S)$	1.0	0.0	0.066	B [h]
7.	$CF_3^+ + e^- + \#SiO_2(B) + 2\#SiO_2\_F_2(S) \rightarrow CF_3 + \#SiF_4 + \#O_2 + 2\#SiO_2(S)$	1.0	0.0	0.092	B [h]
8.	$CF^+ + e^- + \#SiO_2(B) + 2\#SiO_2\_F_2(S) \rightarrow CF + \#SiF_4 + \#O_2 + 2\#SiO_2(S)$	1.0	0.0	0.041	B [h]
9.	$F^+ + e^- + \#SiO_2(B) + 2\#SiO_2\_F_2(S) \rightarrow F + \#SiF_4 + \#O_2 + 2\#SiO_2(S)$	1.0	0.0	0.025	B [h]
10.	$Si^+ + e^- + \#SiO_2(B) + 2\#SiO_2\_F_2(S) \rightarrow Si + \#SiF_4 + \#O_2 + 2\#SiO_2(S)$	1.0	0.0	0.037	B [h]
11.	$SiF^+ + e^- + \#SiO_2(B) + 2\#SiO_2\_F_2(S) \rightarrow SiF + \#SiF_4 + \#O_2 + 2\#SiO_2(S)$	1.0	0.0	0.062	B [h]
12.	$SiF_2^+ + e^- + \#SiO_2(B) + 2\#SiO_2\_F_2(S) \rightarrow SiF_2 + \#SiF_4 + \#O_2 + 2\#SiO_2(S)$	1.0	0.0	0.088	B [h]
13.	$SiF_3^+ + e^- + \#SiO_2(B) + 2\#SiO_2\_F_2(S) \rightarrow SiF_3 + \#SiF_4 + \#O_2 + 2\#SiO_2(S)$	1.0	0.0	0.113	B [h]
14.	$O^+ + e^- + \#SiO_2(B) + 2\#SiO_2\_F_2(S) \rightarrow O + \#SiF_4 + \#O_2 + 2\#SiO_2(S)$	1.0	0.0	0.021	B [h]
15.	$O_2^+ + e^- + \#SiO_2(B) + 2\#SiO_2\_F_2(S) \rightarrow O_2 + \#SiF_4 + \#O_2 + 2\#SiO_2(S)$	1.0	0.0	0.042	B [h]
16.	$CO^+ + e^- + \#SiO_2(B) + 2\#SiO_2\_F_2(S) \rightarrow CO + \#SiF_4 + \#O_2 + 2\#SiO_2(S)$	1.0	0.0	0.037	B [h]
17.	$CF_2^+ + e^- + \#SiO_2(B) + 2\#SiO_2\_CF_2(S) \rightarrow CF_2 + \#SiF_4 + 2\#CO + 2\#SiO_2(S)$	1.0	0.0	0.067	B [i]
18.	$CF_3^+ + e^- + \#SiO_2(B) + 2\#SiO_2\_CF_2(S) \rightarrow CF_3 + \#SiF_4 + 2\#CO + 2\#SiO_2(S)$	1.0	0.0	0.093	B [i]
19.	$CF^+ + e^- + \#SiO_2(B) + 2\#SiO_2\_CF_2(S) \rightarrow CF + \#SiF_4 + 2\#CO + 2\#SiO_2(S)$	1.0	0.0	0.042	B [i]
20.	$F^+ + e^- + \#SiO_2(B) + 2\#SiO_2\_CF_2(S) \rightarrow F + \#SiF_4 + 2\#CO + 2\#SiO_2(S)$	1.0	0.0	0.026	B [i]

[a] Sticking and Bohm coefficients of form: $k_f = A \exp(-C/T)$. Units for C are Kelvin. # indicates a species with an ion energy dependent yield.

[b] Yield coefficients: yield = h $(E_{ion}^{0.5} - E_{th}^{0.5})$, where E_{th} is 4 eV.

[c] S in this column indicates that the rate parameters give a sticking coefficient. B in this column indicates a Bohm reaction. Unless otherwise noted, rate parameters were estimated or fit in this work.

[d] From Ref. 45.

[e] The FORD option has been used to make this reaction first order in $SiO_2(S)$ coverage.

[f] Sticking coefficient from Ref. 46.

[g] Sticking coefficient from Ref. 47.

[h] The FORD option has been used to make this reaction first order in $SiO_2\_F_2(S)$ coverage.

[i] The FORD option has been used to make this reaction first order in $SiO_2\_CF_2(S)$ coverage.

21.	$Si^+ + e^- + \#SiO_2(B) + 2\#SiO_2\_CF_2(S) \rightarrow Si + \#SiF_4 + 2\#CO + 2\#SiO_2(S)$	1.0	0.0	0.038	B [i]
22.	$SiF^+ + e^- + \#SiO_2(B) + 2\#SiO_2\_CF_2(S) \rightarrow SiF + \#SiF_4 + 2\#CO + 2\#SiO_2(S)$	1.0	0.0	0.063	B [i]
23.	$SiF_2^+ + e^- + \#SiO_2(B) + 2\#SiO_2\_CF_2(S) \rightarrow SiF_2 + \#SiF_4 + 2\#CO + 2\#SiO_2(S)$	1.0	0.0	0.090	B [i]
24.	$SiF_3^+ + e^- + \#SiO_2(B) + 2\#SiO_2\_CF_2(S) \rightarrow SiF_3 + \#SiF_4 + 2\#CO + 2\#SiO_2(S)$	1.0	0.0	0.116	B [i]
25.	$O^+ + e^- + \#SiO_2(B) + 2\#SiO_2\_CF_2(S) \rightarrow O + \#SiF_4 + 2\#CO + 2\#SiO_2(S)$	1.0	0.0	0.021	B [i]
26.	$O_2^+ + e^- + \#SiO_2(B) + 2\#SiO_2\_CF_2(S) \rightarrow O_2 + \#SiF_4 + 2\#CO + 2\#SiO_2(S)$	1.0	0.0	0.044	B [i]
27.	$CO^+ + e^- + \#SiO_2(B) + 2\#SiO_2\_CF_2(S) \rightarrow CO + \#SiF_4 + 2\#CO + 2\#SiO_2(S)$	1.0	0.0	0.038	B [i]
	Ion neutralizations on open sites:				
28.	$CF_3^+ + e^- + SiO_2(S) \rightarrow CF_3 + SiO_2(S)$	0.8	0.0		B
29.	$CF_2^+ + e^- + SiO_2(S) \rightarrow CF_2 + SiO_2(S)$	0.8	0.0		B
30.	$CF^+ + e^- + SiO_2(S) \rightarrow CF + SiO_2(S)$	0.8	0.0		B
31.	$F^+ + e^- + SiO_2(S) \rightarrow F + SiO_2(S)$	0.8	0.0		B
32.	$Si^+ + e^- + SiO_2(S) \rightarrow Si + SiO_2(S)$	1.0	0.0		B
33.	$SiF^+ + e^- + SiO_2(S) \rightarrow SiF + SiO_2(S)$	0.8	0.0		B
34.	$SiF_2^+ + e^- + SiO_2(S) \rightarrow SiF_2 + SiO_2(S)$	0.8	0.0		B
35.	$SiF_3^+ + e^- + SiO_2(S) \rightarrow SiF_3 + SiO_2(S)$	0.8	0.0		B
36.	$O^+ + e^- + SiO_2(S) \rightarrow 0.5O_2 + SiO_2(S)$	1.0	0.0		B
37.	$O_2^+ + e^- + SiO_2(S) \rightarrow O_2 + SiO_2(S)$	1.0	0.0		B
38.	$CO^+ + e^- + SiO_2(S) \rightarrow CO + SiO_2(S)$	1.0	0.0		B
	Ion deposition reactions:				
39.	$CF_3^+ + e^- + 1.5SiO_2(S) \rightarrow SiO_2\_CF_2(S) + 0.5SiO_2\_F_2(S)$	0.2	0.0		B [e]
40.	$CF_2^+ + e^- + SiO_2(S) \rightarrow SiO_2\_CF_2(S)$	0.2	0.0		B
41.	$CF^+ + e^- + SiO_2\_F_2(S) + 0.5SiO_2(S) \rightarrow SiO_2\_CF_2(S) + 0.5SiO_2\_F_2(S)$	0.2	0.0		B [e]
42.	$F^+ + e^- + 0.5SiO_2(S) \rightarrow 0.5SiO_2\_F_2(S)$	0.2	0.0		B [e]
43.	$SiF^+ + e^- + 0.5SiO_2(S) \rightarrow Si + 0.5SiO_2\_F_2(S)$	0.2	0.0		B [e]
44.	$SiF_2^+ + e^- + SiO_2(S) \rightarrow Si + SiO_2\_F_2(S)$	0.2	0.0		B
45.	$SiF_3^+ + e^- + 1.5SiO_2(S) \rightarrow Si + 1.5SiO_2\_F_2(S)$	0.2	0.0		B [e]
	Radical abstraction/recombination reactions at surface				
46.	$F + 0.5SiO_2\_CF_2(S) \rightarrow 0.5CF_4 + 0.5SiO_2(S)$	0.01	0.0		S [i]
47.	$Si + SiO_2\_CF_2(S) \rightarrow CF + SiF + SiO_2(S)$	0.04	0.0		S
48.	$SiF + SiO_2\_CF_2(S) \rightarrow SiF_2 + CF + SiO_2(S)$	0.03	0.0		S
49.	$SiF_3 + SiO_2\_CF_2(S) \rightarrow SiF_4 + CF + SiO_2(S)$	0.01	0.0		S
50.	$Si + SiO_2\_F_2(S) \rightarrow SiF_2 + SiO_2(S)$	0.04	0.0		S
51.	$SiF + SiO_2\_F_2(S) \rightarrow SiF_3 + SiO_2(S)$	0.03	0.0		S,
52.	$SiF_2 + SiO_2\_F_2(S) \rightarrow SiF_4 + SiO_2(S)$	0.02	0.0		S
53.	$SiF_3 + 0.5SiO_2\_F_2(S) \rightarrow SiF_4 + 0.5SiO_2(S)$	0.01	0.0		S [h]
54.	$C + SiO_2\_F_2(S) \rightarrow CF_2 + SiO_2(S)$	0.01	0.0		S
55.	$O \rightarrow 0.5O_2$	3.55E–4	0.0		S [j]

[j] From Ref. 48

4.2. Comparisons with Experiment

The C_2F_6/oxide reaction mechanism was developed and tested with the widest range of experimental data. These include measurements of etch rates in all three reactors, electron densities, negative ion densities, relative densities of CF, CF_2 SiF, and SiF_2, gas temperatures, and ion current densities.

As summarized in Table 5, we have attained very good overall agreement between the predictions of the model and experiment. A three-part scale is used to rate the comparisons, with ✓ indicating good agreement, **O** indicating some agreement, and ✖ indicating poor agreement. If these are scored as 3 points, 2 points, and 1 point, respectively, the average is a very favorable 2.66. Figures of all these comparisons are shown below. Rather than attempt to provide experimental details here, we refer the reader to the experimentalists and their publications.

4.2.1. Etch Rates

Figure 6 shows a comparison between experimental C_2F_6 etch rates [15] and simulations for blanket oxide wafers in Reactor IB over a wide range of conditions. These conditions are given in Table 6, roughly in order of increasing power. Runs 8-13 represent repeats of the base conditions separated in time. From these repeats, we estimate a ~10% uncertainty in these experimental etch rates. Taken as a whole, there is good agreement between the model and experiments, although the etch rates predicted by the model for this reactor tend to be a little on the low side. This was deliberately done as a compromise to prevent the predicted etch rates for reactors II and III from being too high, and is reflected in the average difference between model and experimental etch rates of –72 nm/min, with a standard deviation about that mean of 115.

Table 5. Summary of Aurora comparisons to experimental data for C_2F_6 plasmas.

Reactor	Species	Parameter varied	Direction of trend	Magnitude of trend	Absolute number
III	etch rate	overall	✓	✓	✓
III	etch rate	flow rate	✓	O	✓
III	etch rate	bias power	✓	✓	✓
IB	etch rate	overall	✓	✓	✓
IB	etch rate	power	O	✓	✓
IB	etch rate	pressure	O	✓	✓
IB	etch rate	bias power	✓	✓	✓
II	etch rate	overall	✓	O	✓
II	etch rate	power	✓	✓	✓
II	etch rate	pressure	O	O	✓
II	etch rate	flow rate	✓	O	✓
II	etch rate	bias voltage	✓	✓	✓
IA	e^-	power	O	✓	✓
IA	e^-	pressure	O	✓	✓
IA	e^-	bias power	O	✓	✓
IA	F^-	power	O	✖	✓
IA	F^-	pressure	✓	✓	✓
IA	F^-	bias power	O	✓	✓
IA	CF	power	✓	✓	--
IA	CF	pressure	O	✓	--
IA	CF	bias power	✓	✓	--
IA	CF_2	power	✓	O	--
IA	CF_2	pressure	✓	O	--
IA	CF_2	bias power	✓	✓	--
IA	Gas Temp.	power	✓	✓	O
IA	Gas Temp.	pressure	✓	✓	O
IA	Gas Temp.	bias power	✖	✓	O
IA	SiF	power	✖	✓	--
IA	SiF	pressure	O	O	--
IA	SiF	bias power	✓	✓	--
IA	SiF	C_2F_6/O_2 MF	✓	✓	--
IA	SiF_2	power	✖	✓	--
IA	SiF_2	pressure	O	O	--
IA	SiF_2	bias power	✓	✓	--
II	ICD	power	✓	✓	✓
II	ICD	pressure	O	O	✓
II	ICD	flow rate	✓	O	✓

✓ = Good, O = Okay, ✖ = Poor

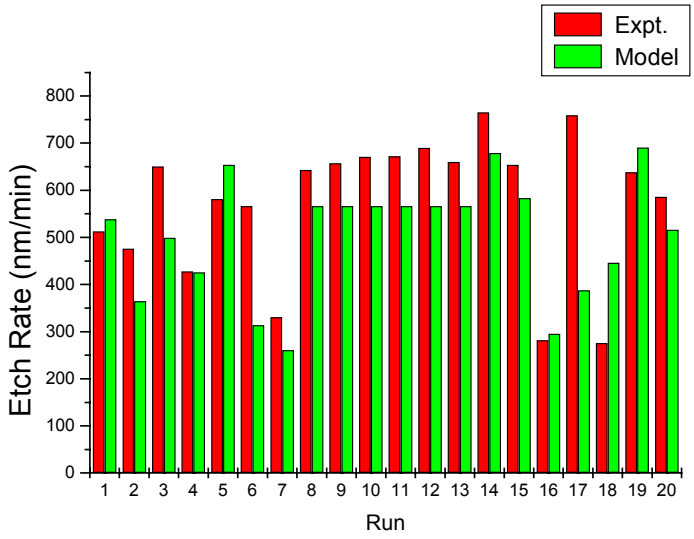

Figure 6. Oxide etch rate comparisons between model and experiment for C_2F_6 in Reactor IB. Experimental conditions given in Table 6. Data generally in order of increasing power.

Table 6. Conditions for C_2F_6 plasma etching of oxide shown in Figure 6 for Reactor IB.

Run No.	**Plasma Power** (Watts)	**Pressure** (mTorr)	**Bias Power** (Watts)
1	204.66	15	85
2	277	8	48
3	277	8	125
4	277	20	48
5	277	20	125
6	350	5.20	85
7	350	15	22.13
8–13	350	15	85
14	350	15	147.87
15	350	24.80	85
16	455	8	48
17	455	8	125
18	455	20	48
19	455	20	125
20	495.34	15	85

Within this data set, there are subsets of runs that illustrate etch rate trends with one particular variable, i.e. where all but one of the conditions are held constant. As shown in Figure 7, the experimental etch rate (runs 1, 8-13, and 20) initially increases with power, then decreases at 15 mTorr, 85 W bias power, and 10 sccm C_2F_6.. The simulations reproduce this trend, but not as strongly. There are also four other data pairs where only the power is changed. In these cases, as the power is increased, the observed etch rates show trends of ↓↑↓↑ for these data pairs, whereas the simulations show ↓↓↑↑.

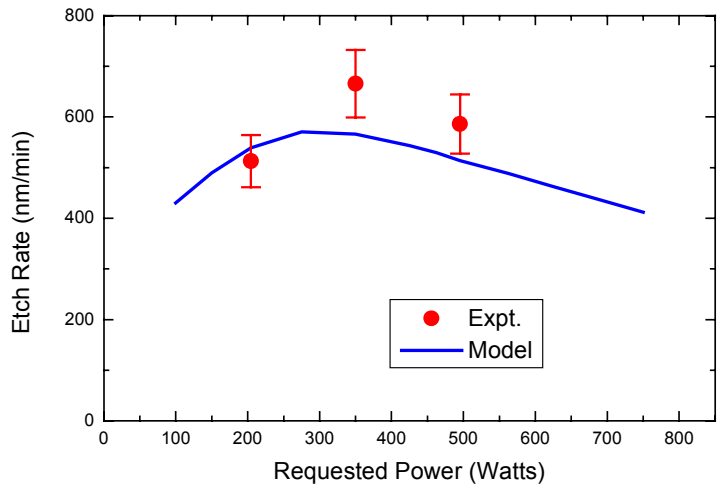

Figure 7. Blanket oxide etch rates as a function of plasma power in Reactor IB.

Similarly, Figure 8 shows that the experimental etch rate (runs 6, 8-13, and 15) increases slightly with increasing pressure, then levels off or decreases slightly at 350 W plasma power, 85 W bias power, and 10 sccm C_2F_6. The simulations reproduce this behavior, with a stronger dependence at low pressures. However, there are four other cases in which only the pressure is changed where experimental trend is down and the model trend is up. These figures illustrate the complexity of this system, where simple rules about trends do not apply. Even the direction of dependence of the etch rate on parameters such as power or pressure depend on other parameters.

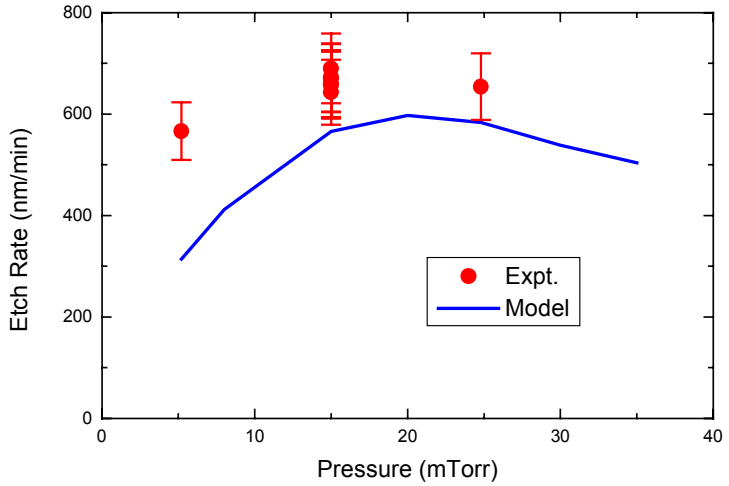

Figure 8. Blanket oxide etch rates as a function of pressure in Reactor IB.

Figure 9 shows the dependence of etch rate on bias power (Runs 7-14) at 350 W plasma power, 15 mTorr, and 10 sccm C_2F_6. For this parameter, both model and experiment agree that increased bias leads to increased etch rate. In addition to the comparisons shown, there are four pairs of runs where only the bias power differs. In all four cases, an increase in bias power is accompanied by a substantial increase in etch rate, although model and experiment sometimes disagree on the magnitude of the change.

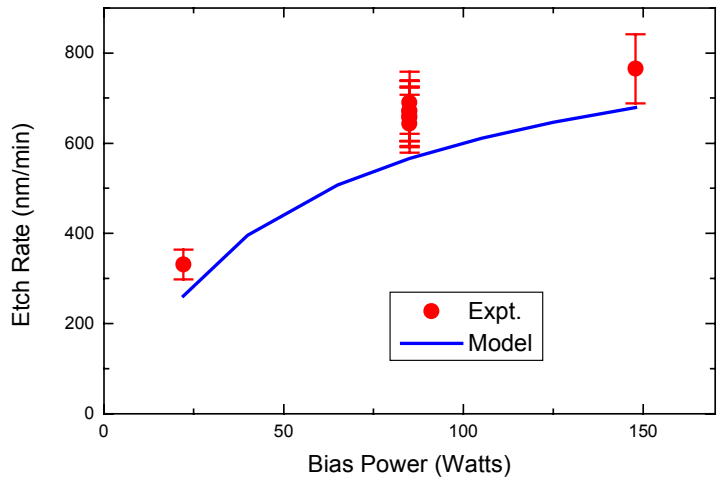

Figure 9. Blanket oxide etch rates as a function of bias power in Reactor IB.

Figure 10 shows a more limited set of etch rate data for Reactor III, [49] with the corresponding conditions given in Table 7. The agreement between experiment and model is very good, with some simulated etch rates being higher and some lower than experimentally observed. The combination of runs 1 and 2 with runs 4 and 5, shows that the etch rate is most strongly dependent on C_2F_6 flow rate. In contrast with the observations for Reactor I, runs 3 and 4 in Reactor III show only a minor dependence on bias power. Although two parameters were changed at once, the fact that runs 1 and 3 have nearly the same etch rates suggests that, in this case, the etch rate may also have only a minor dependence on plasma power and pressure. Overall, these trends suggest that Reactor III is being operated in a regime where the etch rate is limited by the etchant supply rate, and performance is less sensitive to variations in power and pressure.

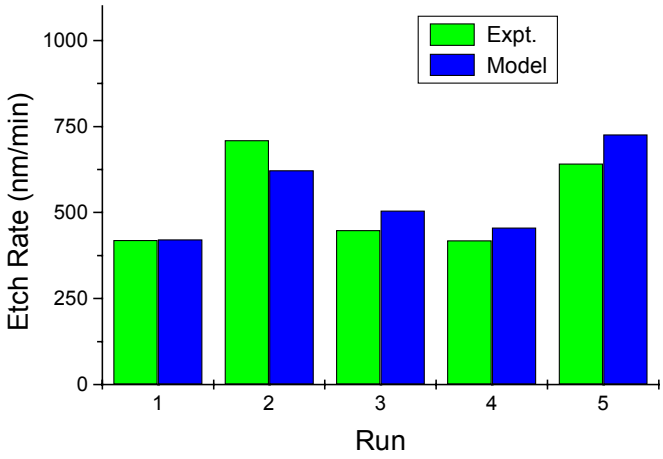

Figure 10. Oxide etch rates for a C_2F_6 plasma in Reactor III.

Table 7. Conditions for C_2F_6 plasma etching of oxide shown in Figure 10 for Reactor III.

Run No.	**Plasma Power** (Watts)	**Pressure** (mTorr)	**Bias Power** (Watts)	**Flow Rate** (sccm)
1	1550	10	1800	20
2	1550	10	1800	40
3	1650	30	1800	20
4	1650	30	1000	20
5	1650	30	1000	40

For Reactor II, etch rate data over a wide range of conditions were available [18,20]. Figure 11 shows etch rates as a function of power at three different pressures and four different flow rates. For the flow rate of 30 sccm, two sets of experimental data taken at the same conditions were available. Comparing these two sets of data yielded an estimated uncertainty for these etch rate experiments of ±15%, which is used in the graphs. The experimental data in Figure 11 clearly show that etch rates increase with power, except at the highest power and lowest pressure, where it levels off or drops somewhat. (This can be hard to see amidst the overlapping points in the graphs.) This is successfully reproduced by the model, as is the overall magnitude of the etch rates.

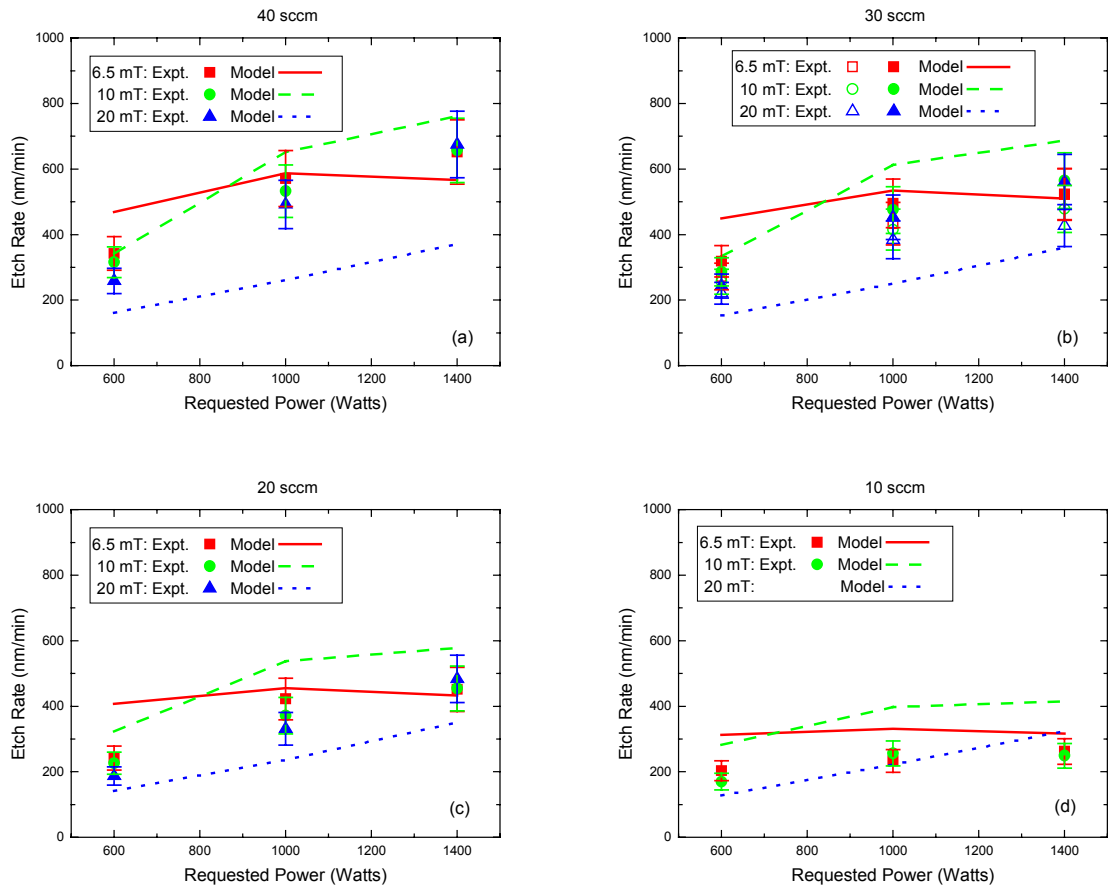

Figure 11. Oxide etch rates for C_2F_6 as a function of plasma power for three different pressures and four different flow rates in Reactor II. In (b), open and closed symbols represent older and newer sets of data.

Figure 12 shows the etch rate data in Figure 11(b), but now plotted as a function of total pressure. The 30 sccm flow rate has two sets of experimental data, and illustrates how the experimental data sets sometimes show somewhat different pressure dependencies. Analogous plots at the other flow rates are not included. The pressure dependencies, shown directly in Figure 12 and less directly in Figure 11, are complex. Most of the experimental data indicate that the etch rate should decrease slightly with increasing pressure. But the newer set of data at the highest power show evidence of a slight maximum. The simulations only match the pressure dependencies moderately well; many of the trends are reproduced, but are too strong. Attempts to raise the predicted etch rates (and ion current densities) at high pressures by adjusting rate parameters unfortunately resulted in even flatter power dependencies for the electron densities in Reactor I. The current mechanism represents a compromise. The presence of a maximum in the simulated etch rate pressure dependence for Reactor II is probably caused by the need to reproduce the etch rate data in Figure 8 for Reactor I, which showed a distinct maximum. But we note that there were difficulties in matching the pressure dependencies for that reactor too, so this may be indicative of a limitation in our approach of using 0D models for these systems.

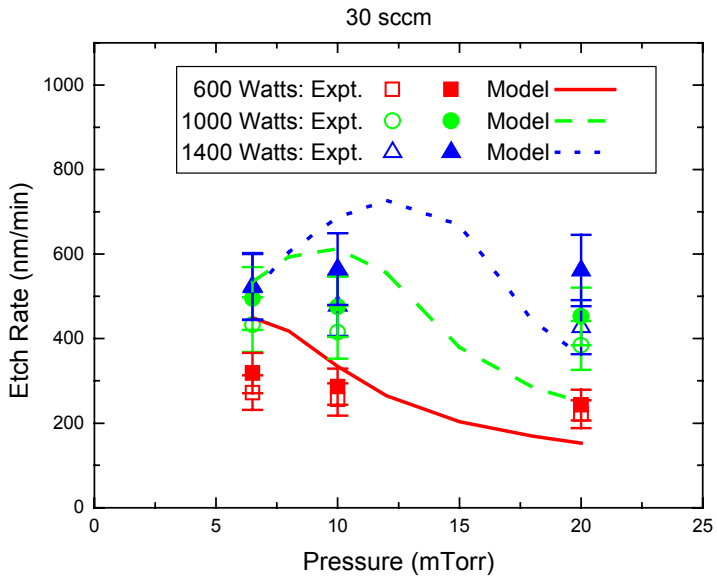

Figure 12. Oxide etch rates for C_2F_6 as a function of pressure for three different powers (30 sccm) in Reactor II. Open and closed symbols represent older and newer sets of data.

Figure 13 shows etch rates as a function of flow rate for different powers and pressures. The model successfully reproduces the trends of increasing etch rate with increasing flow rate, and generally flatter dependencies at lower powers. Comparisons at 6.5 and 20 mTorr are complicated by the problems with the pressure dependence discussed above. Figure 14 shows etch rates as a function of bias voltage for two different flow rates at 1400 W plasma power and 6.5 mTorr. In this case, the model successfully reproduces the magnitudes of the etch rates and their increase with increasing bias, although the model is somewhat flatter.

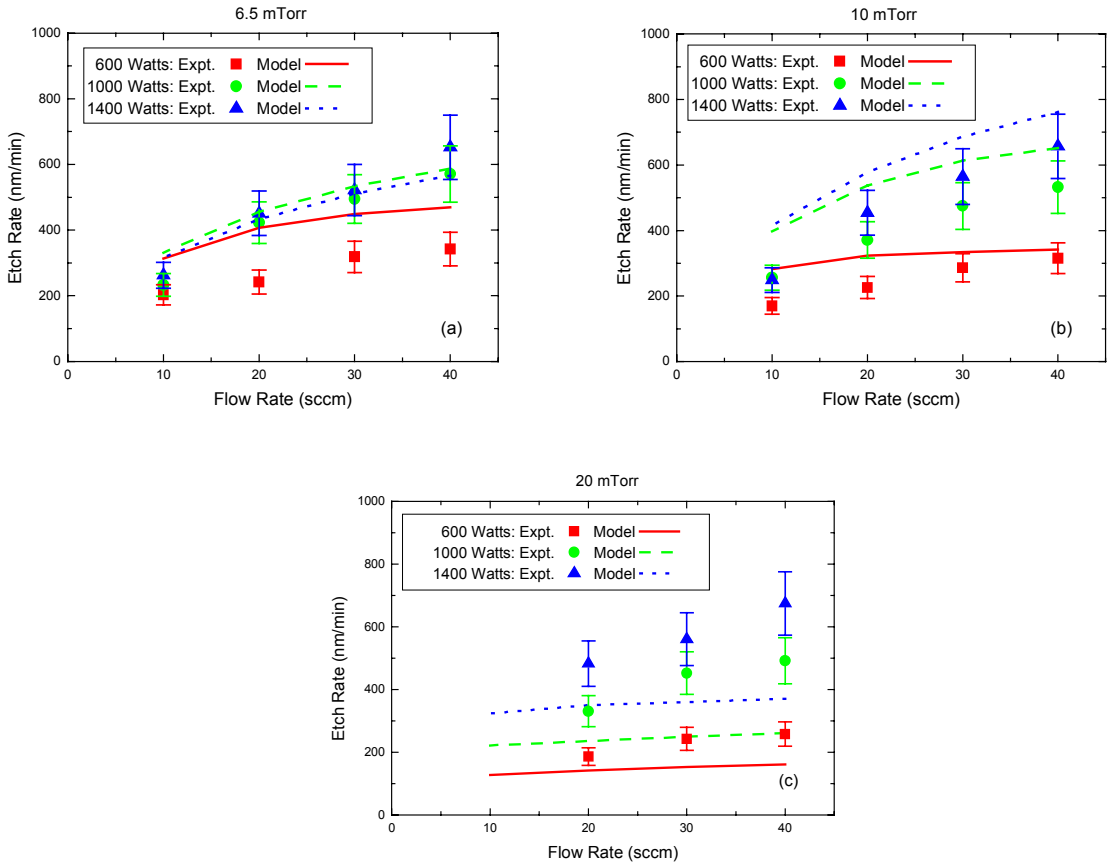

Figure 13. Oxide etch rates for C_2F_6 as a function of flow rate for three different powers and pressures in Reactor II.

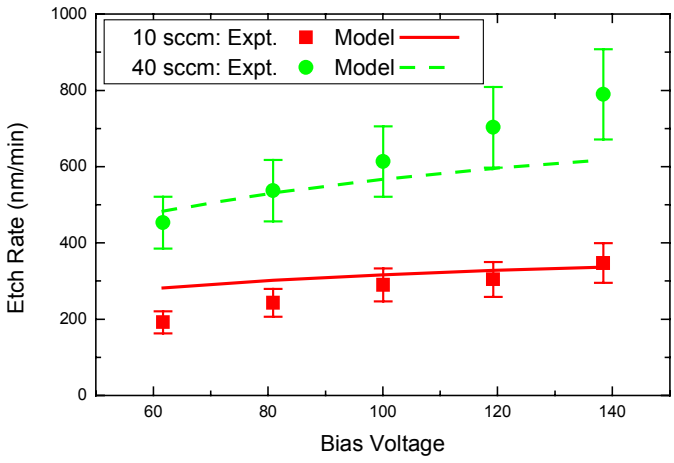

Figure 14. Oxide etch rates for C_2F_6 as a function of bias power for two different flow rates in Reactor II.

Taken as a whole, the agreement between model predictions and the experimental etch rate data for these three reactors is quite satisfactory. These comparisons also clearly illustrate the complexity of this chemical system, where simple rules about trends do not apply, especially across different plasma reactors. Even within one plasma system, the direction of the etch rate dependence on a parameter such as power or pressure can vary depending on the value of other operating parameters.

4.2.2. Electron and Ion Densities

The diagnostic data shown here for Reactor IA were measured at Sandia with a silicon wafer in the reactor as well as a quartz confining ring and a large quartz window, which are etched by the plasma. The default, or base, conditions are 200 W, 10 mTorr, 10 sccm, and 20 W bias power, so if a parameter is not specified in a figure, these values should be used. The plasma powers were reduced by 0.8 in the model to account for the efficiency of coupling into the plasma. Error bars shown in these graphs indicate estimated experimental uncertainties.

Figure 15 shows experimentally measured electron densities [11] as a function of (a) plasma power, (b) pressure, and (c) bias power, in Reactor IA for C_2F_6 plasmas, along with the corresponding simulations. The electron densities were measured by Hebner and Miller [11] using microwave interferometry. The model reproduces both the absolute magnitude of the electron densities and the general trends quite well, as well as the relative densities between gases (discussed in more detail below).

However, some noticeable differences remain. Figure 15(a) shows that the model predicts a leveling-off in the electron density at higher powers while the experimental values continue to rise. Unfortunately, attempted changes in the mechanism to increase the electron density at high powers led to larger disagreements with other data sets, so the decision was made to accept this discrepancy at this time. For the pressure dependence shown in Figure 15(b), the model fits the experimental data quite well, except at the lowest pressures. The C_2F_6 model has a distinct peak at ~10 mTorr, while the experiments show a steady decline. The bias dependence shown in Figure 15(c) shows a disagreement between model and experiment. The experiments show a rise in electron density at bias powers above ~75 W, whereas the model predicts almost no change. These observations suggest that the bias power may be acting in a non-ideal manner and adding to the plasma power in addition to accelerating the ions, but the model currently only treats the latter. Although not included in the Tables or Figures, the model also reproduces the reported [11] overall magnitudes and trends in electron temperature with power and pressure.

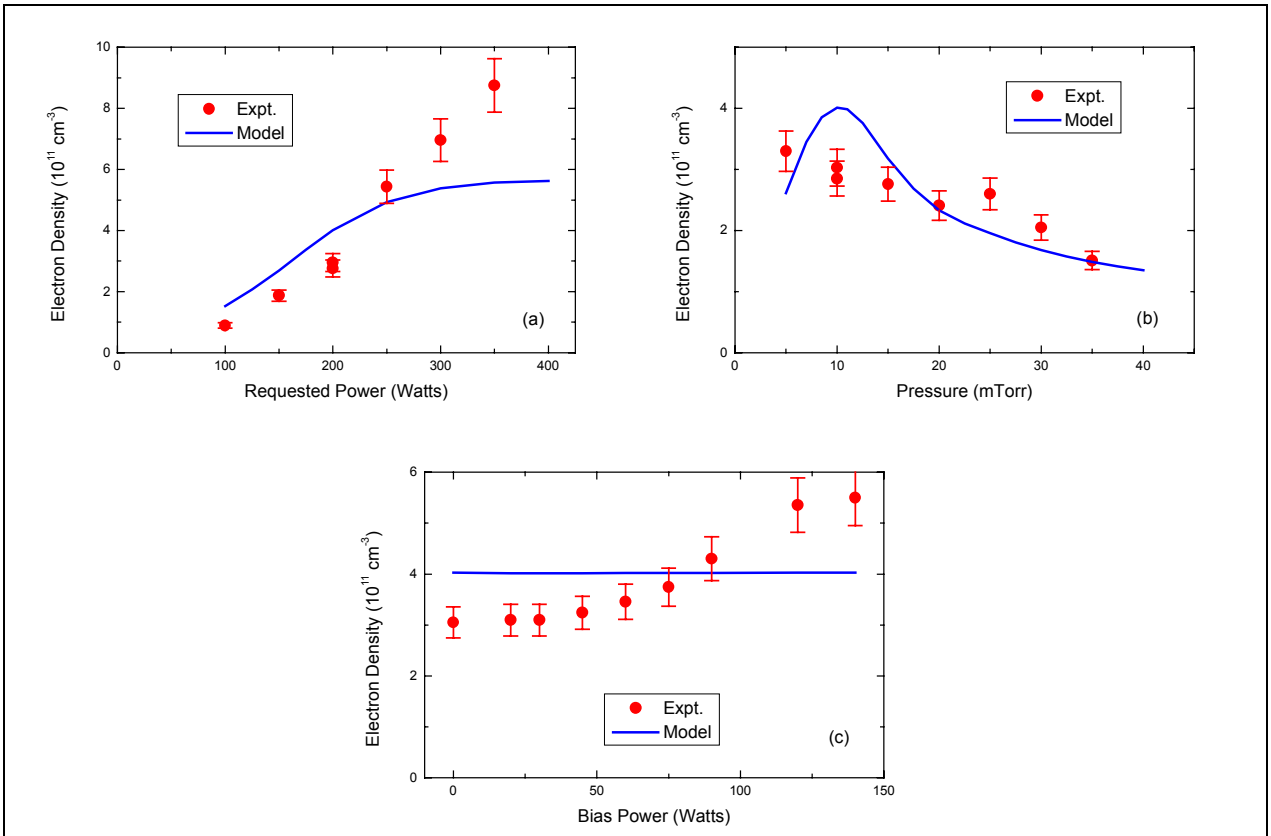

Figure 15. Electron density comparisons between model and experiment for C_2F_6 plasmas in Reactor IA. Dependence on: (a) plasma power, (b) pressure, and (c) bias power.

Figure 16 shows similar plots of experimentally measured F^- densities [11] as a function of (a) plasma power, (b) pressure for C_2F_6 plasmas, and (c) bias power, along with the corresponding simulations. The negative ion densities were measured using laser photodetachment. The error bars in these plots indicate the estimated experimental within-run uncertainties, but the uncertainty in absolute number density is notably larger, on the order of a factor of 2. In general, the agreement between model and experiment for F^- is very good, comparable to that for electron densities. Experimentally, F^- is observed at significantly lower concentration than the electrons, which is also seen in the simulations. The models also reproduce the presence of a maximum in the power-dependence and pressure dependence curves. However, the model predicts a too-weak power dependence, and the peak of the curve is located at lower powers. As a function of bias power, the experimental negative ion density drops above ~75 W bias power whereas the model predicts no variation. Both the decrease in F^- density and the increase in electron density at higher bias power are consistent with the idea, mentioned above, that the bias power is beginning to contribute to the deposited plasma power, which is an effect that is not included in the model. Note that for C_2F_6, the primary route for production of F^- in this mechanism is the dissociative attachment of C_2F_6 itself.

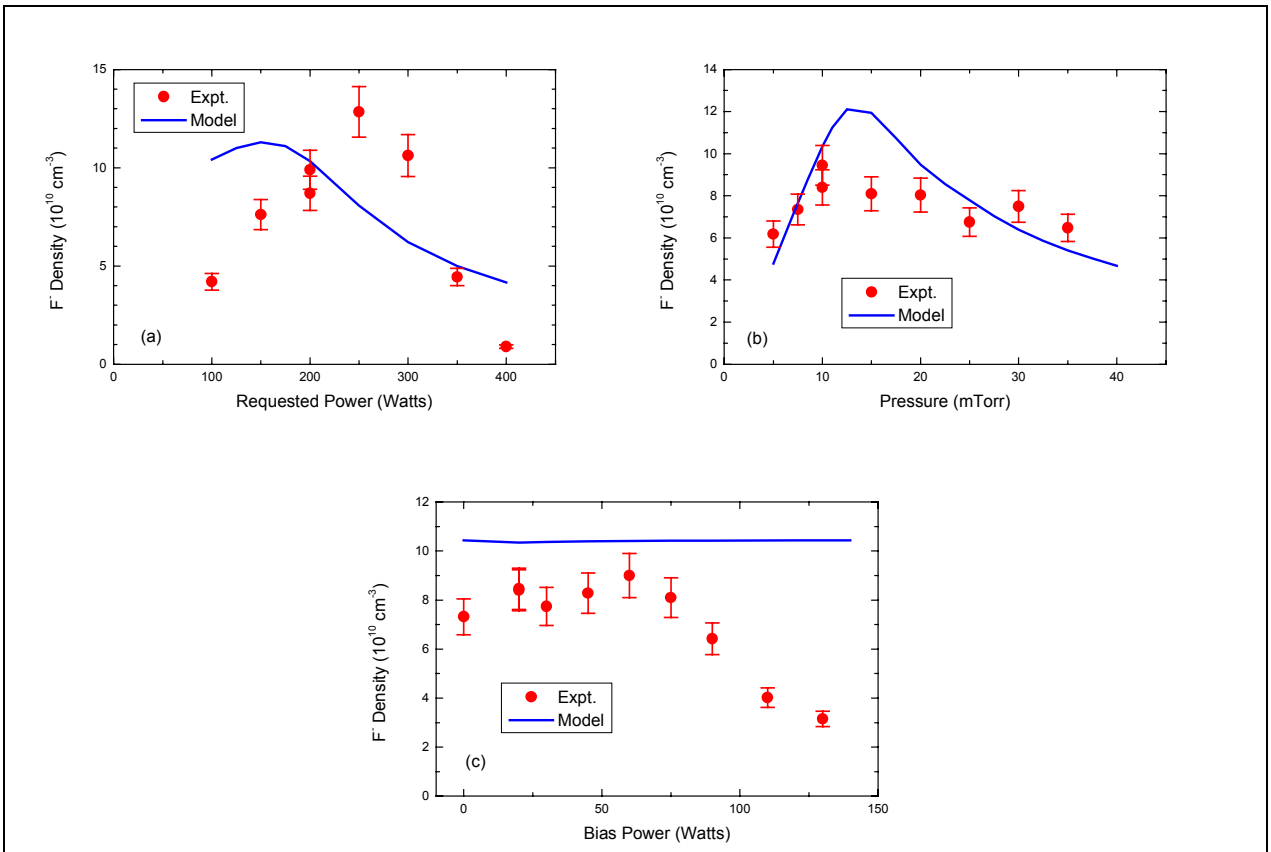

Figure 16. Negative ion density comparisons between model and experiment for C_2F_6 in Reactor IA. Dependence on: (a) plasma power, (b) pressure, and (c) bias power.

In Reactor II, experimental measurements of ion current densities (ICD) were also available for comparison with the simulations. These comparisons exhibit many of the same features as the etch rate comparisons in this reactor, with a few notable differences. Figure 17 shows ICDs as a function of power for a variety of pressures and flow rates, which can be compared with the etch rates shown in Figure 11. Figure 18 shows the pressure dependence at 30 sccm, to be compared with the etch data in Figure 12. Figure 19 shows the ICDs as a function of flow rate for various powers and pressures, to be compared with the etch data in Figure 13. In contrast with the analogous plots for the etch rates, the ICDs are generally invariant with flow rate. In the early simulations, the ICDs were initially quite high at low flow rate. Adjusting the mechanism to yield fairly flat ICDs as a function of flow rate turned out to be an important part of getting the correct etch rate dependencies.

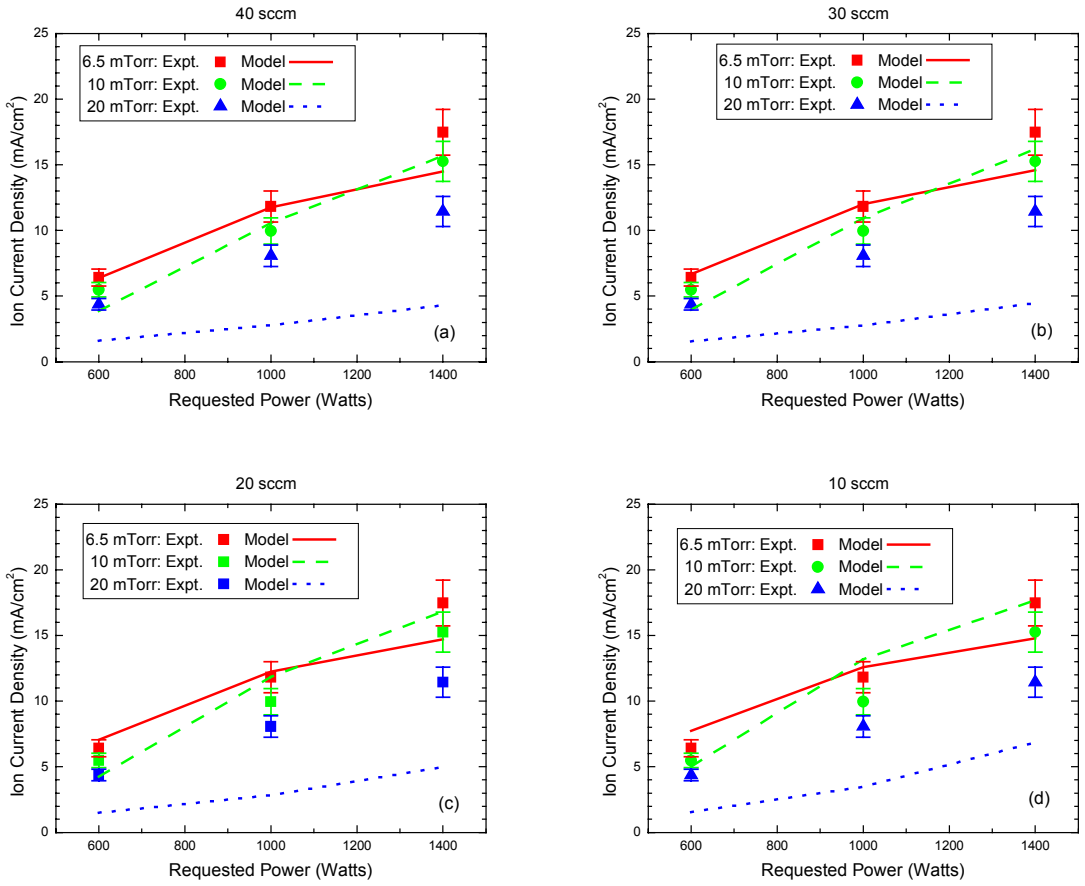

Figure 17. Ion current densities for C_2F_6 as a function of plasma power for three different pressures at four different flow rates in Reactor II.

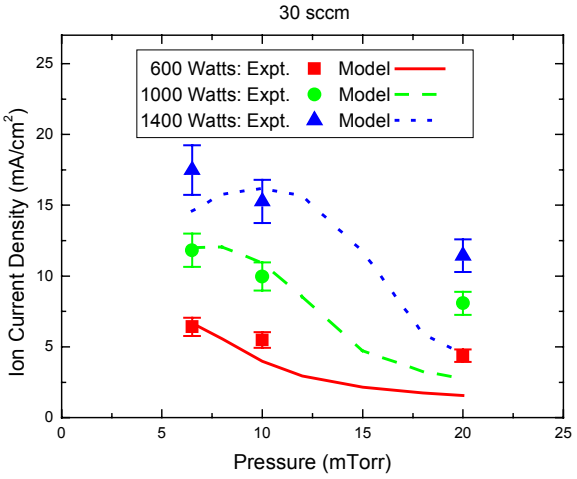

Figure 18. Ion current densities for C_2F_6 as a function of pressure for three powers in Reactor II.

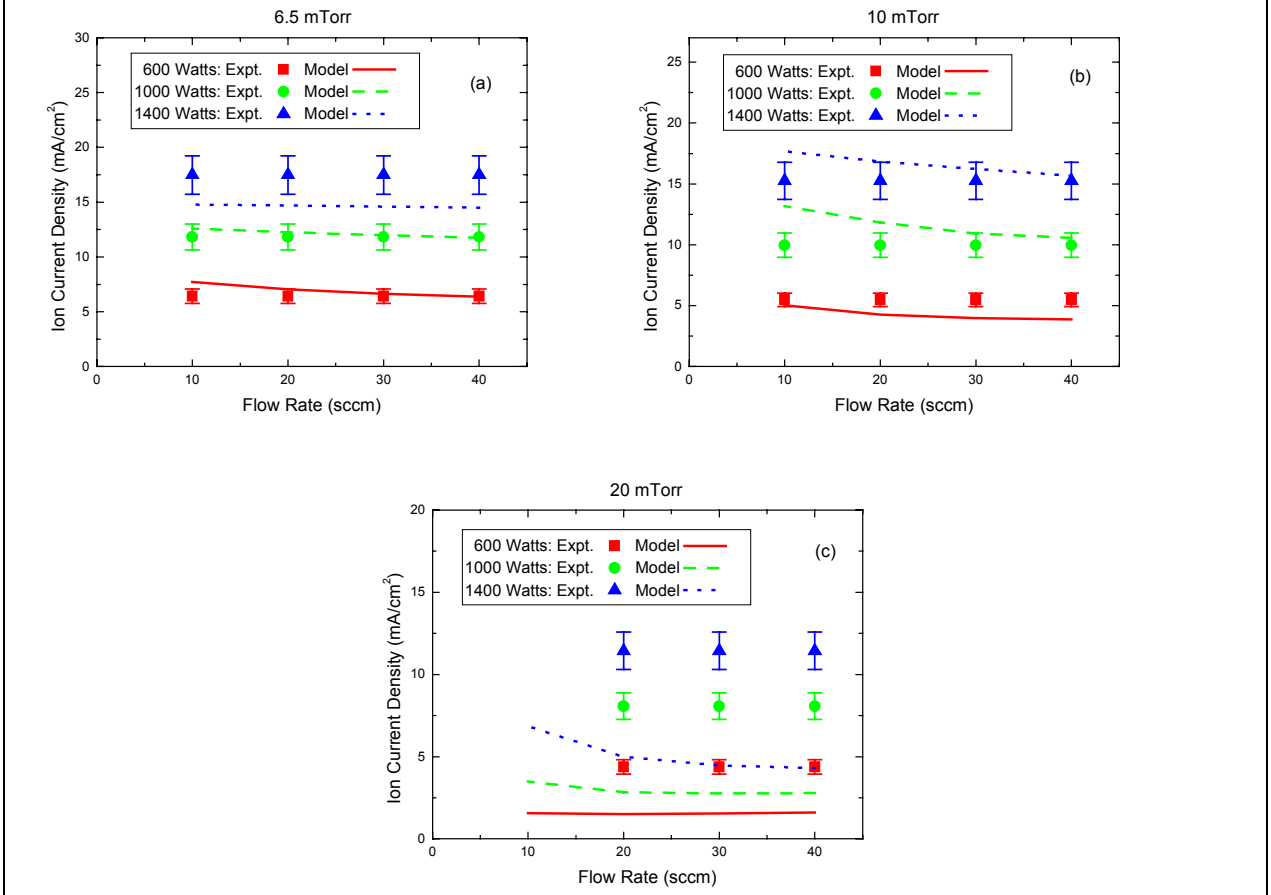

Figure 19. Ion current densities for C_2F_6 as a function of flow rate for three different powers and pressures in Reactor II.

Table 8 gives the distribution of the various gas and surface species (denoted by (S)) for C_2F_6 in Reactor IA from the model at the nominal conditions of 200 W plasma power, 10 mTorr, and 20 W bias, with a silicon wafer. The ion densities are generally consistent with mass spectrometric studies by Jayaraman, et al., [50] although the agreement is not perfect. Their experiments indicate that CF_3^+ is present at 4-5 times higher concentration than CF_2^+ and CF^+, whereas the simulations show roughly comparable concentrations for CF_3^+ and CF_2^+ , with CF^+ being roughly a factor of two lower. However, model and experiment agree that SiF_x^+ ions are generally lower in concentration than CF_x^+ ions. The model predictions of low concentrations of F^+ , O_2^+ and Si^+ are consistent with the fact that they were not observed in the experimental studies. The experiments reported relatively higher concentrations of CO^+ than the model indicates, but do not include O^+. In contrast, $C_2F_4^+$ and $C_2F_5^+$ were reported in the experiments, but are not included in the model.

Table 8. Distribution of gas-phase and surface species for a C_2F_6 plasma in Reactor IA. Silicon wafer, oxide walls.

Species	Mole Fraction	Species	Mole Fraction	Species	Mole Fraction
e^-	0.2311E−2	C_2F_6	0.03492	SiF_4	0.1052
F^-	0.5951E−3	CF_4	0.04020	SiF_3	0.04408
CF_3^+	0.7354E−3	CF_3	0.1260	SiF_2	0.02807
CF_2^+	0.6877E−3	CF_2	0.1633	SiF	0.00410
CF^+	0.4257E−3	CF	0.1159	Si	0.00888
SiF_3^+	0.3308E−3	C	0.08328	Si(S)	0.7138
SiF_2^+	0.3028E−3	F	0.1399	Si_F_2(S)	0.2862
SiF^+	0.2490E−3	CO	0.04978	SiO_2(S)	0.02383
Si^+	0.1450E−4	O_2	0.00134	SiO_2_F_2(S)	0.03961
F^+	0.2546E−4	O	0.04935	SiO_2_CF_2(S)	0.9366
O_2^+	0.5333E−5				
O^+	0.1018E−3				
CO^+	0.2770E−4				

4.2.3. Neutral Species Densities

Mass spectrometric measurements have difficulty providing data for reactive intermediate species because of interference via fragmentation of larger species in the ionizer. Laser diagnostic techniques can provide unambiguous identification and measurement of small radical species, but generally only give relative trends, rather than absolute number densities. The neutral intermediate species CF, CF_2, SiF and SiF_2 have been studied using laser-induced fluorescence (LIF) techniques in C_2F_6 plasmas by Hebner in Reactor IA [12,13,14]. The CF_x species are formed by dissociation of the input C_2F_6, while SiF_x species are etch products. Model/experiment comparisons for these species thus test different parts of the model.

LIF provides relative number densities only, so comparing the experimental values with model predictions involves a calibration factor. Generally, a single calibration was done for all the data in a given molecule and plasma system in such a way that experiment and model agreed at the base conditions of 200 W plasma power, 10 mTorr and 20 W bias power. For CF_2, the experimental data were taken in such a way that the values can be compared across the various gases, so densities could be compared across C_2F_6, CHF_3 and C_4F_8. For SiF_2, the densities can be compared across C_2F_6 and C_4F_8.

Figure 20 shows comparisons between model and experiment [12]for CF_2 as a function of power and pressure for both C_2F_6 plasmas. The LIF values have been scaled to overlap the model at the nominal conditions. Error bars indicate estimated experimental uncertainties of 20%, although generally within-run reproducibility is better than between-run reproducibility in these kinds of experiments. In this case, experiment and model agree that the CF_2 density: 1) decreases with increasing power, 2) increases with increasing pressure, and 3) does not vary with bias power. However, the magnitudes of the power and pressure dependencies are too large.

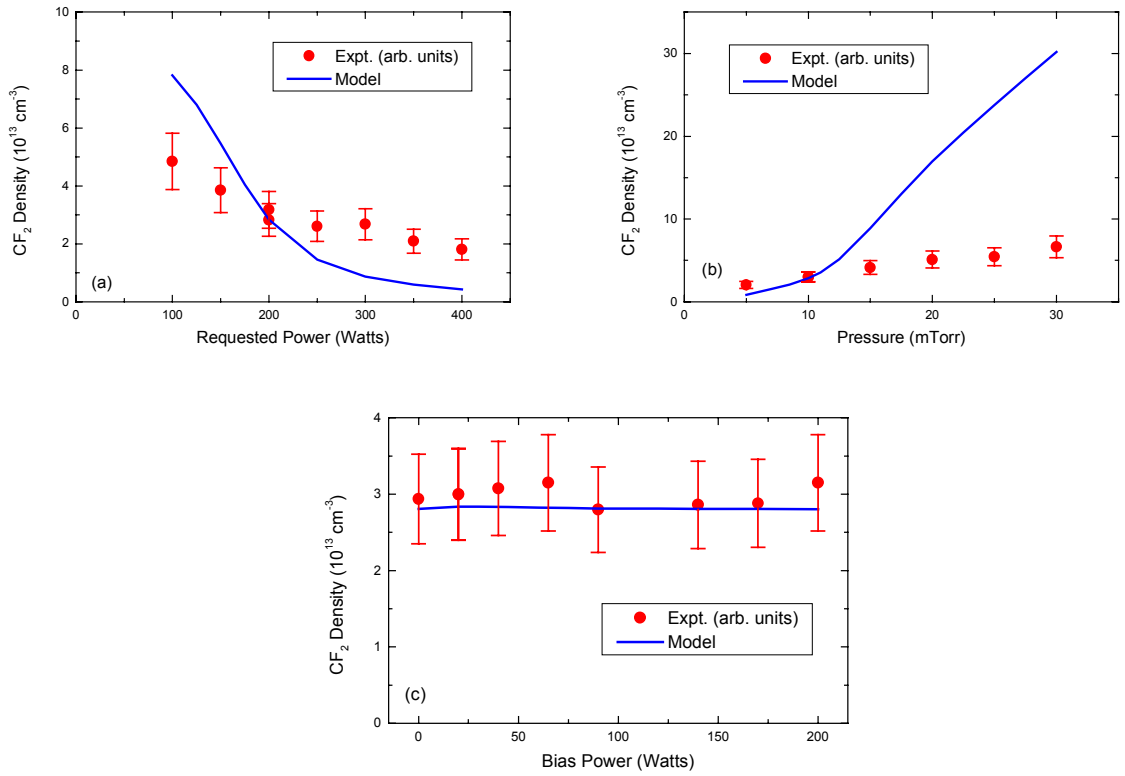

Figure 20. CF_2 density comparisons between model and experiment (arbitrary units) for C_2F_6 in Reactor IA. Dependence on: (a) plasma power, (b) pressure, and (c) bias power.

Figure 21 shows analogous plots for CF. In this case, experiment [12] and model agree that in C_2F_6 plasmas, the CF density: 1) decreases with increasing power, 2) increases with increasing pressure, and 3) does not change much with bias power. This is qualitatively similar to the CF_2 results. The model predictions for the power dependence are a little low at the low end of the power dependence leading to a "humped" curve, and somewhat too flat at the high end of the pressure dependence, but generally agree quite well with experiment.

As shown in Table 8, the current version of the mechanism predicts that CF is present in comparable concentrations to CF_2 and CF_3. This contrasts with the results from line-integrated diode laser absorption measurements by Abraham [51] and by Anderson and coworkers [52] which showed that CF was lower than the others by about an order of magnitude. However, spatially-resolved LIF studies [12] in Reactor IA indicate that CF and CF_2 have very different spatial distributions, with CF predominantly in the center of the plasma and CF_2 showing significant densities in the regions away from the electrodes. This greatly complicates the interpretation of the line-integrated absorption measurements. There are also qualitative disagreements between absorption and LIF measurements in terms of the direction of the dependence on power, which are convoluted with gas temperature profiles. In view of these complications, we have decided that it is more appropriate at present to compare the results of our zero dimensional simulations with the LIF measurements in the center of the discharge rather

than the line-integrated absorption measurements, which would be better compared with two-dimensional simulations.

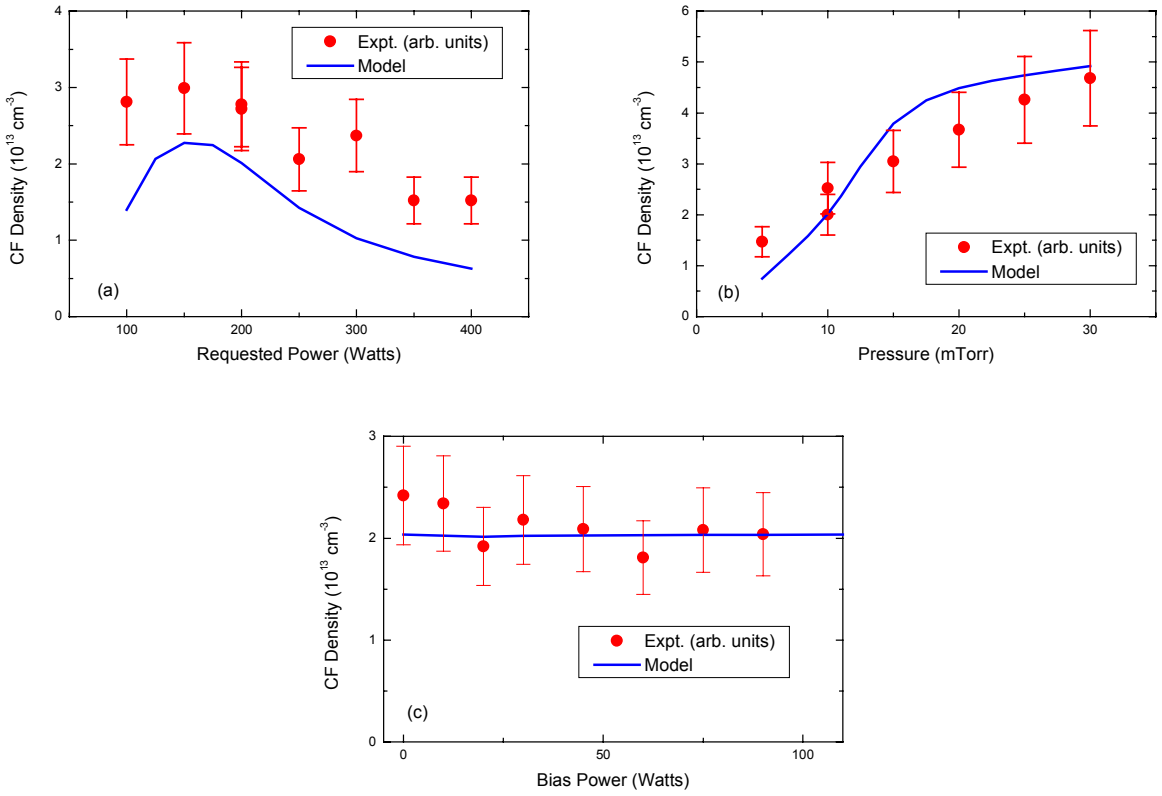

Figure 21. CF density comparisons between model and experiment (arbitrary units) for C_2F_6 in Reactor IA. Dependence on: (a) plasma power, (b) pressure, and (c) bias power.

The LIF experiments on CF [12] also provide information on the rotational temperatures of the molecule from the relative intensities of the spectral lines. If we assume that the CF temperature is representative of the neutrals in the plasma, these values can be compared with the gas temperatures in the simulations. As shown in Figure 22, the experimental uncertainties are quite large (~50K), but the simulations give the same general trends of increasing temperature with increasing plasma power, and a relatively flat dependence on pressure. However, the experiments show a negative dependence on bias power that is not reproduced by the model. The experimental temperatures, especially at high powers, were used to guide the choice of boundary conditions (surface temperatures) in the simulations, but the large experimental uncertainties discourage one from spending much effort improving the agreement on this.

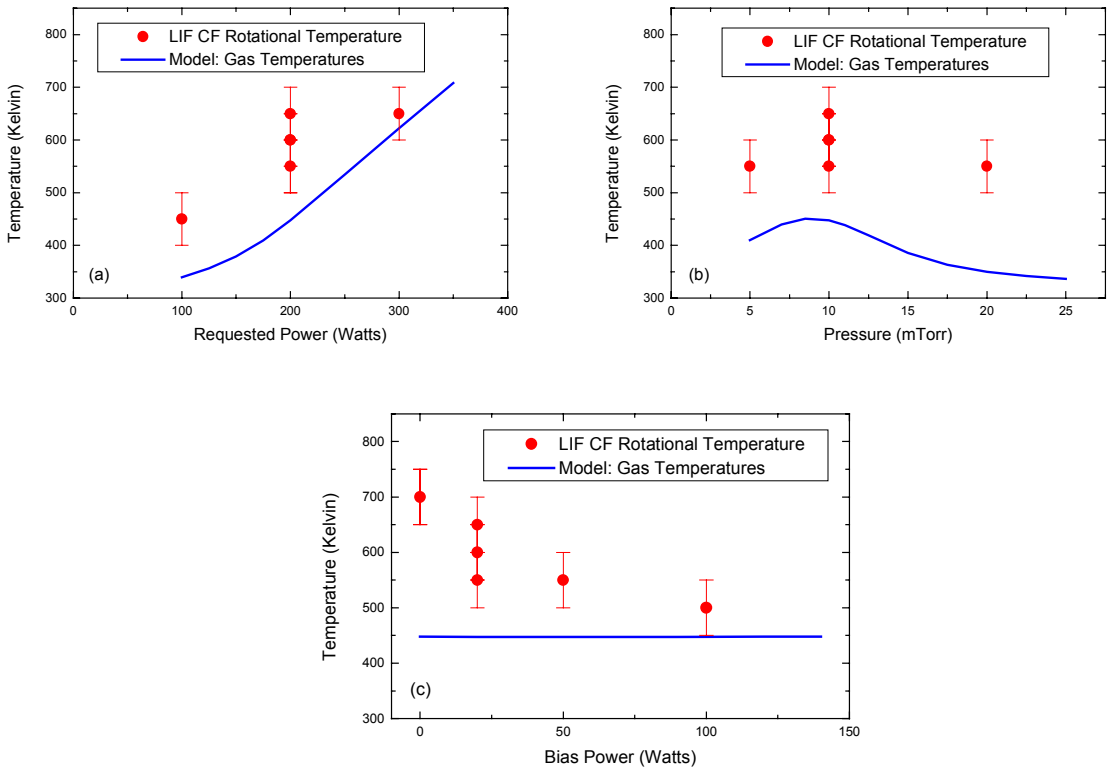

Figure 22. Gas temperatures from CF LIF experiments for C_2F_6 in Reactor IA. Dependence on: (a) plasma power, (b) pressure, and (c) bias power.

Figure 23 shows comparisons between model and experiment [12] for SiF as a function of (a) plasma power, (b) pressure, (c) bias power and (d) gas mixture for C_2F_6 plasmas. The SiF data represent a case where no effort has been made to adjust rate parameters in the model to improve agreement with the experimental data. Thus they provide examples of "poor" and "okay" agreement between model and experiment. In this case, the simulations show decreases in SiF density at high power and high pressures that are either not seen in the measurements, or are much milder. The model does, however, successfully reproduce the flat dependence on bias power and the dependence on C_2F_6/O_2 ratio. Although the latter probably results mostly from the changing F content of the system, no gas-mixture experiments were used to develop the reaction mechanism, so this agreement is gratifying.

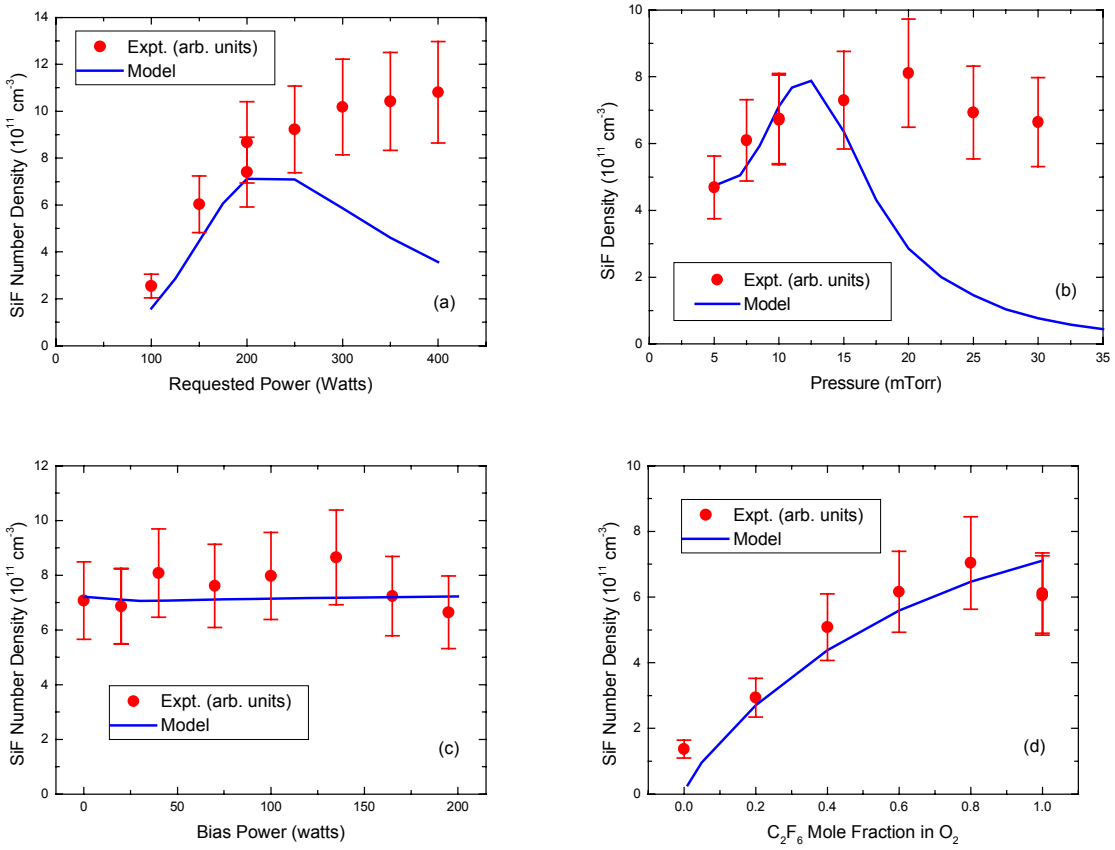

Figure 23. SiF density comparisons between model and experiment (arbitrary units) for C_2F_6 in Reactor IA. Dependence on: (a) plasma power, (b) pressure, (c) bias power, and (d) gas mixture with O_2.

Figure 24 shows comparisons between simulation and experiment [14] for the SiF_2 species. SiF and SiF_2 are both produced by electron-impact dissociation of SiF_4 etch products, so the similarities between them are not surprising. In both cases, no effort was made to adjust rate parameters in the model to improve agreement with the experimental data. As for SiF, the simulations show decreases in SiF_2 density at higher powers and pressures that are either not seen in the experiments, or are much milder.

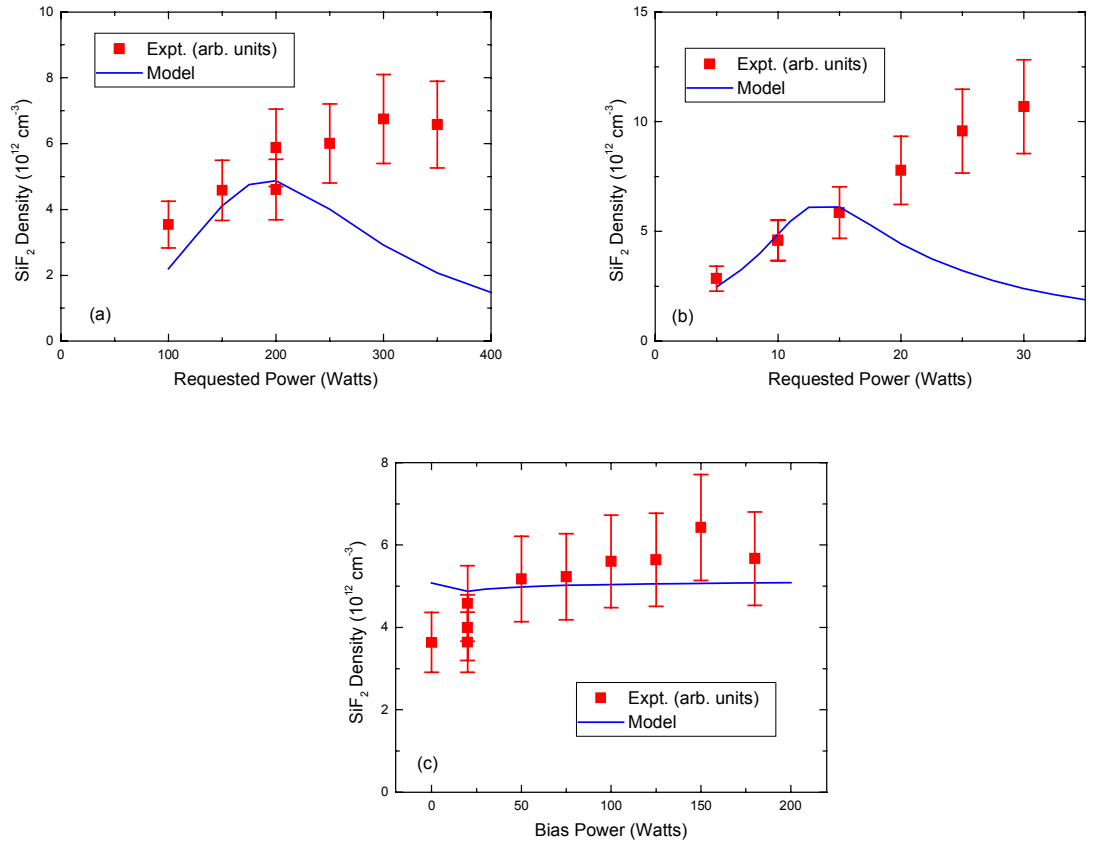

Figure 24. SiF_2 density comparisons between model and experiment (arbitrary units) for C_2F_6 in Reactor IA. Dependence on: (a) plasma power, (b) pressure, and (c) bias power.

4.3. Dominant Reaction Paths

One of the reasons to construct detailed reaction mechanisms for modeling plasmas is that the relative importance of various reaction paths can be evaluated from the simulations. An examination of the dominant reaction paths was done for a C_2F_6 plasma at the "base conditions" in Reactor IA, that were used for many of the diagnostic experiments described above. For purposes of these analyses, we generally define a dominant reaction path as one contributing ≥ 10% of the etch rate or a major species density.

As shown by the distribution of gas-phase species in Table 8, most of the C_2F_6 injected into the reactor is dissociated by the plasma to smaller fragments. Figure 25 shows that this occurs primarily, in order of decreasing importance, by electron impact dissociation forming 2 CF_3 radicals, dissociative attachment forming $F^- + CF_2 + CF_3$, and dissociative ionization forming $CF_3^+ + CF_3$ (reactions 6, 10, and 7 in Table 2, respectively). These fragment species then undergo further ionization, dissociation, dissociative ionization, or dissociative neutralization reactions. CF_4 is formed both by associative attachment of F^- and by surface reactions as an oxide etch product; only the former appears in this diagram. CO is also formed by surface

reactions as an oxide etch product, and is then dissociated by the plasma. The positive ions are generally neutralized at surfaces, but these neutralization reactions are not shown in this figure. In this case, almost all the dominant gas-phase reactions are electron impact reactions (solid lines), with only two associative detachment reactions (dashed lines).

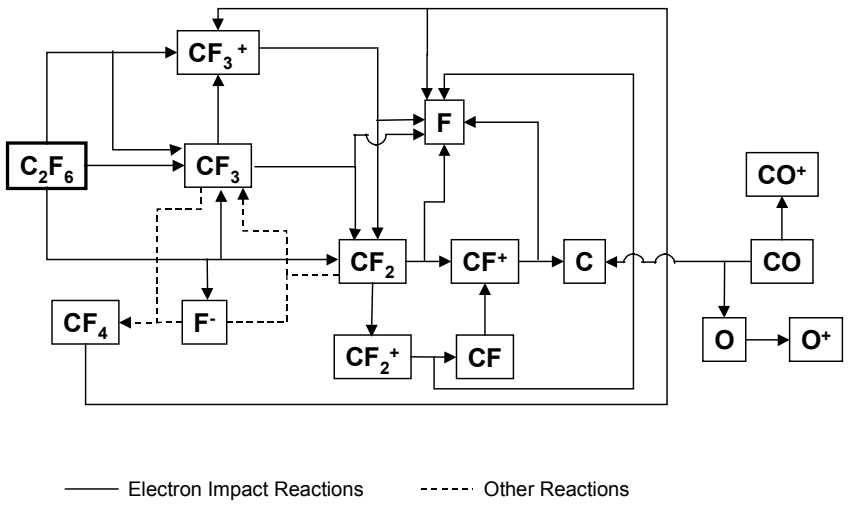

Figure 25. Primary gas-phase reaction paths of carbon-containing species for a C_2F_6 plasma in Reactor IA. Silicon wafer, oxide walls.

Figure 26 shows dominant gas-phase reactions for silicon-containing species. In this case, all the dominant gas-phase reactions are electron impact reactions, so the solid lines indicate reactions involving positive ions, and the dashed lines indicate reactions involving neutrals only. For this set of reactions, SiF_4 is the starting point and is formed by surface reactions as both a silicon etch product and an oxide etch product. It is less completely dissociated by electron impact than C_2F_6, and primarily forms, in order of decreasing importance, $SiF_3 + F$, $SiF_3^+ + F$, and $SiF_2 + 2F$ (reactions 49, 52, and 50 in Table 2, respectively). These fragment species then undergo further ionization, dissociative ionization, or dissociative neutralization reactions.

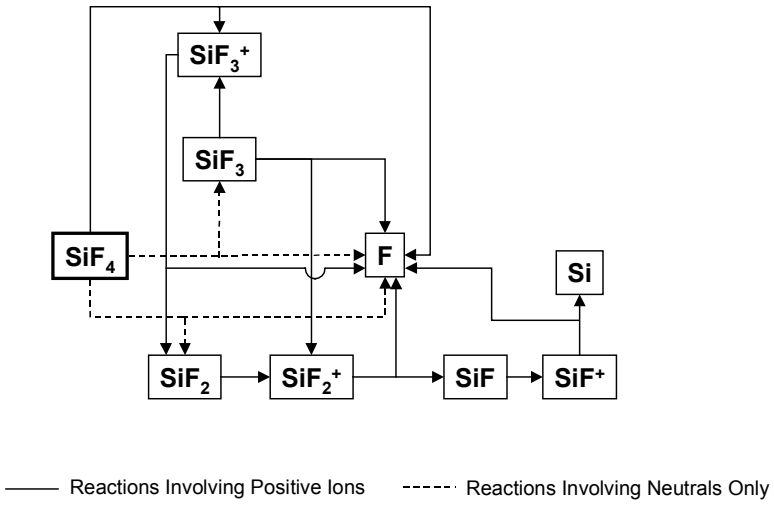

Figure 26. Primary gas-phase reaction paths of silicon-containing species for a C_2F_6 plasma in Reactor IA. Silicon wafer, oxide walls.

One of the interesting features of the reaction-path diagrams is the multitude of paths leading to F atoms. This is one of the species that needs to adsorb on the surface for etching to occur, but doesn't have a single primary source. In particular, the dissociation of the CF_x and SiF_x etch products by the plasma provides a way of recycling the fluorine to make it available for further etching. Another interesting feature is the observation that neutral radicals seem to preferentially dissociate via multistep pathways involving the ion rather than direct dissociation to smaller neutral species. In other words, AF_x (A=C, Si; x=1-3) species undergo $AF_x \rightarrow AF_x^+ \rightarrow AF_{x-1}$ reactions rather than $AF_x \rightarrow AF_{x-1}$, except for the case of CF_3.

Figure 27 shows the dominant surface reactions on the silicon wafer, which are relatively simple. Silicon sites on the surface are fluorinated primarily by reaction with F atoms, with a small contribution from SiF_x^+ ions that deposit on the surface. Some ion-assisted etching of the silicon occurs, primarily via CF_x^+ ions, but spontaneous etching is unimportant. As shown in Table 8, the silicon surface has more open sites than fluorinated sites. Thus most of the ions incident on the wafer simply neutralize.

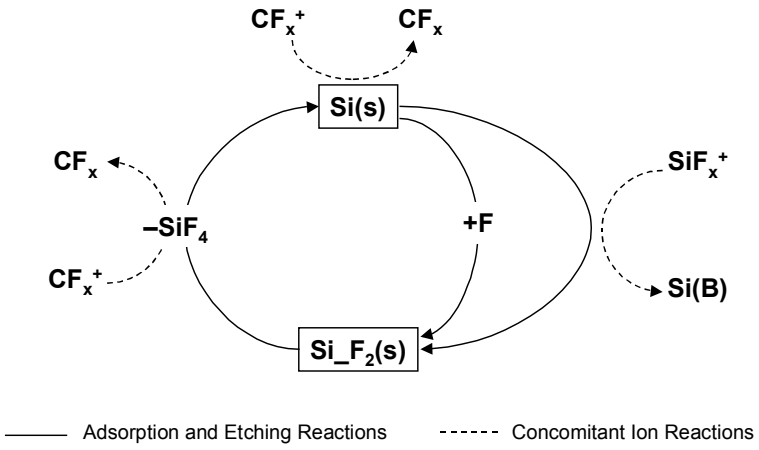

Figure 27. Primary reaction paths on the silicon wafer surface for a C_2F_6 plasma, Reactor IA.

In contrast, the dominant surface reactions shown in Figure 28 for the oxide walls are quite complex. This partially results from the presence of fluorocarbon sites on the surface, leading to many more potential reactions. It also partially results from the fact that neutral reactions can compete with the ion-assisted reactions on the walls because of the lower ion energies. Open sites on the oxide surface, SiO_2(s) are converted to fluorine-covered sites, $SiO_2\_F_2$(s), or fluorocarbon-covered sites, $SiO_2\_CF_2$(s), by reaction with F atoms or CF_x radicals from the gas, respectively. The oxide surface is mostly covered with fluorocarbons at steady state (see Table 8), which means that neutralization of ions on open sites is much less important on this surface. $SiO_2\_CF_2$(s) is primarily consumed by ion-assisted etching reactions, although abstraction of F from the surface by gas-phase SiF_x radicals and reaction of gas-phase F atoms with the surface CF_x groups also play a role. $SiO_2\_F_2$(s) is consumed by reaction with CF from the gas to form $SiO_2\_CF_2$(s), ion-assisted etching, and F abstraction by C atoms and SiF_x radicals.

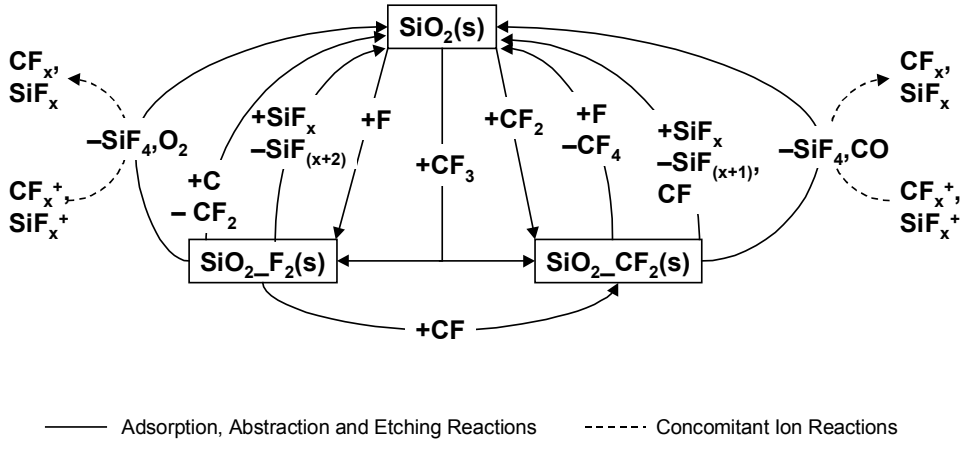

Figure 28. Primary reaction paths on the oxide wall surface for a C_2F_6 plasma, Reactor IA.

One of the reasons for doing the reaction-path analysis for Reactor IA is that many diagnostic experiments were done using the nominal conditions. Identifying the dominant pathways can assist in interpreting the experiments as well as in developing the mechanism. In addition, pathway analysis is useful in understanding differences between reactors. To this end, a similar analysis is done for the case of an oxide wafer being etched in Reactor III, (the commercial oxide etching tool). Here, we are primarily interested in the differences between the reactors.

Figure 29 shows the primary gas-phase reaction for carbon-containing species in Reactor III (10 mTorr, 20 sccm and 1550 W), while Figure 30 shows the reactions for silicon-containing species. Comparing these figures with Figure 25 and Figure 26, respectively, shows that the dominant reactions in the two reactors are generally quite similar. The major differences are the increased importance of a number of reactions in Reactor III that lead to more extensive dissociation of the gas. For example, in Reactor IA, CF_3 decomposes primarily to CF_3^+ and to CF_2 and F. In Reactor III, dissociative ionization of CF_3 to CF_2^+ and F, as well as to CF^+ and F, also become significant. Likewise, SiF_2 dissociative ionization to SiF^+ + F, SiF decomposition to Si^+ + F, and F atom ionization to F^+ become important in Reactor III. A contrasting difference is that the associative detachment reaction of F^- with CF_x radicals, which is important in Reactor IA, becomes less significant in Reactor III, where F^- reaction with F atoms dominates.

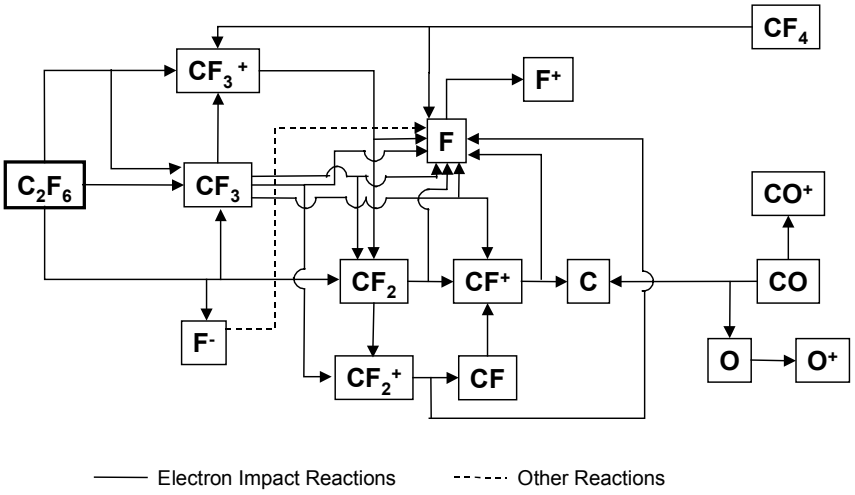

Figure 29. Primary gas-phase reaction paths of carbon-containing species for a C_2F_6 plasma in Reactor III.

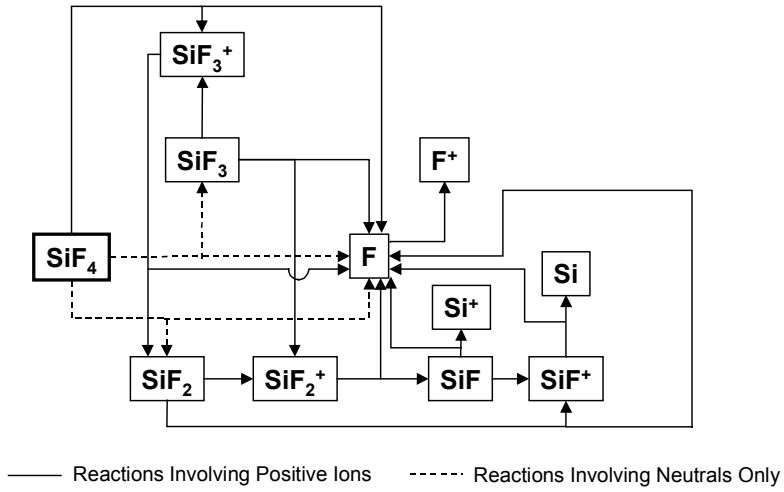

Figure 30. Primary gas-phase reaction paths of silicon-containing species for a C_2F_6 plasma in Reactor III.

The major difference of interest between the two reactors is the wafer material. Figure 31 shows the dominant reaction paths on the oxide wafer in Reactor III. Many of these reactions are the same as shown in Figure 28 for the oxide walls in Reactor IA, but the picture is simpler overall. The incident ions have higher energies because of the bias applied to the wafer and correspondingly higher etching efficiencies. Under these conditions, abstraction of F atoms from the surface by radicals from the gas cannot compete, and thus do not appear in the diagram. For these conditions, the wafer surface is ~80% covered by open sites at steady state, such that surface fluorination by SiF_x ions becomes significant. This large a fraction of open sites is also consistent with the observation that the etch rate in Reactor III is relatively more sensitive to C_2F_6 supply rate, and less sensitive to bias power than the etch rates in the other reactors. This reactor is being operated in a regime where the etch rate is limited by the rate of adsorption of fluorine-containing etchants, rather than being limited by the rate of ion-assisted desorption.

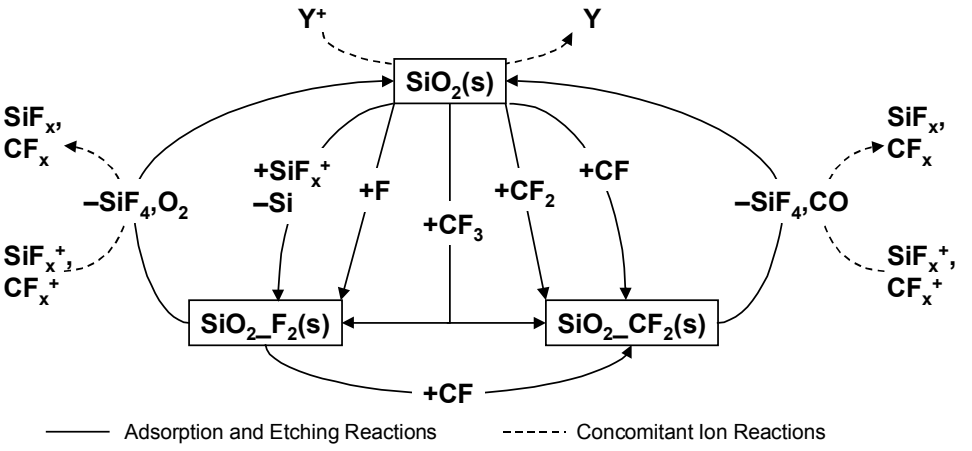

Figure 31. Primary reaction paths on the oxide wafer surface for a C_2F_6 plasma, Reactor III.

5. CHF_3 Etch of Silicon Dioxide

The reaction mechanism for the trifluoromethane plasma etch of silicon dioxide was the second most completely studied system. Although not quite as much experimental data are available for validation, it still is a substantial body of data. The primary chemical difference is the presence of hydrogen-containing species. Again, we do not include all species comprised of C, H and F, but just the most likely ones, based on the dissociation of the starting CHF_3 species.

5.1. Reaction Mechanism

The additional reactions in the mechanism for this system are given at the end of this subsection. They are in three Tables, one for each of the CHEMKIN and Surface-CHEMKIN input files. To construct the gas phase reaction mechanism for CHF_3 plasma etching, the 38 reactions in Table 9 were added to the 122 reactions in Table 2 that do not involve the C_2F_6 itself. For electron-impact reactions of CHF_3, the rate parameters are primarily based on a cross section set recently published by Kushner and Zhang [53]. In some cases, particularly the dissociative attachment reactions, separate, but identical reactions are used to describe features in different energy ranges in the cross-section set. There are also a few estimated rate parameters. Electron impact reactions for H and H_2 were taken from Janev, et al. [54] The remaining ion-ion reactions or dissociative recombination reactions have estimated rate parameters.

For silicon surfaces in CHF_3 plasmas, the 28 reactions in Table 10 were added to the 30 reactions in Table 3 comprising the C_2F_6 silicon surface mechanism. The first two reactions in Table 10 represent the surface recombination of H atoms to form H_2, written as the adsorption of H atoms on open Si(S) sites followed by reaction of a gas-phase H atom with an adsorbed H atom. Such reactions are expected to be quite efficient and are given relatively high sticking coefficients. Reactions 3-5 are the abstraction of H atoms from the surface by F atoms, CF_2 and CF radicals, respectively. These reactions provide a way to remove H atoms from the surface, and the rate constants are set to reasonable values that give good fits to the experimental data. Reactions 6-9 in Table 10 are ion-assisted etch reactions for hydrogen-containing ions. The yields were extrapolated from the mass-weighted yields given for CF_x and SiF_x ions in Table 3. Reactions 10-24 are ion-assisted desorption of hydrogen from the surface, with mass-weighted yields set to values 5 times lower than those used for the etching reactions, that gave good fits to the experimental data. The remaining 4 reactions are neutralization of H-containing ions on open sites.

For CHF_3 plasma etching of oxide surfaces, the 34 reactions in Table 11 were added to the 55 reactions in Table 4 for the C_2F_6 oxide system. The first set of reactions are again adsorption and abstraction reactions with estimated/fit rate parameters. For the oxide surface, however, a set of ion-assisted etch reactions (reactions 8-20) involving the hydrogenated surface species SiO_2_H(S) was added to the mechanism with mass-weighted yields set to values used for the etching reactions. This was done to include the possibility that etching occurs via these species, although it turns out to be a minor reaction pathway. The remaining reactions in the table are ion-assisted etch, ion deposition, and neutralization of the hydrogen-containing ions.

Table 9. Additional gas-phase reactions for CHF_3 plasma etching of silicon dioxide. [a]

No.	Reaction	A	B	C	ε	Notes	Reference
	electron-impact reactions						
1.	$e^- + CHF_3 \rightarrow CHF_3 + e^-$	1.089E–2	–1.2214	2.645E+4	0.37	V1,4 [b]	53
2.	$e^- + CHF_3 \rightarrow CHF_3 + e^-$	3.019E–2	–1.3964	1.759E+4	0.18	V2,5 [b]	53
3.	$e^- + CHF_3 \rightarrow CHF_3 + e^-$	5.218E–2	–1.4396	1.406E+4	0.13	V3,6 [b]	53
4.	$e^- + CHF_3 \rightarrow CHF_3 + e^-$	4.122E–2	–1.379	1.549E+5	10.9	E [c]	Estimate
5.	$e^- + CHF_3 \rightarrow CHF_3 + e^-$	1.584E–11	0.4322	1.415E+5	11.9	E [c]	Estimate
6.	$e^- + CHF_3 \rightarrow CF_3^+ + H + 2e^-$	5.361E–15	1.3438	1.736E+5	15.2		53
7.	$e^- + CHF_3 \rightarrow CHF_2^+ + F + 2e^-$	2.225E–15	1.2886	1.906E+5	16.8		53
8.	$e^- + CHF_3 \rightarrow CF_2^+ + HF + 2e^-$	6.533E–17	1.4404	1.800E+5	17.6		53
9.	$e^- + CHF_3 \rightarrow CF^+ + 2F + H + 2e^-$	6.780E–16	1.5225	2.335E+5	20.9		53
10.	$e^- + CHF_3 \rightarrow F^+ + CHF_2 + 2e^-$	8.120E–14	0.9194	4.273E+5	37.0		53
11.	$e^- + CHF_3 \rightarrow CHF^+ + 2F + 2e^-$	1.006E–15	1.3223	2.120E+5	19.8		53
12.	$e^- + CHF_3 \rightarrow CF_3 + H + e^-$	3.963E–17	1.6416	1.044E+5	11.0		53
13.	$e^- + CHF_3 \rightarrow CHF_2 + F + e^-$	1.187E–16	1.3167	1.376E+5	13.0		53
14.	$e^- + CHF_3 \rightarrow CF_2 + HF + e^-$	3.626E–14	1.0759	2.631E+5	23.6		53
15.	$e^- + CHF_3 \rightarrow CHF + 2F + e^-$	8.084E–13	0.5725	4.070E+5	35.0		53
16.	$e^- + CHF_3 \rightarrow CF + H + 2F + e^-$	6.752E–9	0.1877	2.358E+5	13.3		53
17.	$e^- + CHF_3 \rightarrow CF_3 + H + e^-$	2.555E–6	–0.4365	1.546E+5	11.0		53, add-on
18.	$e^- + CHF_3 \rightarrow F^- + CHF_2$	8.988E–5	–1.3618	1.129E+5	1.3		53
19.	$e^- + CHF_3 \rightarrow F^- + CHF_2$	1.166E–6	–1.2306	4.219E+4	1.3		53
20.	$e^- + CHF_2 \rightarrow CF_2^+ + H + 2e^-$	5.361E–15	1.3438	1.736E+5	17.2		copy CHF_3
21.	$e^- + CHF_2 \rightarrow CHF^+ + F + 2e^-$	2.225E–15	1.2886	1.906E+5	14.3		copy CHF_3
22.	$e^- + CHF_2 \rightarrow CF^+ + HF + 2e^-$	6.533E–17	1.4404	1.800E+5	14.6		copy CHF_3
23.	$e^- + CHF_2 \rightarrow CF_2 + H + e^-$	3.963E–17	1.6416	1.044E+5	2.71		copy CHF_3
24.	$e^- + CHF_2 \rightarrow CHF + F + e^-$	1.187E–16	1.3167	1.376E+5	4.75		copy CHF_3
25.	$e^- + CHF_2 \rightarrow CF + H + F + e^-$	3.626E–14	1.0759	2.631E+5	8.09		copy CHF_3
26.	$e^- + H_2 \rightarrow H_2 + e^-$	1.400E–5	–0.7604	2.264E+4	0.5	V [b]	54
27.	$e^- + H_2 \rightarrow H_2 + e^-$	4.185E–12	0.6434	1.407E+5	11.37	E B_1 [c]	54
28.	$e^- + H_2 \rightarrow H_2 + e^-$	6.250E–13	0.8498	1.702E+5	11.70	E C_1 [c]	54
29.	$e^- + H_2 \rightarrow 2H + e^-$	1.697E–8	–0.0244	1.199E+5	4.4		54
30.	$e^- + H_2 \rightarrow H_2^+ + 2e^-$	1.329E–13	1.075	1.976E+5	15.4		54
31.	$e^- + H \rightarrow H + e^-$	8.367E–10	0.3014	1.335E+5	10.2	E ^2P [c]	54
32.	$e^- + H \rightarrow H^+ + 2e^-$	7.332E–12	0.6938	1.694E+5	13.6		54
	ion-ion neutralization						
33.	$F^- + CHF_2^+ \rightarrow F + CF_2 + H$	4.0E–7	–0.5	0.0			Estimate
34.	$F^- + CHF^+ \rightarrow F + CF + H$	4.0E–7	–0.5	0.0			Estimate
35.	$F^- + H_2^+ \rightarrow F + 2H$	4.0E–7	–0.5	0.0			Estimate
	dissociative recombination						
36.	$e^- + H_2^+ \rightarrow 2H$	4.0E–8	0.0	0.0	0.0		Estimate
37.	$e^- + CHF_2^+ \rightarrow H + CF_2$	4.0E–8	0.0	0.0	0.0		Estimate
38.	$e^- + CHF^+ \rightarrow H + CF$	4.0E–8	0.0	0.0	0.0		Estimate

[a] Rate coefficients of form: $k_f = A\ T^B \exp(-C/T)$. Units for A depend on the order of the reaction, but are in molecules, cm and s. B is for temperature in K. Units for C are K. ε is the electron collision energy loss in eV.
[b] V indicates a vibrational excitation. If a number is given, it denotes the number of the vibrational mode.
[c] E indicates an electronic excitation. If a state designation is given, it identifies the excited state.

Table 10. Additional surface reactions for CHF_3 plasma etching of silicon. [a]

No.	Reaction	A	C	h [b]	Notes[c]
1.	$H + Si(S) \rightarrow Si\_H(S)$	1.0	0.0		S
2.	$H + Si\_H(S) \rightarrow Si(S) + H_2$	0.5	0.0		S
3.	$F + Si\_H(S) \rightarrow Si(S) + HF$	0.1	0.0		S
4.	$CF_2 + Si\_H(S) \rightarrow CHF_2 + Si(S)$	0.4	0.0		S
5.	$CF + Si\_H(S) \rightarrow CHF + Si(S)$	0.4	0.0		S
6.	$CHF_2^+ + e^- + \#Si(B) + 2\#Si\_F_2(S) \rightarrow CHF_2 + \#SiF_4 + 2\#Si(S)$	1.0	0.0	0.876	B [d]
7.	$CHF^+ + e^- + \#Si(B) + 2\#Si\_F_2(S) \rightarrow CHF + \#SiF_4 + 2\#Si(S)$	1.0	0.0	0.550	B [d]
8.	$H^+ + e^- + \#Si(B) + 2\#Si\_F_2(S) \rightarrow H + \#SiF_4 + 2\#Si(S)$	1.0	0.0	0.017	B [d]
9.	$H_2^+ + e^- + \#Si(B) + 2\#Si\_F_2(S) \rightarrow H_2 + \#SiF_4 + 2\#Si(S)$	1.0	0.0	0.034	B [d]
10.	$CF_2^+ + e^- + \#Si(B) + 2\#Si\_H(S) \rightarrow CF_2 + \#H_2 + 2\#Si(S)$	1.0	0.0	0.172	B [e]
11.	$CF_3^+ + e^- + \#Si(B) + 2\#Si\_H(S) \rightarrow CF_3 + \#H_2 + 2\#Si(S)$	1.0	0.0	0.237	B [e]
12.	$CF^+ + e^- + \#Si(B) + 2\#Si\_H(S) \rightarrow CF + \#H_2 + 2\#Si(S)$	1.0	0.0	0.107	B [e]
13.	$F^+ + e^- + \#Si(B) + 2\#Si\_H(S) \rightarrow F + \#H_2 + 2\#Si(S)$	1.0	0.0	0.065	B [e]
14.	$Si^+ + e^- + \#Si(B) + 2\#Si\_H(S) \rightarrow Si + \#H_2 + 2\#Si(S)$	1.0	0.0	0.097	B [e]
15.	$SiF^+ + e^- + \#Si(B) + 2\#Si\_H(S) \rightarrow SiF + \#H_2 + 2\#Si(S)$	1.0	0.0	0.162	B [e]
16.	$SiF_2^+ + e^- + \#Si(B) + 2\#Si\_H(S) \rightarrow SiF_2 + \#H_2 + 2\#Si(S)$	1.0	0.0	0.227	B [e]
17.	$SiF_3^+ + e^- + \#Si(B) + 2\#Si\_H(S) \rightarrow SiF_3 + \#H_2 + 2\#Si(S)$	1.0	0.0	0.293	B [e]
18.	$O^+ + e^- + \#Si(B) + 2\#Si\_H(S) \rightarrow O + \#H_2 + 2\#Si(S)$	1.0	0.0	0.055	B [e]
19.	$O_2^+ + e^- + \#Si(B) + 2\#Si\_H(S) \rightarrow O_2 + \#H_2 + 2\#Si(S)$	1.0	0.0	0.110	B [e]
20.	$CO^+ + e^- + \#Si(B) + 2\#Si\_H(S) \rightarrow CO + \#H_2 + 2\#Si(S)$	1.0	0.0	0.096	B [e]
21.	$CHF_2^+ + e^- + \#Si(B) + 2\#Si\_H(S) \rightarrow CHF_2 + \#H_2 + 2\#Si(S)$	1.0	0.0	0.175	B [e]
22.	$CHF^+ + e^- + \#Si(B) + 2\#Si\_H(S) \rightarrow CHF + \#H_2 + 2\#Si(S)$	1.0	0.0	0.110	B [e]
23.	$H^+ + e^- + \#Si(B) + 2\#Si\_H(S) \rightarrow H + \#H_2 + 2\#Si(S)$	1.0	0.0	0.0034	B [e]
24.	$H_2^+ + e^- + \#Si(B) + 2\#Si\_H(S) \rightarrow H_2 + \#H_2 + 2\#Si(S)$	1.0	0.0	0.0068	B [e]
25.	$CHF^+ + e^- + Si(S) \rightarrow CHF + Si(S)$	1.0	0.0		B
26.	$CHF_2^+ + e^- + Si(S) \rightarrow CHF_2 + Si(S)$	1.0	0.0		B
27.	$H^+ + e^- + Si(S) \rightarrow H + Si(S)$	1.0	0.0		B
28.	$H_2^+ + e^- + Si(S) \rightarrow H_2 + Si(S)$	1.0	0.0		B

[a] Rate parameters of form: $k_f = A \exp(-C/T)$. Units for A depend on the reaction order. Units for C are Kelvin. # indicates a species with an ion energy dependent yield.

[b] Yield coefficients: yield = $h\,(E_{ion}^{0.5} - E_{th}^{0.5})$, where E_{th} is 4 eV.

[c] S in this column indicates a sticking coefficient. B in this column indicates a Bohm reaction. Unless otherwise noted, rate parameters were estimated or fit in this work.

[d] The FORD option has been used to make this reaction first order in $Si\_F_2(S)$ coverage.

[e] The FORD option has been used to make this reaction first order in Si_H(S) coverage.

Table 11. Additional surface reactions for CHF_3 plasma etching of silicon dioxide. [a]

No.	Reaction	A	C	h [b]	Notes[c]
	Adsorption of radicals				
1.	$H + SiO_2(S) \rightarrow SiO_2\_H(S)$	1.0	0.0		S
2.	$H + SiO_2\_H(S) \rightarrow SiO_2(S) + H_2$	0.5	0.0		S
3.	$F + SiO_2\_H(S) \rightarrow SiO_2(S) + HF$	0.1	0.0		S
4.	$CF_2 + SiO_2\_H(S) \rightarrow CHF_2 + SiO_2(S)$	0.4	0.0		S
5.	$CF + SiO_2\_H(S) \rightarrow CHF + SiO_2(S)$	0.4	0.0		S
6.	$CHF_2 + SiO_2(S) \rightarrow SiO_2\_CF_2(S) + H$	1.0	0.0		S
7.	$CHF + SiO_2\_F_2(S) + 0.5SiO_2(S) \rightarrow SiO_2\_CF_2(S) + 0.5SiO_2\_F_2(S) + H$	1.0	0.0		S [d]
	Ion assisted etch				
8.	$CF_2^+ + e^- + \#SiO_2(B) + 2\#SiO_2\_H(S) + \#SiO_2\_CF_2(S) + \#SiO_2\_F_2(S) \rightarrow CF_2 + \#SiF_4 + \#H_2O + \#CO + 4\#SiO_2(S)$	1.0	0.0	0.067	B [e]
9.	$CF_3^+ + e^- + \#SiO_2(B) + 2\#SiO_2\_H(S) + \#SiO_2\_CF_2(S) + \#SiO_2\_F_2(S) \rightarrow CF_3 + \#SiF_4 + \#H_2O + \#CO + 4\#SiO_2(S)$	1.0	0.0	0.093	B [e]
10.	$CF^+ + e^- + \#SiO_2(B) + 2\#SiO_2\_H(S) + \#SiO_2\_CF_2(S) + \#SiO_2\_F_2(S) \rightarrow CF + \#SiF_4 + \#H_2O + \#CO + 4\#SiO_2(S)$	1.0	0.0	0.042	B [e]
11.	$SiF^+ + e^- + \#SiO_2(B) + 2\#SiO_2\_H(S) + \#SiO_2\_CF_2(S) + \#SiO_2\_F_2(S) \rightarrow SiF + \#SiF_4 + \#H_2O + \#CO + 4\#SiO_2(S)$	1.0	0.0	0.063	B [e]
12.	$SiF_2^+ + e^- + \#SiO_2(B) + 2\#SiO_2\_H(S) + \#SiO_2\_CF_2(S) + \#SiO_2\_F_2(S) \rightarrow SiF_2 + \#SiF_4 + \#H_2O + \#CO + 4\#SiO_2(S)$	1.0	0.0	0.090	B [e]
13.	$SiF_3^+ + e^- + \#SiO_2(B) + 2\#SiO_2\_H(S) + \#SiO_2\_CF_2(S) + \#SiO_2\_F_2(S) \rightarrow SiF_3 + \#SiF_4 + \#H_2O + \#CO + 4\#SiO_2(S)$	1.0	0.0	0.116	B [e]
14.	$O_2^+ + e^- + \#SiO_2(B) + 2\#SiO_2\_H(S) + \#SiO_2\_CF_2(S) + \#SiO_2\_F_2(S) \rightarrow O_2 + \#SiF_4 + \#H_2O + \#CO + 4\#SiO_2(S)$	1.0	0.0	0.044	B [e]
15.	$O^+ + e^- + \#SiO_2(B) + 2\#SiO_2\_H(S) + \#SiO_2\_CF_2(S) + \#SiO_2\_F_2(S) \rightarrow O + \#SiF_4 + \#H_2O + \#CO + 4\#SiO_2(S)$	1.0	0.0	0.022	B [e]
16.	$CO^+ + e^- + \#SiO_2(B) + 2\#SiO_2\_H(S) + \#SiO_2\_CF_2(S) + \#SiO_2\_F_2(S) \rightarrow CO + \#SiF_4 + \#H_2O + \#CO + 4\#SiO_2(S)$	1.0	0.0	0.038	B [e]
17.	$CHF_2^+ + e^- + \#SiO_2(B) + 2\#SiO_2\_H(S) + \#SiO_2\_CF_2(S) + \#SiO_2\_F_2(S) \rightarrow CHF_2 + \#SiF_4 + \#H_2O + \#CO + 4\#SiO_2(S)$	1.0	0.0	0.069	B [e]
18.	$CHF^+ + e^- + \#SiO_2(B) + 2\#SiO_2\_H(S) + \#SiO_2\_CF_2(S) + \#SiO_2\_F_2(S) \rightarrow CHF + \#SiF_4 + \#H_2O + \#CO + 4\#SiO_2(S)$	1.0	0.0	0.043	B [e]
19.	$H^+ + e^- + \#SiO_2(B) + 2\#SiO_2\_H(S) + \#SiO_2\_CF_2(S) + \#SiO_2\_F_2(S) \rightarrow H + \#SiF_4 + \#H_2O + \#CO + 4\#SiO_2(S)$	1.0	0.0	0.001	B [e]
20.	$H_2^+ + e^- + \#SiO_2(B) + 2\#SiO_2\_H(S) + \#SiO_2\_CF_2(S) + \#SiO_2\_F_2(S) \rightarrow H_2 + \#SiF_4 + \#H_2O + \#CO + 4\#SiO_2(S)$	1.0	0.0	0.003	B [e]
21.	$CHF_2^+ + e^- + \#SiO_2(B) + 2\#SiO_2\_F_2(S) \rightarrow CHF_2 + \#SiF_4 + \#O_2 + 2\#SiO_2(S)$	1.0	0.0	0.068	B [f]
22.	$CHF^+ + e^- + \#SiO_2(B) + 2\#SiO_2\_F_2(S) \rightarrow CHF + \#SiF_4 + \#O_2 + 2\#SiO_2(S)$	1.0	0.0	0.042	B [f]
23.	$H^+ + e^- + \#SiO_2(B) + 2\#SiO_2\_F_2(S) \rightarrow H + \#SiF_4 + \#O_2 + 2\#SiO_2(S)$	1.0	0.0	0.001	B [f]
24.	$H_2^+ + e^- + \#SiO_2(B) + 2\#SiO_2\_F_2(S) \rightarrow H_2 + \#SiF_4 + \#O_2 + 2\#SiO_2(S)$	1.0	0.0	0.003	B [f]

[a] Rate parameters of form: $k_f = A \exp(-C/T)$. Units for A depend on the reaction order. Units for C are Kelvin. # indicates a species with an ion energy dependent yield.

[b] Yield coefficients: yield = h $(E_{ion}^{0.5} - E_{th}^{0.5})$, where E_{th} is 4 eV.

[c] S in this column indicates that the rate parameters give a sticking coefficient. B in this column indicates a Bohm reaction. Unless otherwise noted, rate parameters were estimated or fit in this work.

[d] The FORD option has been used to make this reaction first order in $SiO_2(S)$ coverage.

[e] The FORD option has been used to make this reaction first order in $SiO_2\_H(S)$ coverage.

[f] The FORD option has been used to make this reaction first order in $SiO_2\_F_2(S)$ coverage.

25.	$CHF_2^+ + e^- + \#SiO_2(B) + 2\#SiO_2\_CF_2(S) \rightarrow CHF_2 + \#SiF_4 + 2\#CO + 2\#SiO_2(S)$	1.0	0.0	0.069	B [g]
26.	$CHF^+ + e^- + \#SiO_2(B) + 2\#SiO_2\_CF_2(S) \rightarrow CHF + \#SiF_4 + 2\#CO + 2\#SiO_2(S)$	1.0	0.0	0.043	B [g]
27.	$H^+ + e^- + \#SiO_2(B) + 2\#SiO_2\_CF_2(S) \rightarrow H + \#SiF_4 + 2\#CO + 2\#SiO_2(S)$	1.0	0.0	0.001	B [g]
28.	$H_2^+ + e^- + \#SiO_2(B) + 2\#SiO_2\_CF_2(S) \rightarrow H_2 + \#SiF_4 + 2\#CO + 2\#SiO_2(S)$	1.0	0.0	0.003	B [g]
	Ion deposition reactions				
29.	$CHF^+ + e^- + 1.5SiO_2(S) + SiO_2\_F_2(S) \rightarrow SiO_2\_CF_2(S) + SiO_2\_H(S) + 0.5SiO_2\_F_2(S)$	0.2	0.0		B [d f]
30.	$CHF_2^+ + e^- + 2.0SiO_2(S) \rightarrow SiO_2\_CF_2(S) + SiO_2\_H(S)$	0.2	0.0		B [d]
	Ion neutralization on open sites				
31.	$CHF^+ + e^- + SiO_2(S) \rightarrow CHF + SiO_2(S)$	0.8	0.0		B
32.	$CHF_2^+ + e^- + SiO_2(S) \rightarrow CHF_2 + SiO_2(S)$	0.8	0.0		B
33.	$H^+ + e^- + SiO_2(S) \rightarrow H + SiO_2(S)$	1.0	0.0		B
34.	$H_2^+ + e^- + SiO_2(S) \rightarrow H_2 + SiO_2(S)$	1.0	0.0		B

[g] The FORD option has been used to make this reaction first order in $SiO_2\_CF_2(S)$ coverage.

5.2. Comparisons with Experiment

The CHF_3/oxide reaction mechanism was developed and tested with a somewhat smaller range of experimental data than the C_2F_6/oxide system. These include measurements of etch rates in one reactor, electron densities, negative ion densities, relative densities of CF, CF_2, and SiF, and ion current densities. The comparisons for this system are summarized in Table 12, with a three-part scale to rate the comparisons. If good agreement (✓) is scored as 3 points, okay agreement (**O**) is scored as 2 points, and poor agreement (✖) is scored as 1 point, the average is a very favorable 2.51. We again attained good overall agreement between model and experiment, but not quite as good as the 2.66 attained for the C_2F_6/oxide system. Figures of all these comparisons are shown below.

Table 12. Summary of Aurora comparisons to experimental data for CHF_3 plasmas.

Reactor	Species	Parameter varied	Direction of trend	Magnitude of trend	Absolute number
II	etch rate	overall	**O**	**O**	✓
II	etch rate	power	**O**	**O**	✓
II	etch rate	pressure	✖	✓	✓
II	etch rate	flow rate	✓	**O**	✓
IA	e^-	power	**O**	**O**	✓
IA	e^-	pressure	✓	**O**	✓
IA	e^-	bias power	**O**	✓	✓
IA	F^-	power	✓	✖	✓
IA	F^-	pressure	✓	✓	✓
IA	F^-	bias power	✖	**O**	✓
IA	CF	power	**O**	✓	--
IA	CF	pressure	✓	✓	--
IA	CF	bias power	**O**	✓	--
IA	CF_2	power	✓	✓	--
IA	CF_2	pressure	✓	**O**	--
IA	CF_2	bias power	**O**	✓	--
IA	SiF	power	✖	✓	--
IA	SiF	pressure	✓	**O**	--
IA	SiF	bias power	**O**	✓	--
II	ICD	power	✓	✓	✓
II	ICD	pressure	**O**	**O**	✓
II	ICD	flow rate	**O**	**O**	✓

✓ = Good, **O** = Okay, ✖ = Poor

5.2.1. Etch Rates

For CHF_3, etch rate data are available only for Reactor II, [20] and the data set is less complete than for C_2F_6. The agreement between model and experiment is very similar for the two gases. The model reproduces the magnitude of the etch rates, but, as for C_2F_6 plasmas, has trouble reproducing some of the trends, especially with pressure.

Etch rate data are shown in Figure 32 as a function of power for three different pressure and two different flow rates. The same data are plotted a different way in Figure 33 to display different features. The open symbols in these plots represent an older set of measurements, which were not really used for fitting the model, but are shown for reference.

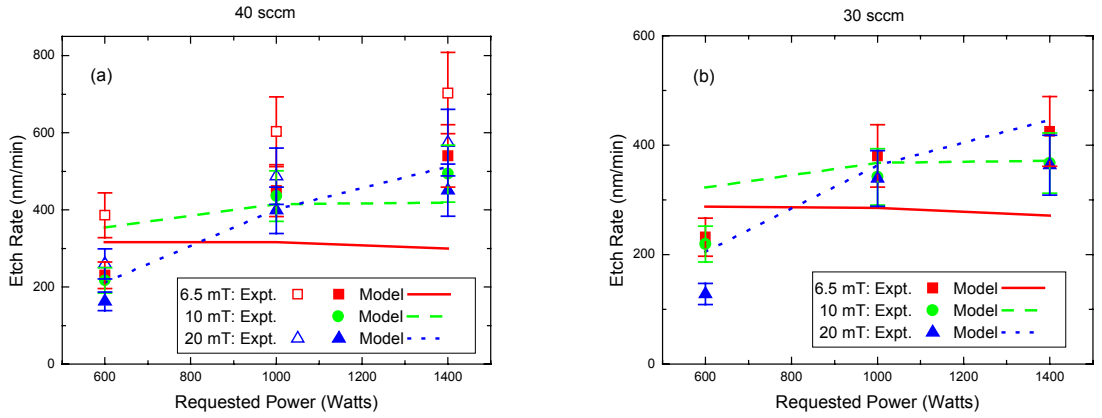

Figure 32. Oxide etch rates for CHF_3 as a function of plasma power for three different pressures and two different flow rates in Reactor II. In (a), open and closed symbols represent older and newer sets of data.

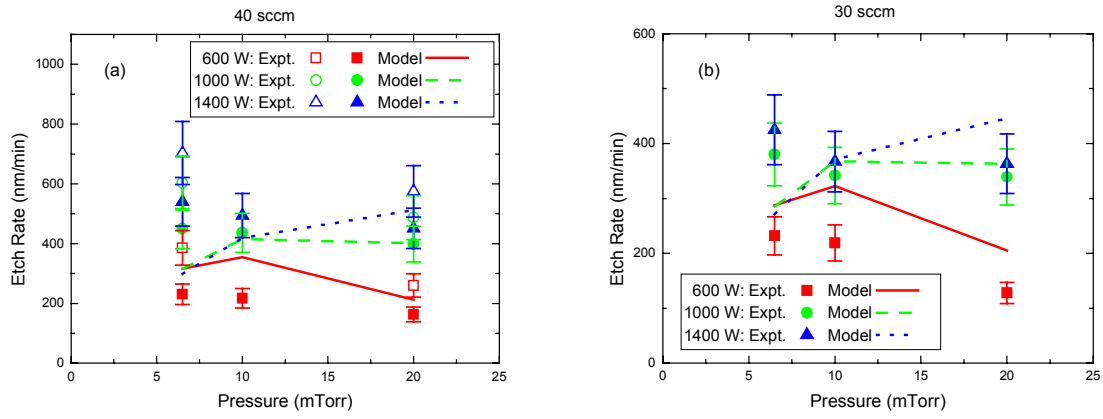

Figure 33. Oxide etch rates for CHF_3 as a function of pressure for three different powers and two different flow rates in Reactor II. In (a), open and closed symbols represent older and newer sets of data.

The model has been adjusted to reproduce the magnitude of the etch rates, but has trouble reproducing some of the trends, especially with pressure. Some of this is caused by compromises made so that the same models could reproduce etch rate data in other reactors for C_2F_6 plasmas. However, in contrast with the C_2F_6 simulations, the etch rates in the CHF_3 simulations do not drop at high power and high pressure, suggesting that the presence of hydrogen on the surface may affect this.

Figure 34 shows experimental and model etch rates as a function of flow rate at 6.5, 10 and 20 mTorr pressure. The model successfully reproduces the increase in etch rate with increasing flow rate. As a result of the difficulties with the pressure dependence, the model predictions are bunched together at low pressures, and more spread out at high pressures, which was also the case for C_2F_6.

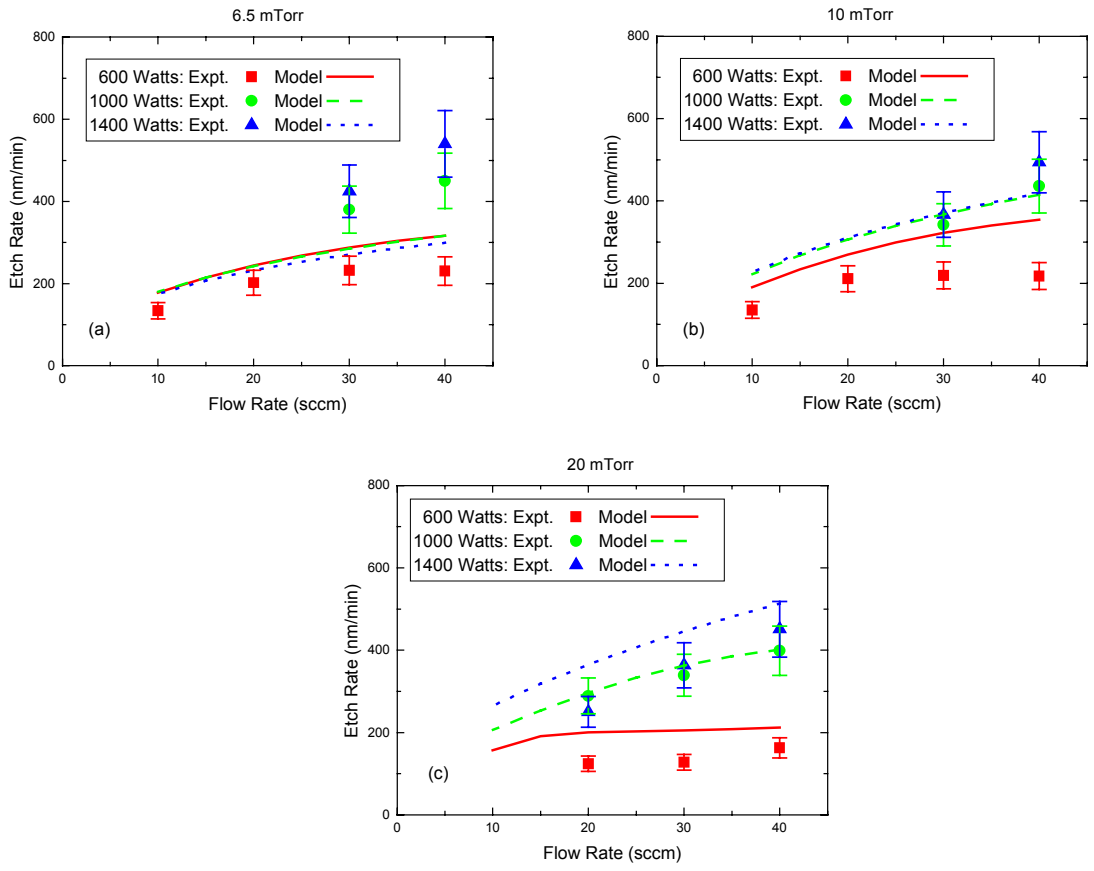

Figure 34. Oxide etch rates for CHF_3 as a function of flow rate for three different powers and pressures in Reactor II.

5.2.2. Electron and Ion Densities

Figure 35 shows experimentally determined electron densities [11] as a function of (a) plasma power, (b) pressure, and (c) bias power, along with the corresponding simulations. Although the model successfully predicts that the electron density increases with power, the dependence is too weak. This flattening at higher powers was also observed in the C_2F_6 simulations, but it was not as severe. For the pressure dependence, the model fits the experimental data quite well, except that it drops too much at the lowest pressures. The low predictions at low pressure were also seen in the C_2F_6 model, which had a distinct peak at ~10 mTorr in contrast to the smoother curve seen here. The dependence on bias power shows a rise in electron density at higher bias powers that is not reproduced by the model, as was the case for C_2F_6. These observations probably indicate that the bias power is adding to the plasma power in addition to accelerating the ions, but the model currently only treats the latter.

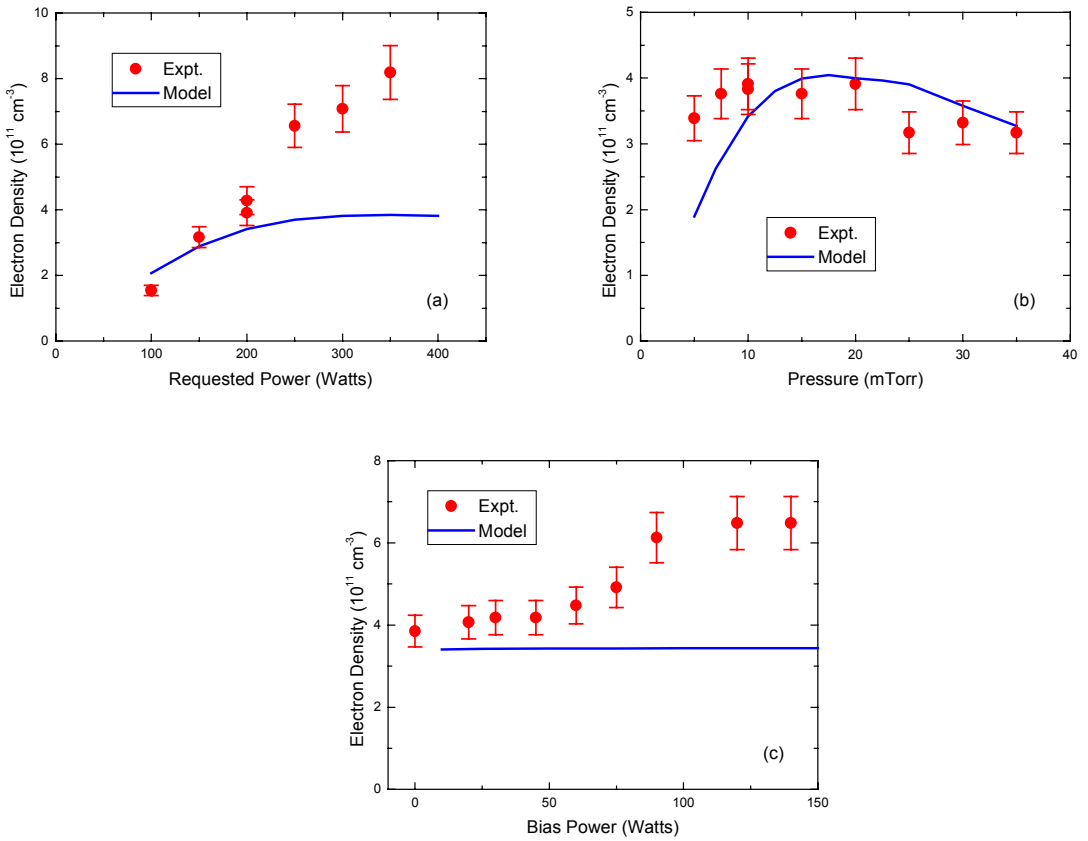

Figure 35. Electron density comparisons between model and experiment for CHF_3 plasmas in Reactor IA. Dependence on: (a) plasma power, (b) pressure, and (c) bias power.

Figure 36 shows negative ion densities [11,13] as a function of (a) plasma power, (b) pressure, and (c) bias power, along with the corresponding simulations. Unlike the electron densities, which were comparable in the CHF_3 and C_2F_6 discharges, the F^- density is ~4-5 times lower in CHF_3 than in C_2F_6. The models successfully reproduce this difference. In the CHF_3 system, F^- is primarily formed by $e + CF_x \rightarrow F^- + CF_{(x-1)}$ and $e + SiF_4 \rightarrow F^- + SiF_3$, whereas for C_2F_6, the dissociative attachment of C_2F_6 itself is the primary route for production of F^-. These differences in the formation reactions probably account for the lower F^- density in the CHF_3 plasmas. The simulations also successfully show a maximum in the power-dependence curves, but in both cases they predict too weak a dependence. For the F^- pressure dependence, the there is good agreement between model and experiment. The bias power dependence, however, experimentally shows the same drop at high bias power as seen for C_2F_6. As for the rise in electron density at high bias, this is probably the result of an effect not included in the model.

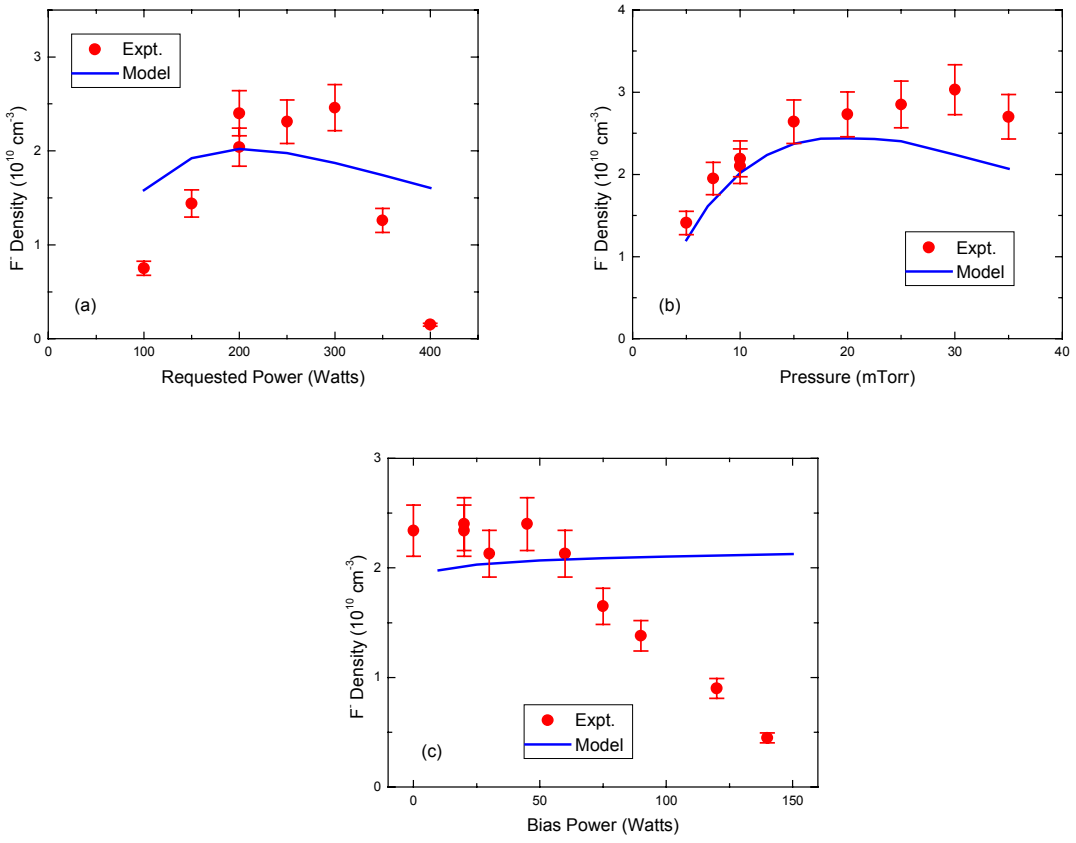

Figure 36. Negative ion density comparisons between model and experiment for CHF_3 in Reactor IA. Dependence on: (a) plasma power, (b) pressure, and (c) bias power.

Figure 37 shows ion current densities (ICDs) for CHF_3 in Reactor II [20] as a function of plasma power for four different flow rates. Figure 38 shows pressure dependencies at two of the flow rates. As expected, many of the same features seen in the etch rate comparisons are also evident in the ICDs. These figures are also qualitatively similar to those for C_2F_6, except that the CHF_3 results do not drop as much with increasing pressure, especially at higher power. Figure 39 shows ICDs as a function of flow rate for three power levels at three pressures. In contrast with the C_2F_6 results, the experimental CHF_3 results show a slight drop with increasing flow rate and then rise again. The model predictions were often higher at low flow rate, but this was correlated with the wrong flow rate dependence to the etch rate, so it was reduced when mechanism was adjusted to fix the etch rate dependence on flow rate. The model predictions for CHF_3 plasmas are much more spread out at higher pressures than they were for C_2F_6.

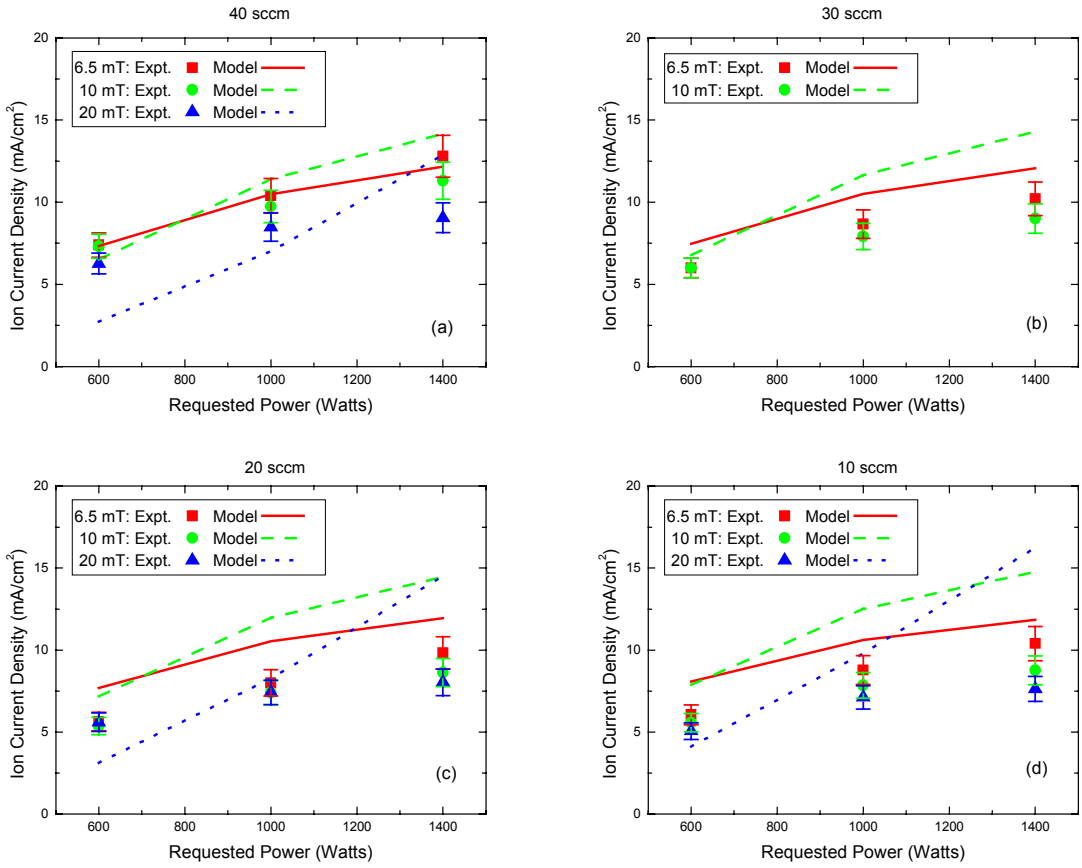

Figure 37. Ion current densities for CHF_3 as a function of plasma power for three different pressures at four different flow rates in Reactor II.

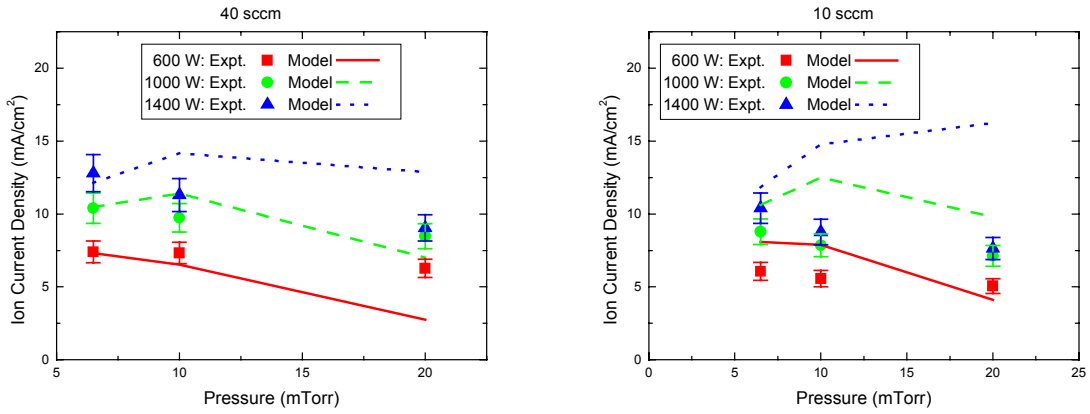

Figure 38. Ion current densities for CHF_3 as a function of pressure for three different powers at two different flow rates in Reactor II.

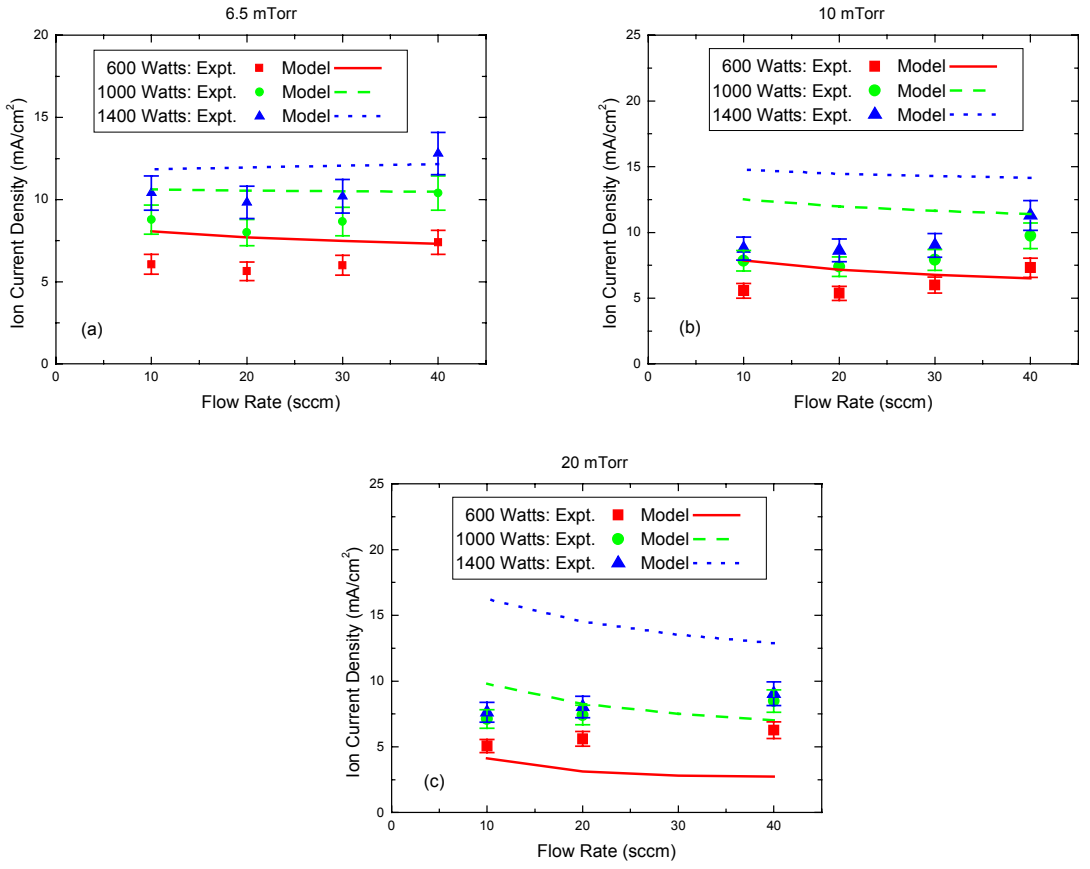

Figure 39. Ion current densities for CHF_3 as a function of flow rate for three different powers and pressures. in Reactor II

5.2.3. Neutral Species Densities

Figure 40 shows a comparison between model and experiment [12] for CF_2 density as a function of (a) plasma power, (b) pressure, and (c) bias power. Both model and experiment show a decrease with increasing power, although the model shows a somewhat stronger dependence, as it did for C_2F_6. CF_2 densities increase with pressure in both cases, although again, as for C_2F_6, the simulations exhibit too strong a dependence. They also agree that CF_2 densities are fairly independent of bias power. For this species, the LIF experiments were done in such a way that they can be compared across gases. The experiments show that the CF_2 density in the CHF_3 plasma at the nominal conditions should be ~×4 lower than in the analogous C_2F_6 plasma. The current models, however, predict a larger ~×10 difference.

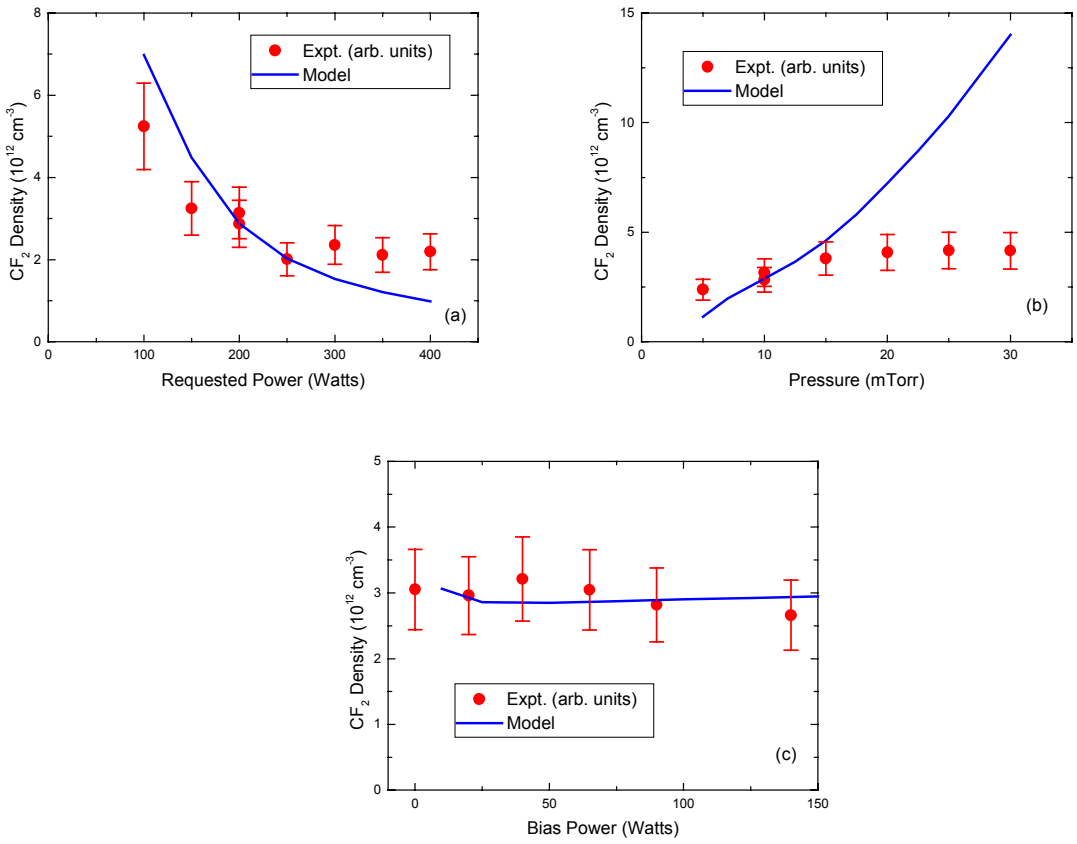

Figure 40. CF_2 density comparisons between model and experiment (arbitrary units) for CHF_3 in Reactor IA. Dependence on: (a) plasma power, (b) pressure, and (c) bias power.

Figure 41 shows comparisons between model and experiment [12] for CF densities as a function of (a) plasma power, (b) pressure, and (c) bias power. The experimental numbers shown were obtained from LIF measurements at the center of the reactor, and a single scaling factor has been applied to all the experimental data to compare it with the model. The fact that the measurements at the default conditions vary from ~4 to ~6 in the graphs reflects the between-run reproducibility of the experiments, as the same scaling factor was used for the three graphs. The simulations reproduces the trend of mildly decreasing CF density with increased power, although it shows a drop at low power that is not evident in the experiments. This was much more noticeable in the C_2F_6 simulations. There is excellent agreement between model and experiment that the CF density increases as a function of pressure and basically does not change with bias power.

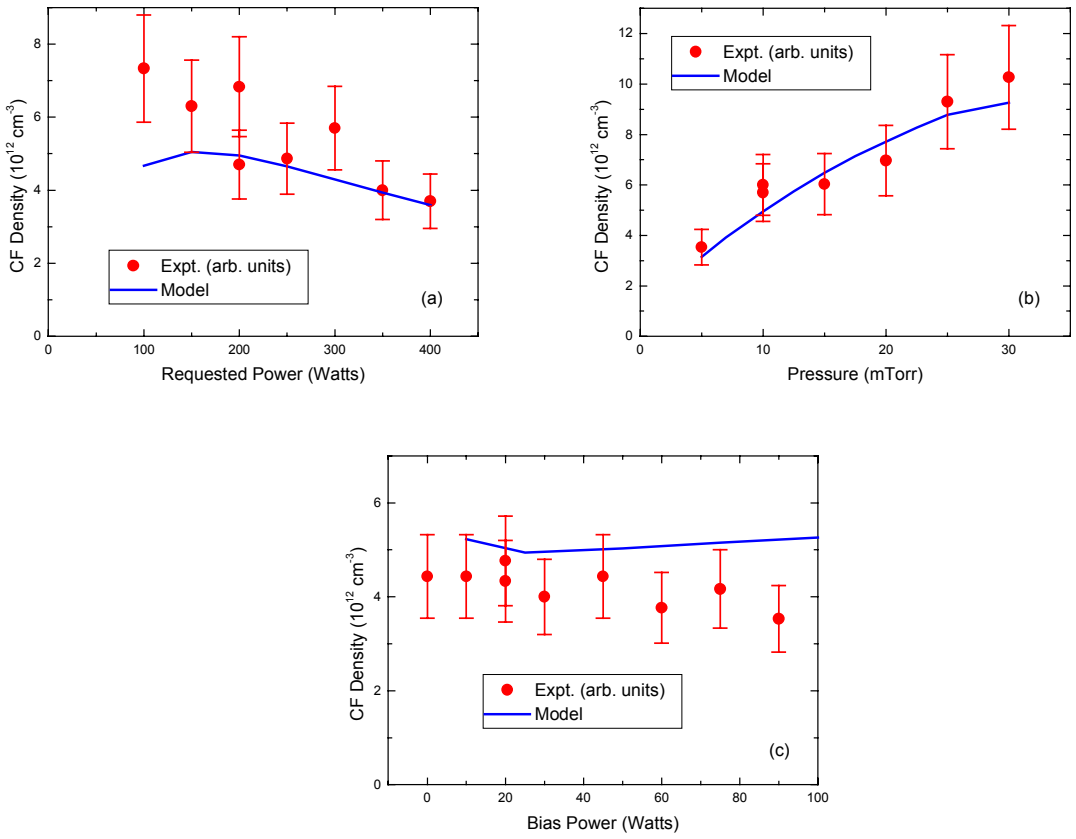

Figure 41. CF density comparisons between model and experiment (arbitrary units) for CHF_3 in Reactor IA. Dependence on: (a) plasma power, (b) pressure, and (c) bias power.

Figure 42 shows comparisons between model and experiment [12] for SiF as a function of (a) plasma power, (b) pressure, and (c) bias power for CHF_3 plasmas. These comparisons provide examples of "poor" and "okay" agreement between model and experiment. In this case, the simulations show a decrease in SiF density at high power that is not seen in the measurements. For SiF in CHF_3, the plasma power and bias power comparisons are comparable to those shown in Figure 23 for C_2F_6. However, the pressure dependence for CHF_3 seen in the simulations is a smoothly increasing curve, which agrees much better with experiment than the strongly-peaked pressure dependence seen for C_2F_6.

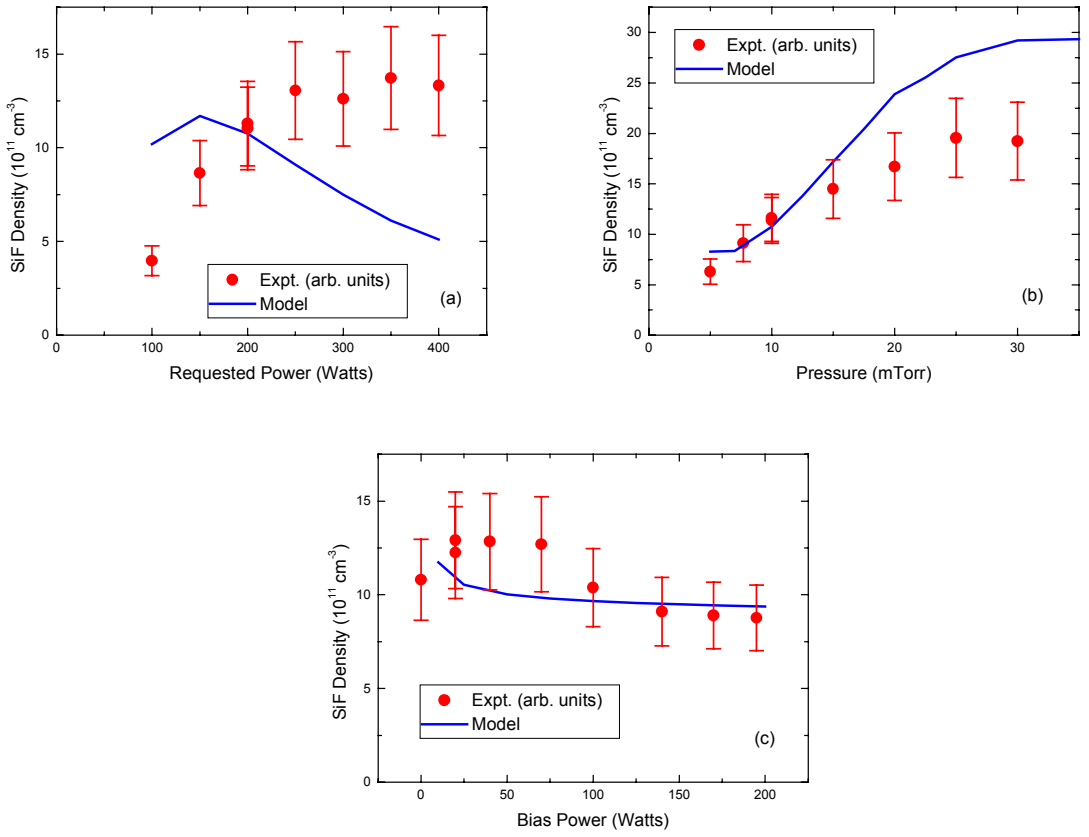

Figure 42. SiF density comparisons between model and experiment (arbitrary units) for CHF_3 in Reactor IA. Dependence on: (a) plasma power, (b) pressure, and (c) bias power.

6. C_4F_8 Etch of Silicon Dioxide

Octafluorocyclobutane, C_4F_8, is of increasing interest for plasma etching of silicon dioxide. This system represents a fairly straightforward extension of the C_2F_6/oxide work. A substantial amount of experimental data for this system was available to use in model validation.

6.1. Reaction Mechanism

The additional reactions in the mechanism for this system are given at the end of this subsection. They are again in three Tables, one for each of the CHEMKIN and Surface-CHEMKIN input files. The gas-phase reaction mechanism for C_4F_8 oxide etching is the C_2F_6 oxide etch mechanism with the addition of 18 reactions describing the electron impact dissociation of C_4F_8, C_3F_5 and C_2F_4, given in Table 13. The electron-impact dissociation and dissociative ionization of C_3F_5 was included to prevent unrealistic buildup of this species in the system, but had little effect on the model predictions that were compared with experiment. For these new reactions, rate parameters were either obtained from Morgan [26] or estimated from related reactions.

For the silicon surface, the surface reaction mechanism is predominantly the C_2F_6 mechanism, with the addition of the 4 reactions shown in Table 14 for $C_2F_4^+$ and $C_3F_5^+$ ions. For these reactions, the rate constants determined from the same mass-weighted scheme used for the lighter ions in the C_2F_6 mechanism.

For the oxide surface, the surface reaction mechanism is again predominantly the C_2F_6 mechanism, with the addition the 22 reactions shown in Table 15. These consist of ion-assisted reactions for $C_2F_4^+$ and $C_3F_5^+$, and the reaction of C_2F_4 with open sites on the surface, which produces a surface C_2F_4 species, $SiO_2\_C_2F_4(S)$. The latter undergoes ion-assisted decomposition on the surface to form CF_2 on the surface, which can participate in further reactions such as ion-assisted etching, plus CF_2 in the gas. C_4F_8 plasmas are known to be much more polymerizing than other fluorocarbon plasmas, so it was deemed necessary to add reactions to represent this phenomenon. Note that none of the reactions contained in the C_2F_6 reaction mechanism were altered; all fitting to C_4F_8 experiments was done only by varying rate constants for the newly added reactions, many of which are estimates. The reaction of C_2F_4 with open sites on the surface has a sticking coefficient of 0.1, which is a moderate reaction probability. In this case, an open site can be viewed as a radical site with an unpaired electron, and a reaction with species containing a carbon-carbon double bond can propagate the radical site. Although the systems are quite different, free-radical chain-growth has been discussed as a mechanism for plasma polymerization [55]. However, molecular beam experiments [56] showed that the double-bond containing species do not react well with a surface of a growing plasma-deposited polymer film, so the use of an intermediate sticking coefficient seems reasonable. For the ion-assisted decomposition of this $SiO_2\_C_2F_4(S)$ species, the yields are set to 5% of the ion-mass-weighted yield for the corresponding ion-assisted etching via the $SiO_2\_CF_2$ (S) species. The threshold for this reaction was also set to 64 eV, in order to match the relatively high threshold experimentally observed for etching as a function of bias power in reactors IB and II (described below).

Table 13. Additional gas-phase reactions for C_4F_8 plasma etching of silicon dioxide. [a]

No.	Reaction	A	B	C	ε	Notes	Ref.
1.	$e^- + C_4F_8 \rightarrow C_4F_8 + e^-$	9.408E−4	−1.093	7.365E3	0.12	V [b]	26
2.	$e^- + C_4F_8 \rightarrow C_4F_8 + e^-$	6.495E−8	0.0415	9.948E4	8.0	E [c]	26
3.	$e^- + C_4F_8 \rightarrow C_2F_4^+ + C_2F_4 + 2e^-$	6.991E−10	0.4702	2.029E5	11.3	[d]	26
4.	$e^- + C_4F_8 \rightarrow C_3F_5^+ + CF_3 + 2e^-$	1.441E−9	0.4095	2.171E5	13.02	[d]	26
5.	$e^- + C_4F_8 \rightarrow CF_3^+ + C_3F_5 + 2e^-$	7.714E−10	0.3794	2.588E5	12.9	[d]	26
6.	$e^- + C_4F_8 \rightarrow CF_2^+ + C_2F_4 + CF_2 + 2e^-$	6.195E−8	−0.0264	3.137E5	15.4	[d]	26
7.	$e^- + C_4F_8 \rightarrow F^- + C_3F_5 + CF_2$	2.4E−3	−1.277	6.257E4	3.99	[d]	26 [e]
8.	$e^- + C_4F_8 \rightarrow 2C_2F_4 + e^-$	1.0E−8	0.10033	1.591E5	0.67		copy C_2F_6
9.	$e^- + C_4F_8 \rightarrow C_2F_6 + 2CF + e^-$	3.124E−8	0.10033	1.591E5	5.85		copy C_2F_6
10.	$e^- + C_3F_5 \rightarrow CF + C_2F_4 + e^-$	3.124E−8	0.10033	1.591E5	1.86		copy C_2F_6
11.	$e^- + C_3F_5 \rightarrow CF^+ + C_2F_4 + 2e^-$	7.899E−14	1.0093	1.977E5	11.12		copy C_2F_6
12.	$e^- + C_2F_4 \rightarrow C_2F_4 + e^-$	6.788E−8	−0.43279	6.072E3	0.10	V2 [b]	copy C_2F_6
13.	$e^- + C_2F_4 \rightarrow C_2F_4 + e^-$	3.797E−4	−0.77795	2.192E4	0.17	V9 [b]	copy C_2F_6
14.	$e^- + C_2F_4 \rightarrow C_2F_4 + e^-$	2.128E−7	−0.3252	3.676E3	0.15	V11 [b]	copy C_2F_6
15.	$e^- + C_2F_4 \rightarrow CF_2 + CF_2 + e^-$	6.98E−10	0.412	73459	5.0		26
16.	$e^- + C_2F_4 \rightarrow CF^+ + CF_3 + 2e^-$	1.789E−11	0.619	223976	17.68		26
17.	$e^- + C_2F_4 \rightarrow C_2F_4^+ + 2e^-$	1.356E−12	0.824	190322	15.85		26 [f]
18.	$e^- + C_2F_4 \rightarrow C_2F_4^+ + 2e^-$	7.365E−12	0.661	128815	9.89		

[a] Rate coefficients of form: $k_f = A\ T^B \exp(-C/T)$. Units for A depend on the order of the reaction, but are in molecules, cm and s. B is for temperature in K. Units for C are K. ε is the electron collision energy loss in eV.
[b] V indicates a vibrational excitation. If a number is given, it denotes the number of the vibrational mode.
[c] E indicates an electronic excitation. If a state designation is given, it identifies the excited state.
[d] The products of this reaction were guessed.
[e] The reaction rate from the indicated reference has been multiplied by a factor of 2.
[f] This reaction actually produces $C_2F_3^+$, which was not included in this mechanism.

Table 14. Additional surface reactions for C_4F_8 plasma etching of silicon. [a]

No.	Reaction	A	h [b]	Notes [c]
1.	$C_2F_4^+ + E + \#Si(B) + 2\#Si\_F_2(S) \rightarrow C_2F_4 + \#SiF_4 + 2\#Si(S)$	1.0	1.720	B [d]
6.2.	$C_3F_5^+ + E + \#Si(B) + 2\#Si\_F_2(S) \rightarrow C_3F_5 + \#SiF_4 + 2\#Si(S)$	1.0	2.253	B [d]
6.3.	$C_2F_4^+ + E + Si(S) \rightarrow C_2F_4 + Si(S)$	1.0		B
6.4.	$C_3F_5^+ + E + Si(S) \rightarrow C_3F_5 + Si(S)$	1.0		B

[a] Sticking and Bohm coefficients of form: $k_f = A \exp(-C/T)$, with C = 0 K for these reactions. # indicates a species with an ion energy dependent yield.
[b] Yield coefficients: yield = $h\ (E_{ion}^{0.5} - E_{th}^{0.5})$, where E_{th} is 4 eV.
[c] S in this column indicates that the rate parameters give a sticking coefficient. B in this column indicates a Bohm reaction. Unless otherwise noted, rate parameters were estimated or fit in this work.
[d] The FORD option has been used to make this reaction first order in $Si\_F_2(S)$ coverage.

Table 15. Additional surface reactions for C_4F_8 plasma etching of silicon dioxide. [a]

No.	Reaction	A	h [b]	E_{th} [b]	Notes [c]
	Additional ions				
1.	$C_2F_4^+ + E + \#SiO_2(B) + 2\#SiO_2\_F_2(S) \rightarrow C_2F_4 + \#SiF_4 + \#O_2 + 2\#SiO_2(S)$	1.0	0.132	4.0	B [d]
6.5.	$C_3F_5^+ + E + \#SiO_2(B) + 2\#SiO_2\_F_2(S) \rightarrow C_3F_5 + \#SiF_4 + \#O_2 + 2\#SiO_2(S)$	1.0	0.173	4.0	B [d]
6.6.	$C_2F_4^+ + E + \#SiO_2(B) + 2\#SiO_2\_CF_2(S) \rightarrow C_2F_4 + \#SiF_4 + 2\#CO + 2\#SiO_2(S)$	1.0	0.132	4.0	B [e]
6.7.	$C_3F_5^+ + E + \#SiO_2(B) + 2\#SiO_2\_CF_2(S) \rightarrow C_3F_5 + \#SiF_4 + 2\#CO + 2\#SiO_2(S)$	1.0	0.173	4.0	B [e]
6.8.	$C_2F_4^+ + E + 2SiO_2(S) \rightarrow 2SiO_2\_CF_2(S)$	0.2			B [f]
6.9.	$C_3F_5^+ + E + 2SiO_2(S) \rightarrow 2SiO_2\_CF_2(S) + CF$	0.2			B [f]
6.10.	$C_2F_4^+ + E + SiO_2(S) \rightarrow C_2F_4 + SiO_2(S)$	0.8			B
6.11.	$C_3F_5^+ + E + SiO_2(S) \rightarrow C_3F_5 + SiO_2(S)$	0.8			B
	Additional $SiO_2\_C_2F_4$ surface species				
6.12.	$C_2F_4 + SiO_2(S) \rightarrow SiO_2\_C_2F_4(S)$	0.1			S
6.13.	$CF_2^+ + E + \#SiO_2\_C_2F_4(S) \rightarrow CF_2 + \#CF_2 + \#SiO_2\_CF_2(S)$	1.0	0.0034	64.0	B
6.14.	$CF_3^+ + E + \#SiO_2\_C_2F_4(S) \rightarrow CF_3 + \#CF_2 + \#SiO_2\_CF_2(S)$	1.0	0.0046	64.0	B
6.15.	$CF^+ + E + \#SiO_2\_C_2F_4(S) \rightarrow CF + \#CF_2 + \#SiO_2\_CF_2(S)$	1.0	0.0021	64.0	B
6.16.	$F^+ + E + \#SiO_2\_C_2F_4(S) \rightarrow F + \#CF_2 + \#SiO_2\_CF_2(S)$	1.0	0.0013	64.0	B
6.17.	$C_2F_4^+ + E + \#SiO_2\_C_2F_4(S) \rightarrow C_2F_4 + \#CF_2 + \#SiO_2\_CF_2(S)$	1.0	0.0066	64.0	B
6.18.	$C_3F_5^+ + E + \#SiO_2\_C_2F_4(S) \rightarrow C_3F_5 + \#CF_2 + \#SiO_2\_CF_2(S)$	1.0	0.0086	64.0	B

[a] Sticking and Bohm coefficients of form: $k_f = A \exp(-C/T)$, with C = 0 K for these reactions. # indicates a species with an ion energy dependent yield.
[b] Yield coefficients: yield = $h (E_{ion}^{0.5} - E_{th}^{0.5})$.
[c] S in this column indicates that the rate parameters give a sticking coefficient. B in this column indicates a Bohm reaction. Unless otherwise noted, rate parameters were estimated or fit in this work.
[d] The FORD option has been used to make this reaction first order in $SiO_2\_F_2(S)$ coverage.
[e] The FORD option has been used to make this reaction first order in $SiO_2\_CF_2(S)$ coverage.
[f] The FORD option has been used to make this reaction first order in $SiO_2(S)$ coverage.

6.19.	$Si^+ + E + \#SiO_2\_C_2F_4(S) \rightarrow Si + \#CF_2 + \#SiO_2\_CF_2(S)$	1.0	0.0019	64.0	B
6.20.	$SiF^+ + E + \#SiO_2\_C_2F_4(S) \rightarrow SiF + \#CF_2 + \#SiO_2\_CF_2(S)$	1.0	0.0032	64.0	B
6.21.	$SiF_2^+ + E + \#SiO_2\_C_2F_4(S) \rightarrow SiF_2 + \#CF_2 + \#SiO_2\_CF_2(S)$	1.0	0.0045	64.0	B
6.22.	$SiF_3^+ + E + \#SiO_2\_C_2F_4(S) \rightarrow SiF_3 + \#CF_2 + \#SiO_2\_CF_2(S)$	1.0	0.0058	64.0	B
6.23.	$O^+ + E + \#SiO_2\_C_2F_4(S) \rightarrow O + \#CF_2 + \#SiO_2\_CF_2(S)$	1.0	0.0010	64.0	B
6.24.	$O_2^+ + E + \#SiO_2\_C_2F_4(S) \rightarrow O_2 + \#CF_2 + \#SiO_2\_CF_2(S)$	1.0	0.0022	64.0	B
6.25.	$CO^+ + E + \#SiO_2\_C_2F_4(S) \rightarrow CO + \#CF_2 + \#SiO_2\_CF_2(S)$	1.0	0.0019	64.0	B

6.26. Comparisons with Experiment

For development and testing the reaction mechanism for the C_4F_8/oxide system, we have etch rate data in two reactors, as well as measurements of electron and negative ion densities, and relative densities of CF_2, SiF and SiF_2. The results of comparisons between model and experiment are summarized in Table 16. The details of these comparisons, including figures and a limited amount of discussion, are given later. As for the results obtained for the C_2F_6 and CHF_3 mechanisms, the overall agreement between model and experiment is quite good, but imperfect. Generally, somewhat worse fits to any individual data set were accepted in order to get a better overall fit to the entire set of data. If good agreement (✓) is scored as 3 points, okay agreement (**O**) is scored as 2 points, and poor agreement (✖) is scored as 1 point, the average is a very favorable 2.50. This score for C_4F_8 is comparable to the scores of 2.66 obtained for C_2F_6 and 2.51 for CHF_3.

6.26.1. Etch Rates

Etch rate data were available for reactors IB [15] and II [20]. The first notable observation is that the experimental etch rates in these two reactors exhibit different dependencies on the fluorocarbon gas source. As shown in Figure 43(a), etch rates in the Reactor II using C_2F_6 and C_4F_8 plasmas are comparable in magnitude or higher for C_4F_8 (1000 W plasma power (0.23 W/cc), 90V bias, 6.5 and 20 mTorr). In contrast, Figure 43(b) shows that Reactor IB yields substantially lower etch rates for C_4F_8 plasmas than for C_2F_6 plasmas (350W plasma power (0.63 W/cc), 85 W bias, 15 mTorr). Although the operating conditions for the two reactors are not directly comparable, this represents an immediate challenge to the models, as the reaction mechanism for C_2F_6 plasmas underlying the mechanism was developed to compare equally well with etch rate data from these two reactors. Efforts to get the model to reproduce these differences were not entirely successful, so the current C_4F_8 mechanism was adjusted to be lower than the Reactor II experimental results and higher than the Reactor IB experiments.

The entire set of data available for C_4F_8 plasma etch of oxide in Reactor II is shown in Figure 44, with the corresponding experimental conditions listed in Table 17. The bias is listed as provided in either Volts or Watts. Bias powers of 100-250 W correspond to bias voltages of 50-160 Volts. The C_4F_8 flow rate was 40 sccm. As mentioned above, the model was deliberately adjusted to be generally lower that this set of experimental data, but the overall trends are satisfactorily reproduced.

Table 16. Summary of Aurora Comparisons to Experimental Data for C_4F_8 Plasmas.

Reactor	Species	Parameter varied	Direction of trend	Magnitude of trend	Absolute number
II	Etch Rate	overall	✓	**O**	**O**
II	Etch Rate	power	✓	**O**	**O**
II	Etch Rate	bias power	✓	✓	**O**
IB	Etch Rate	overall	✓	✓	**O**
IB	Etch Rate	power	✓	✓	**O**
IB	Etch Rate	pressure	✖	✓	**O**
IB	Etch Rate	bias power	✓	✓	**O**
IA	e^-	power	✓	✓	✓
IA	e^-	pressure	**O**	✓	**O**
IA	e^-	bias power	✖	✓	✓
IA	F^-	power	✓	**O**	✓
IA	F^-	pressure	✖	**O**	✓
IA	F^-	bias power	✖	✓	✓
IA	CF_2	power	✓	**O**	---
IA	CF_2	pressure	✓	**O**	---
IA	CF_2	bias power	✓	✓	---
IA	CF_2	C_4F_8/C_2F_6	---	---	✓
IA	SiF	power	**O**	✓	---
IA	SiF	pressure	✓	✓	---
IA	SiF	bias power	**O**	✓	---
IA	SiF_2	power	✓	**O**	---
IA	SiF_2	pressure	✖	✓	---
IA	SiF_2	bias power	**O**	✓	---

✓ = Good, **O** = Okay, ✖ = Poor

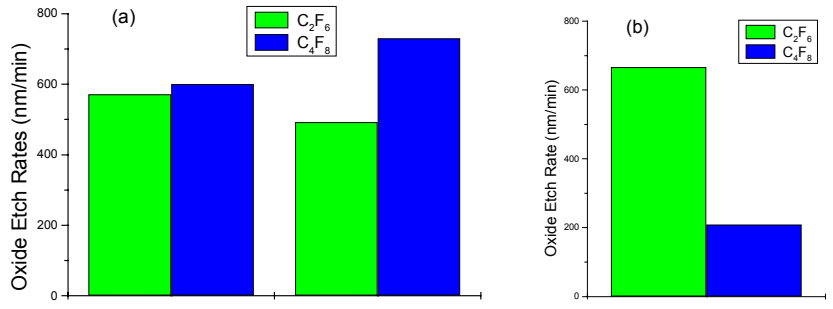

Figure 43. Experimental oxide etch rates in two reactors show different C_2F_6 vs. C_4F_8 gas dependencies. (a) Reactor II, (b) Reactor IB, average of 6 repeats.

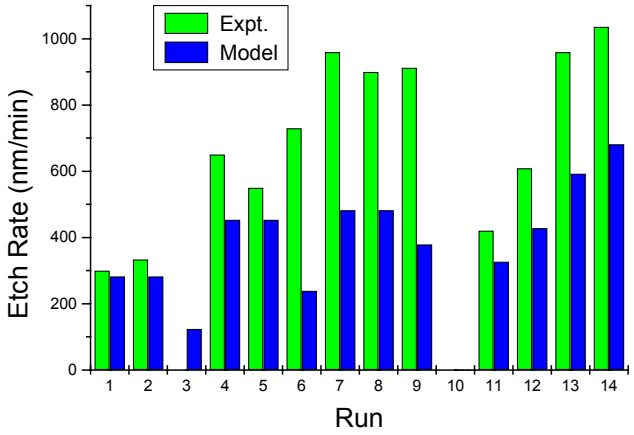

Figure 44. Oxide etch rate comparisons between model and experiment for C_4F_8 in Reactor II. The absence of a bar indicates no etching.

Table 17. Conditions for C_4F_8 plasma etching of oxide shown in Figure 44 for Reactor II.

Run No.	**Plasma Power** (Watts)	**Pressure** (mTorr)	**Bias** (Volts or Watts)
1	600	6.5	90 V
2	600	6.5	90 V
3	600	20	90 V
4	1000	6.5	90 V
5	1000	6.5	90 V
6	1000	20	90 V
7	1400	6.5	90 V
8	1400	6.5	90 V
9	1400	20	90 V
10	1400	6.5	100 W
11	1400	6.5	135 W
12	1400	6.5	150 W
13	1400	6.5	200 W
14	1400	6.5	250 W

For Reactor IB, the full set of etch rate data is shown in Figure 45, with the experimental conditions listed in Table 18. As mentioned above, the model was deliberately adjusted to be generally higher that this set of experimental data, but again many of the trends are satisfactorily reproduced.

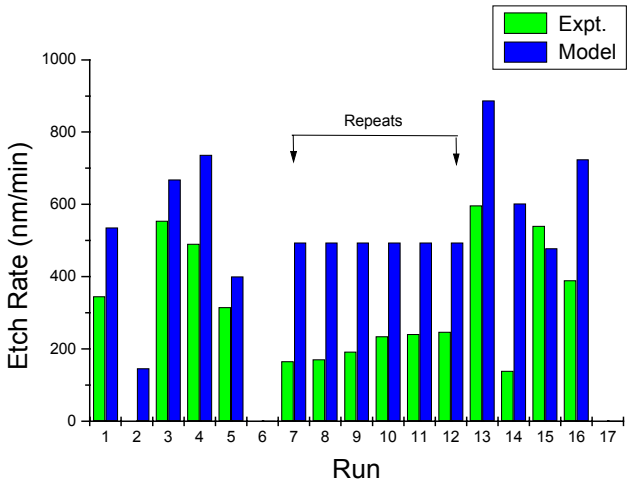

Figure 45. Oxide etch rate comparisons between model and experiment for C_4F_8 in Reactor IB. The absence of a bar indicates no etching.

Table 18. Conditions for C_4F_8 plasma etching of oxide shown in Figure 45 for Reactor IB.

Run No.	**Plasma Power** (Watts)	**Pressure** (mTorr)	**Bias Power** (Watts)
1	204.66	15	85
2	277	8	48
3	277	8	125
4	277	20	125
5	350	5.2	85
6	350	15	22.13
7-12	350	15	85
13	350	15	147.87
14	350	24.8	85
15	455	8	125
16	455	20	125
17	495.34	15	85

It is worthwhile to examine the trends in the etch rate comparisons more closely. Starting with the bias dependence, both model and experiment clearly agree that the etch rate should increase with increasing bias power/voltage. Figure 46 shows experimental etch rates simulations for (a) Reactor II (1400 W plasma power and 6.5 mTorr) and (b) Reactor IB (350 W plasma power and 15 mTorr). As indicated by the open points, the experimental etch rates drop to zero (actually deposition is observed) at the lower bias powers. Simulations using earlier versions of the reaction mechanism showed a much shallower dependence at low bias, as well as generally having much higher etch rates. The reaction of C_2F_4 with open sites on the surface, followed by ion-enhanced decomposition to form CF_2 in the gas and on the surface, was added to the mechanism to steepen the bias dependence. The use of a relatively high threshold energy for the latter allowed the simulations to reproduce the decrease in etch rate at lower bias. These reactions also decrease the etch rate in Reactor IB relative to Reactor II somewhat, but not enough to overlap both sets of data simultaneously.

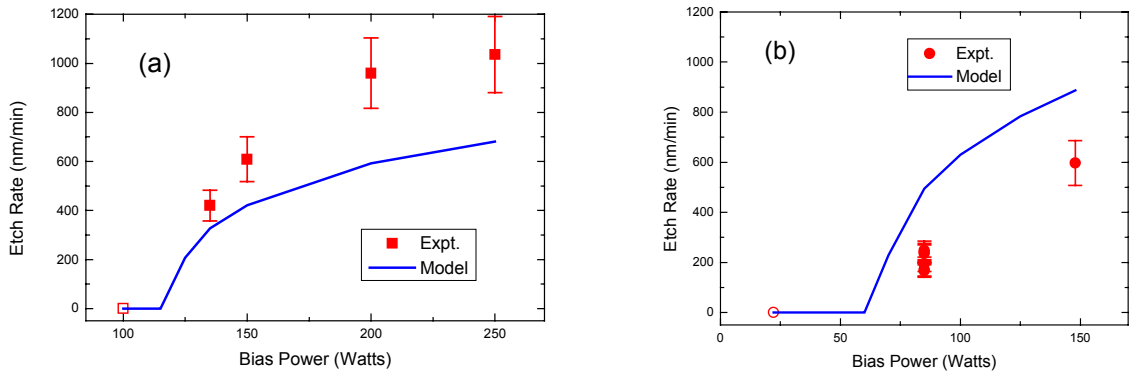

Figure 46. Oxide etch rate dependence on bias power for C_4F_8 in: (a) Reactor II, (b) Reactor IB. Open points indicate no etching.

The experimental data also include a few sets that show the dependence on plasma power and/or pressure. Figure 47 shows the variation of etch rate with plasma power in Reactor II at 90 V bias, 6.5 and 20 mTorr. Model and experiment agree that the etch rate increases with increasing power, but the dependence in the model is somewhat flatter than that observed experimentally. The dependence on pressure is less visible in the figure, but the experimental trends for the three different data pairs are $\downarrow\uparrow\rightarrow$, whereas the simulation shows $\downarrow\downarrow\downarrow$.

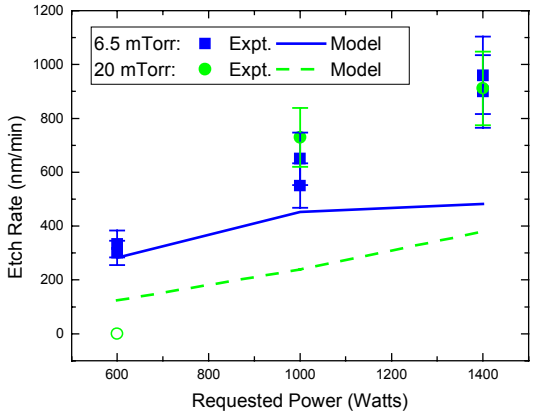

Figure 47. Oxide etch rate dependence on plasma power for C_4F_8 in Reactor II. Open point indicates no etching.

Figure 48(a) shows the variation of etch rate with plasma power in Reactor IB (15 mTorr, 85 W bias). In this case, model and experiment agree that the etch rate decreases with increasing plasma power, dropping off completely at higher powers. Figure 48(b) shows the variation of etch rate with pressure in this reactor (350 W plasma power, 85 W bias). Here, model and experiment disagree as to the sign of the dependence, although the magnitude is about right. There are two other data pairs in this set which allow the direct examination of the pressure dependence. These cases are consistent with Figure 48(b), with the experimental dependence ↓↓ and the model ↑↑.

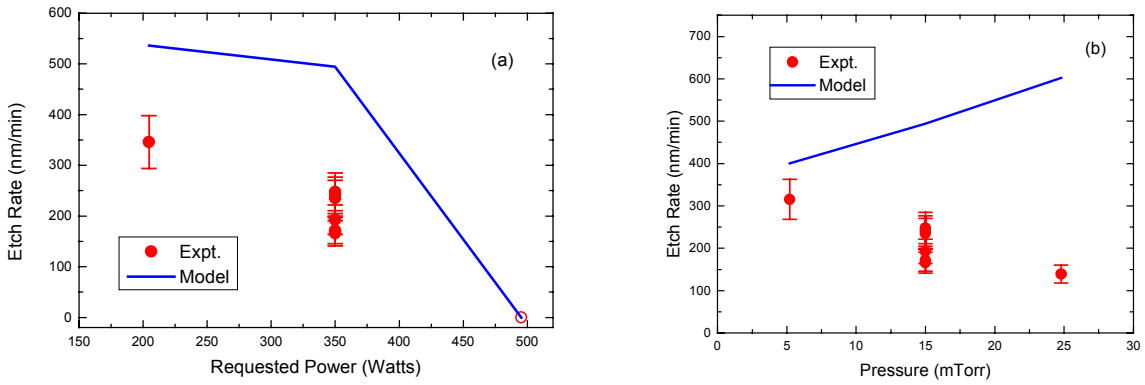

Figure 48. Oxide etch rate dependence for C_4F_8 in Reactor IB on (a) plasma power, and (b) pressure. Open point indicates no etching.

6.26.2. Electron and Ion Densities

Figure 49 shows experimentally measured electron densities [13] in Reactor IA as a function of (a) plasma power, (b) pressure, and (c) bias power, along with the corresponding simulations. The model reproduces the magnitude and the general trends quite well, although differences remain. The experimental and simulated electron densities are generally quite similar for C_4F_8 and C_2F_6 plasmas, although the comparisons for C_4F_8 look somewhat better for the power dependence, and worse for the pressure dependence.

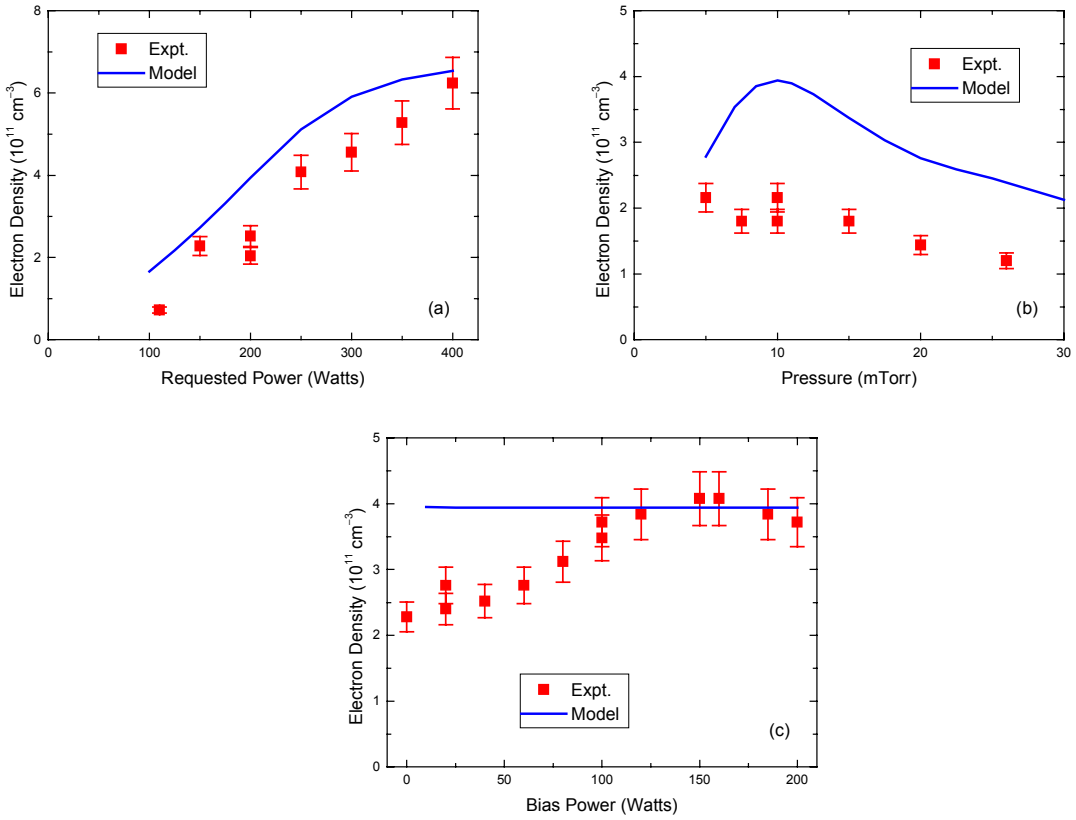

Figure 49. Electron density comparisons between model and experiment for C_4F_8 plasmas in Reactor IA. Dependence on: (a) plasma power, (b) pressure, and (c) bias power.

Figure 50 shows similar plots for F^- densities. In this case, the agreement between model and experiment [13] for C_4F_8 is better than for C_2F_6 plasmas as a function of power, but worse as a function of pressure. The simulations indicate that the dissociative attachment of both C_4F_8 and C_2F_6 are important in producing F^- in C_4F_8 plasmas. As for C_2F_6 and CHF_3 plasmas, the decrease in F^- density and the increase in electron density at higher bias power are not reproduced by the model for C_4F_8 plasmas. This is consistent with the idea that bias power adds to the plasma power in addition to accelerating the ions, but the model only treats the latter.

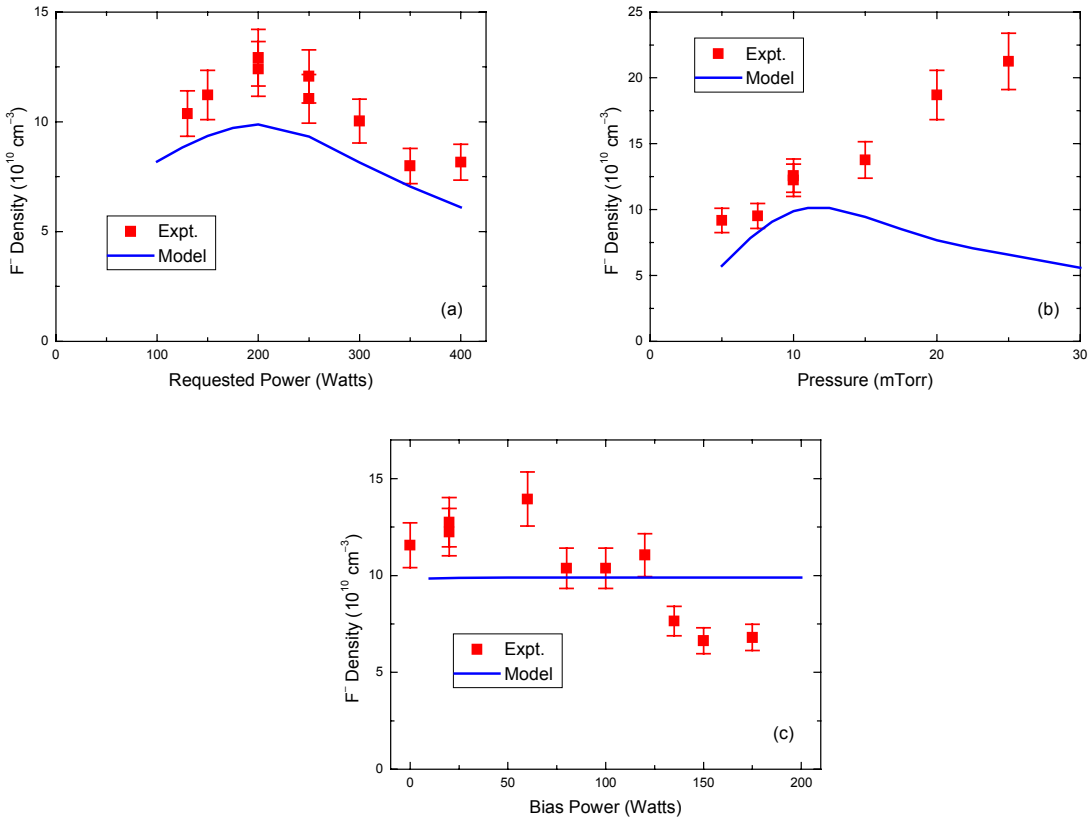

Figure 50. Negative ion density comparisons between model and experiment for C_4F_8 in Reactor IA. Dependence on: (a) plasma power, (b) pressure, and (c) bias power.

6.26.3. Neutral Species Densities

Figure 51 compares model and experiment [12] for CF_2 densities in Reactor IA as a function of (a) plasma power, (b) pressure, and (c) bias power. A single scaling factor has been applied to these centerpoint LIF experimental values to match the simulations at the base conditions (200 W plasma power, 10 mTorr, 10 sccm, and 20 W bias power). The power and pressure dependencies shown in this figure are very similar to the results for C_2F_6 plasmas, where the trends in the model are both correct, but too strong. This is an example where the wafer material significantly affects the trend in the simulations. As shown in Figure 52, the model with an oxide wafer gives a substantial drop in CF_2 density with increasing bias, whereas a silicon wafer gives the flat dependence shown in Figure 51(c). This is probably due to a higher consumption rate of CF_2 via etching of the oxide wafer. Although the LIF technique generally only gives relative densities, in this case the data were taken in such a way that the relative density across plasma gases is known. The experiments indicate that a C_4F_8 plasma at the base conditions gives a CF_2 density 2.33 times higher than a C_2F_6 plasma at the same conditions. The present simulations give a ratio of 2.20, in excellent agreement with experiment. The production of CF_2 via the ion-assisted decomposition of C_2F_4 surface species turns out to be significant in determining the density of CF_2 in the gas.

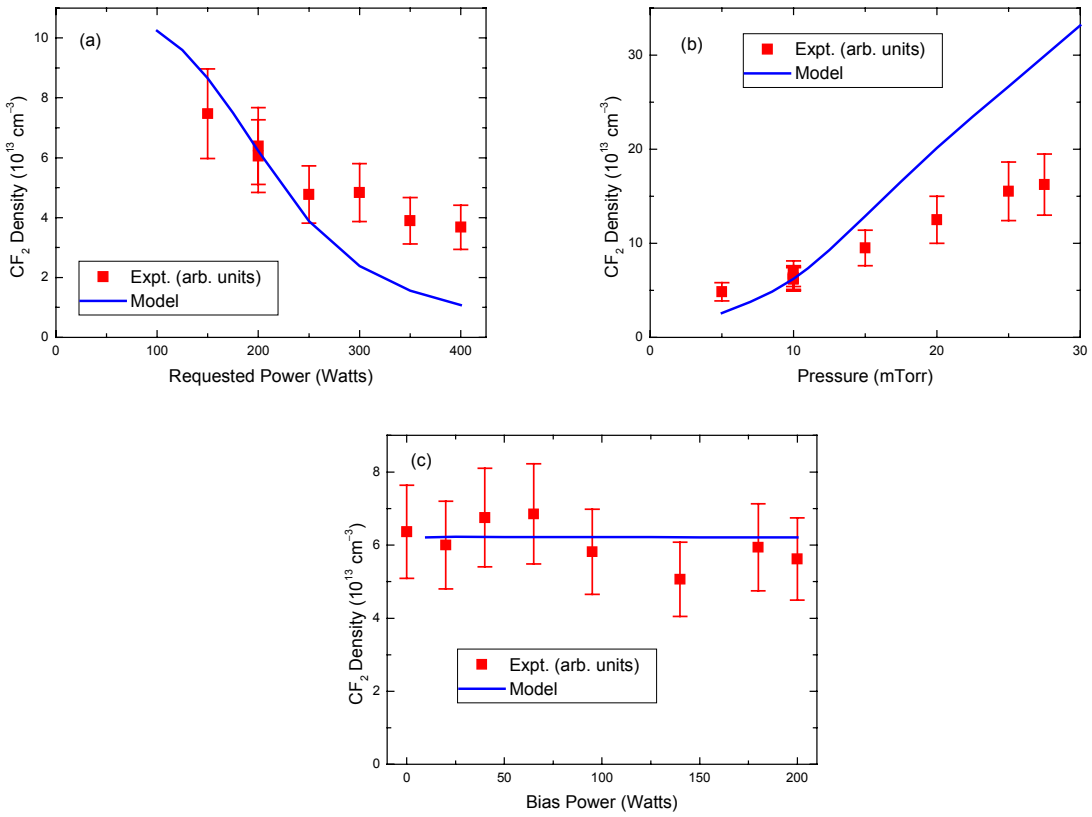

Figure 51. CF_2 density comparisons between model and experiment (arbitrary units) for C_4F_8 in Reactor IA. Dependence on: (a) plasma power, (b) pressure, and (c) bias power.

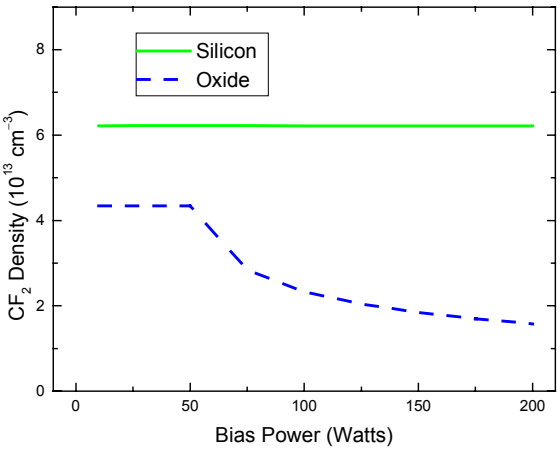

Figure 52. Simulated CF_2 densities show different bias dependencies with silicon and oxide wafers for C_4F_8 in Reactor IA.

Figure 53 shows model and experiment [12] for SiF densities as a function of (a) plasma power, (b) pressure, and (c) bias power. The experimental values have been scaled to overlap the simulations at the base conditions. For this species, the simulations show good agreement for the pressure and bias dependence, but show a decrease in density at high power that is not seen in the experiments. The disagreement for the power dependence is quite similar to that observed for C_2F_6 plasmas, but the agreement for the pressure dependence in C_4F_8 is much better than that obtained for C_2F_6 plasmas.

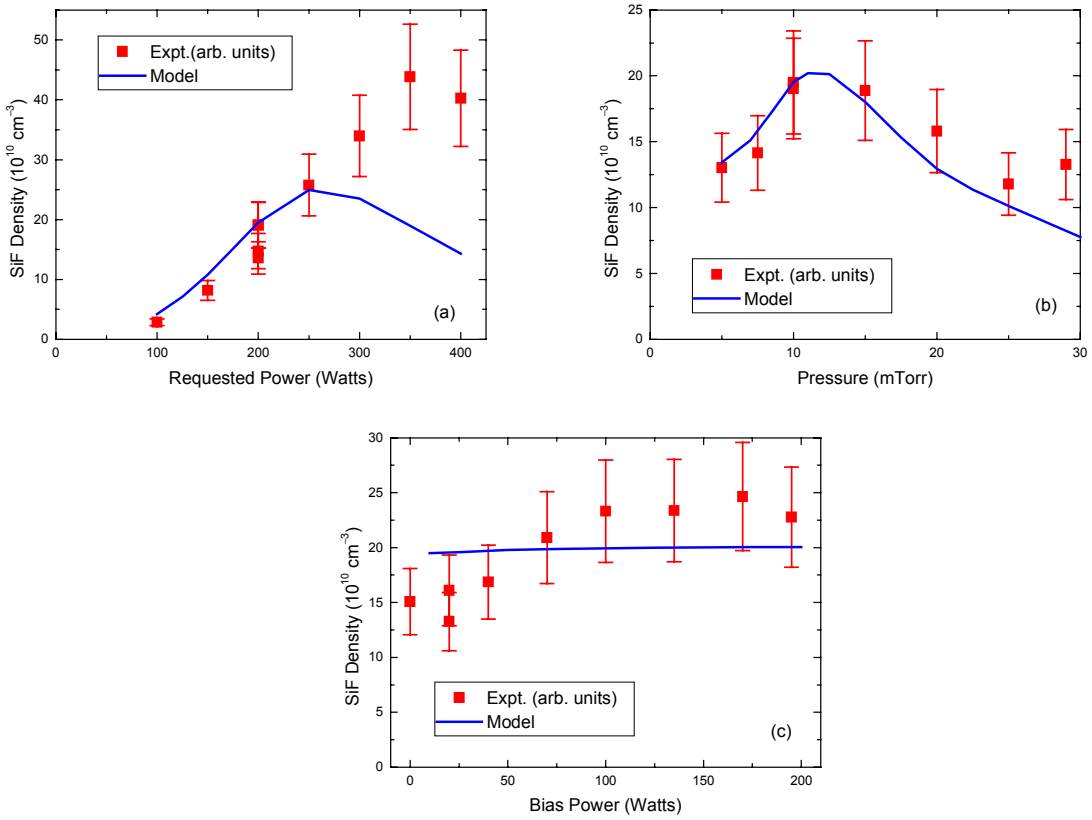

Figure 53. SiF density comparisons between model and experiment (arbitrary units) for C_4F_8 in Reactor IA. Dependence on: (a) plasma power, (b) pressure, and (c) bias power.

Figure 54 shows model and experiment [14] for SiF_2 densities as a function of (a) plasma power, (b) pressure, and (c) bias power. A single scaling factor has again been applied to the experimental values to overlap them with the simulations at the base conditions. For this species, the simulations show good agreement for the power dependence, but also shows a decrease in density at high pressure that is not seen in the experiments. For the bias dependence, the agreement is only okay, but this experimental data set shows more scatter than some of the other measurements and the data in (c) seem systematically low compared to the points in (a) and (b). The disagreement for the pressure dependence is quite similar to that observed for a C_2F_6

plasma, but the agreement for the power dependence in C_4F_8 is much better than that obtained for the C_2F_6 plasma.

LIF only gives relative densities rather than absolute numbers, but in this case the experiments were done in a way that allows comparisons between gases. Experimentally, it is reported [14] that SiF_2 densities are ~3-4 times higher in C_2F_6 plasmas than in C_4F_8 plasmas. The model, in good agreement with experiment, gives a SiF_2 density in C_2F_6 plasmas that is 2.6 times higher than for C_4F_8 for the base conditions.

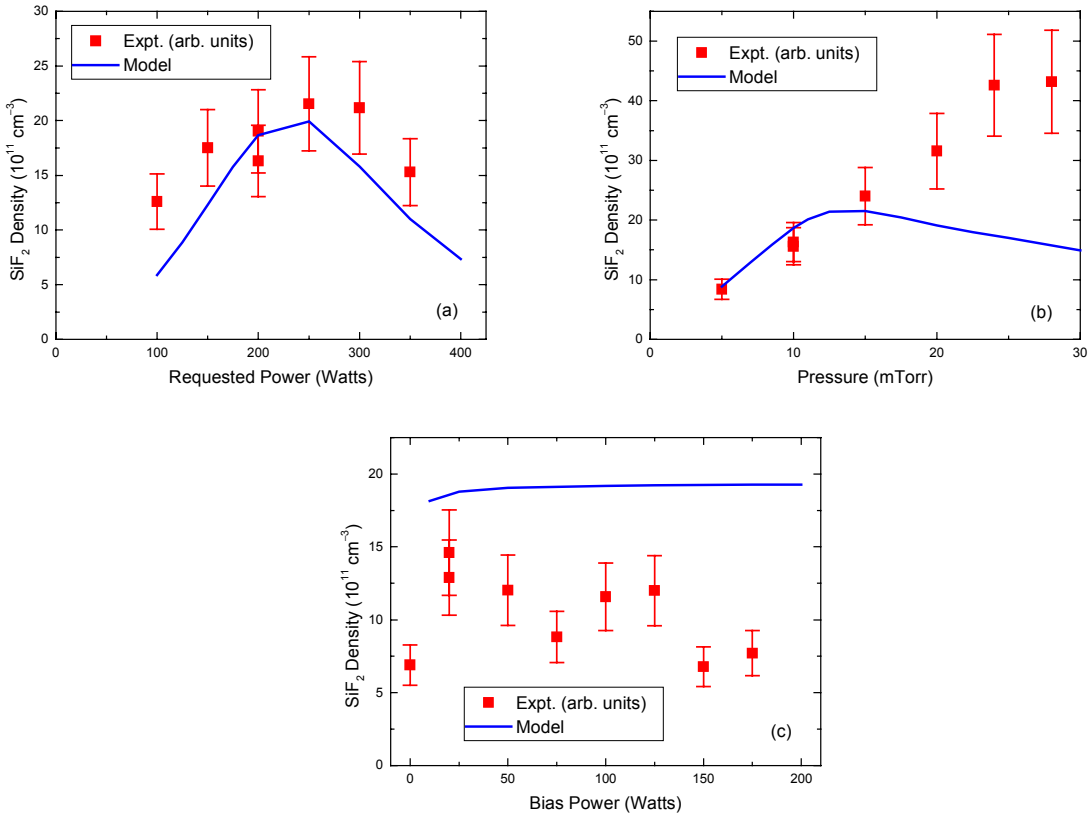

Figure 54. SiF_2 density comparisons between model and experiment (arbitrary units) for C_4F_8 in Reactor IA. Dependence on: (a) plasma power, (b) pressure, and (c) bias power.

As shown in Figure 55, SiF and SiF_2 are both cases where the simulations give different densities using an oxide wafer than a silicon wafer, especially at high bias powers. This is reasonable, given that, in the model, they are both formed by electron-induced dissociation of SiF_4, which is an etch product. In these systems, silicon dioxide etches significantly more rapidly than does silicon, creating more SiF_4. Although the walls have a much higher surface area than the wafer, the etching of the unbiased oxide walls is greatly reduced by the lower ion energies and the thick

polymer coatings (expressed as the C_2F_4 surface species in this mechanism), so the etching of the wafer area noticeably affects the gas-phase composition.

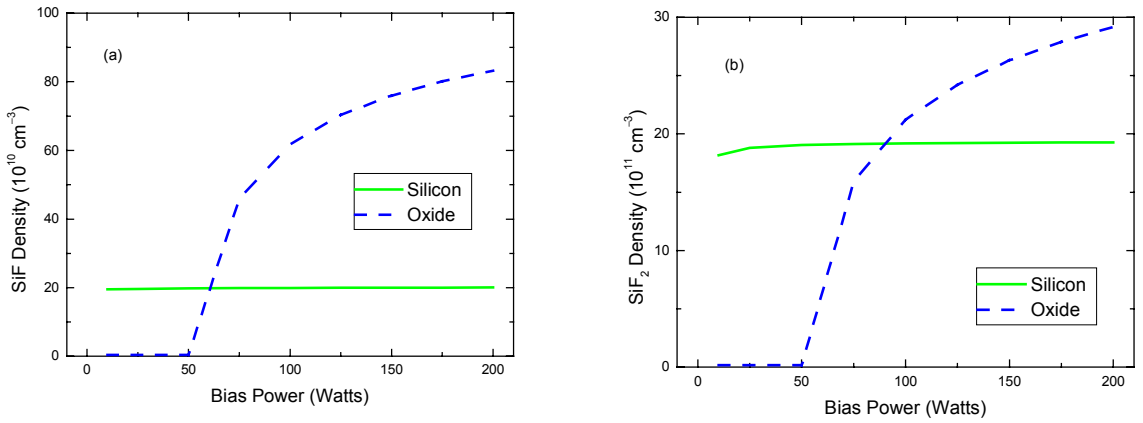

Figure 55. Simulated densities for (a) SiF and (b) SiF_2 show different bias dependencies with silicon and oxide wafers for C_4F_8 in Reactor IA.

7. C_2F_6 Plasma Etch of Photoresist

Although fluorocarbon plasmas are not deliberately used to etch photoresist materials, these masking materials erode during the oxide etch processes. Understanding how the selectivity for oxide vs. photoresist varies as a function of operating parameters is of interest, so we include this system in our modeling work. In contrast with the oxide system, where etch rate data from multiple reactors and a wide variety of diagnostic data were available, the amount of experimental data available for photoresist-etch-mechanism development and validation is quite limited. The results of this work and the mechanism for photoresist etching should thus be used with caution.

7.1. Reaction Mechanism

The chemical reaction mechanism for photoresist etching is heavily drawn from the work on the oxide etch. The gas-phase reaction mechanism for C_2F_6 plasma etching of photoresist is the sum of the C_2F_6 oxide etch mechanism and the CHF_3 oxide etch mechanism. The latter accounts for the plasma dissociation of hydrogen-containing etch products from the photoresist, although it does not represent a complete set of reactions for hydrogen-containing species. A Novolac photoresist was used in the experiments. Based on hints in the MSDS, a chemical formula of C_2H_4O and a density of 1 g/cm^3 were somewhat arbitrarily chosen to represent it in these simulations. Note that this does not imply that the PR has any relationship to other species with this formula such as ethylene oxide or acetaldehyde.

The surface reaction mechanism for photoresist etching generally has two components. The first, given in Table 19, is a reaction mechanism for photoresist surfaces that was fit to the experimental etch rate data. It involves 5 species on the photoresist surface and 90 reactions, plus the bulk photoresist PR(B). These species and reactions were chosen to be analogous to those used in the oxide and silicon surface mechanisms. The second component of the surface reaction mechanism is etching of the oxide sidewalls of the reactor, and consists of the combination of Table 4 plus Table 11 used for CHF_3 plasma etch of oxide. For the simulations of the patterned oxide/photoresist wafer, a third component was added to represent the etching of the exposed oxide on the wafer.

The first category of reactions in Table 19 is the reaction of neutral radicals with various surface species. Some of these reactions significantly affect the relative coverages of the surface species. The next sets describe ion-assisted etching via fluorinated R_F_2(S) sites, CF_2 covered sites, and a combination of hydrogenated R_H(S) and CF_2 covered sites. The last sets of reactions are sputtering of graphitized sites R_C(S) and open sites R(S), respectively. The rates for the radical/surface reactions, along with the ion-assisted etch yields, were generally adjusted to get the best overall fit to the data. As for oxide etch, the yields of the ions were scaled by the relative masses of the ions, so the yields for a class of ion-assisted reaction really represent only one adjustable prefactor and one adjustable threshold parameter. In a few cases, independent information was available to guide the choices of rate parameters. For sputtering of photoresist via open R(S) sites, the yields are based on Graves'[57] experimental measurements of argon ion sputtering. These workers have also shown that hydrogen on the photoresist surface is abstracted by F atoms with a probability of ~0.2, which is close to the 0.1 used for Reaction 5 in Table 19.

Although we include reactions for ion-assisted etching via a number of pathways, these simulations show that most of the photoresist etching occurring via the R_CF_2(S) species. The surface is generally covered primarily by this species and the R_C(S) species, which represents a graphitized surface. Within this model, the R_C(S) species serves to block the surface and decrease the etch rate under certain conditions because it requires removal either by reaction with F or by sputtering away by ions. The current structure of the mechanism, with etching via the R_CF_2(S) species form the R_C(S) species which is then removed in a separate step, was developed in order to reproduce the observed trends in both reactors. Other schemes that were tried could generally be adjusted to reproduce the experiments in one of the two reactors, but with very unacceptable results for the other.

Table 19. Surface reactions for fluorocarbon plasma etching of photoresist. [a]

No.	Reaction	A	h	E_{th}	Notes [b]
	neutral reactions				
1.	$F + 0.5R(S) \rightarrow 0.5R\_F_2(S)$	0.001			S [c]
7.2.	$F + 0.5R\_C(S) \rightarrow 0.5R\_CF_2(S)$	0.001			S [d]
7.3.	$H + R(S) \rightarrow R\_H(S)$	1.0			S
7.4.	$H + R\_H(S) \rightarrow R(S) + H_2$	0.5			S
7.5.	$F + R\_H(S) \rightarrow R(S) + HF$	0.1			S
7.6.	$CF_3 + 1.5R(S) \rightarrow R\_CF_2(S) + 0.5R\_F_2(S)$	0.20			S [c]
7.7.	$CF_2 + R(S) \rightarrow R\_CF_2(S)$	1.0			S
7.8.	$CF + R(S) \rightarrow 0.5R\_CF_2(S) + 0.5R\_C(S)$	1.0			S
7.9.	$CHF + R(S) \rightarrow R\_C(S) + HF$	0.1			S
7.10.	$C + R(S) \rightarrow R\_C(S)$	0.5			S
7.11.	$C + R\_F_2(S) \rightarrow CF_2 + R(S)$	0.01			S
7.12.	$C + R\_CF_2(S) \rightarrow CF_2 + R\_C(S)$	0.01			S
7.13.	$F + 0.5R\_CF_2(S) \rightarrow 0.5CF_4 + 0.5R(S)$	0.01			S [e]
7.14.	$CF_3 + R\_C(S) \rightarrow R\_CF_2(S) + CF$	0.10			S

[a] Sticking and Bohm coefficients of form: $k_f = A \exp(-C/T)$, with C = 0 K for these reactions. # indicates a species with an ion energy dependent yield.

[b] S in this column indicates that the rate parameters give a sticking coefficient. B indicates a Bohm reaction. Unless otherwise noted, rate parameters were estimated or fit in this work.

[c] The FORD option has been used to make this reaction first order in R(S) coverage.

[d] The FORD option has been used to make this reaction first order in R_C(S) coverage.

[e] The FORD option has been used to make this reaction first order in R_CF_2(S) coverage.

7.15.	$CF_2 + R\_C(S) \rightarrow R\_CF_2(S) + C$	0.10			S
	Ion assisted etch, fluorinated sites				
7.16.	$CF_3^+ + e^- + \#PR(B) + \#R\_F_2(S) \rightarrow CF_3 + \#CF_2 + 2\#H_2 + \#CO + \#R(S)$	1.0	0.086	16.0	B
7.17.	$CF_2^+ + e^- + \#PR(B) + \#R\_F_2(S) \rightarrow CF_2 + \#CF_2 + 2\#H_2 + \#CO + \#R(S)$	1.0	0.0625	16.0	B
7.18.	$CF^+ + e^- + \#PR(B) + \#R\_F_2(S) \rightarrow CF + \#CF_2 + 2\#H_2 + \#CO + \#R(S)$	1.0	0.0385	16.0	B
7.19.	$CHF_2^+ + e^- + \#PR(B) + \#R\_F_2(S) \rightarrow CHF_2 + \#CF_2 + 2\#H_2 + \#CO + \#R(S)$	1.0	0.0635	16.0	B
7.20.	$CHF^+ + e^- + \#PR(B) + \#R\_F_2(S) \rightarrow CHF + \#CF_2 + 2\#H_2 + \#CO + \#R(S)$	1.0	0.040	16.0	B
7.21.	$O_2^+ + e^- + \#PR(B) + \#R\_F_2(S) \rightarrow O_2 + \#CF_2 + 2\#H_2 + \#CO + \#R(S)$	1.0	0.040	16.0	B
7.22.	$O^+ + e^- + \#PR(B) + \#R\_F_2(S) \rightarrow O + \#CF_2 + 2\#H_2 + \#CO + \#R(S)$	1.0	0.020	16.0	B
7.23.	$CO^+ + e^- + \#PR(B) + \#R\_F_2(S) \rightarrow CO + \#CF_2 + 2\#H_2 + \#CO + \#R(S)$	1.0	0.035	16.0	B
7.24.	$H^+ + e^- + \#PR(B) + \#R\_F_2(S) \rightarrow H + \#CF_2 + 2\#H_2 + \#CO + \#R(S)$	1.0	0.001	16.0	B
7.25.	$H_2^+ + e^- + \#PR(B) + \#R\_F_2(S) \rightarrow H_2 + \#CF_2 + 2\#H_2 + \#CO + \#R(S)$	1.0	0.0025	16.0	B
7.26.	$F^+ + e^- + \#PR(B) + \#R\_F_2(S) \rightarrow F + \#CF_2 + 2\#H_2 + \#CO + \#R(S)$	1.0	0.0235	16.0	B
7.27.	$Si^+ + e^- + \#PR(B) + \#R\_F_2(S) \rightarrow Si + \#CF_2 + 2\#H_2 + \#CO + \#R(S)$	1.0	0.035	16.0	B
7.28.	$SiF^+ + e^- + \#PR(B) + \#R\_F_2(S) \rightarrow SiF + \#CF_2 + 2\#H_2 + \#CO + \#R(S)$	1.0	0.0585	16.0	B
7.29.	$SiF_2^+ + e^- + \#PR(B) + \#R\_F_2(S) \rightarrow SiF_2 + \#CF_2 + 2\#H_2 + \#CO + \#R(S)$	1.0	0.0825	16.0	B
7.30.	$SiF_3^+ + e^- + \#PR(B) + \#R\_F_2(S) \rightarrow SiF_3 + \#CF_2 + 2\#H_2 + \#CO + \#R(S)$	1.0	0.106	16.0	B
	Ion assisted etch, CF_2 sites				
7.31.	$CF_3^+ + e^- + \#PR(B) + \#R\_CF_2(S) \rightarrow CF_3 + \#CF_2 + \#CO + 2\#H_2 + \#R\_C(S)$	1.0	0.069	16.0	B
7.32.	$CF_2^+ + e^- + \#PR(B) + \#R\_CF_2(S) \rightarrow CF_2 + \#CF_2 + \#CO + 2\#H_2 + \#R\_C(S)$	1.0	0.05	16.0	B

7.33.	$CF^+ + e^- + \#PR(B) + \#R\_CF_2(S) \rightarrow CF + \#CF_2 + \#CO + 2\#H_2 + \#R\_C(S)$	1.0	0.031	16.0	B
7.34.	$CHF_2^+ + e^- + \#PR(B) + \#R\_CF_2(S) \rightarrow CHF_2 + \#CF_2 + \#CO + 2\#H_2 + \#R\_C(S)$	1.0	0.051	16.0	B
7.35.	$CHF^+ + e^- + \#PR(B) + \#R\_CF_2(S) \rightarrow CHF + \#CF_2 + \#CO + 2\#H_2 + \#R\_C(S)$	1.0	0.032	16.0	B
7.36.	$O_2^+ + e^- + \#PR(B) + \#R\_CF_2(S) \rightarrow O_2 + \#CF_2 + \#CO + 2\#H_2 + \#R\_C(S)$	1.0	0.032	16.0	B
7.37.	$O^+ + e^- + \#PR(B) + \#R\_CF_2(S) \rightarrow O + \#CF_2 + \#CO + 2\#H_2 + \#R\_C(S)$	1.0	0.016	16.0	B
7.38.	$CO^+ + e^- + \#PR(B) + \#R\_CF_2(S) \rightarrow CO + \#CF_2 + \#CO + 2\#H_2 + \#R\_C(S)$	1.0	0.028	16.0	B
7.39.	$H^+ + e^- + \#PR(B) + \#R\_CF_2(S) \rightarrow H + \#CF_2 + \#CO + 2\#H_2 + \#R\_C(S)$	1.0	0.001	16.0	B
7.40.	$H_2^+ + e^- + \#PR(B) + \#R\_CF_2(S) \rightarrow H_2 + \#CF_2 + \#CO + 2\#H_2 + \#R\_C(S)$	1.0	0.002	16.0	B
7.41.	$F^+ + e^- + \#PR(B) + \#R\_CF_2(S) \rightarrow F + \#CF_2 + \#CO + 2\#H_2 + \#R\_C(S)$	1.0	0.019	16.0	B
7.42.	$Si^+ + e^- + \#PR(B) + \#R\_CF_2(S) \rightarrow Si + \#CF_2 + \#CO + 2\#H_2 + \#R\_C(S)$	1.0	0.028	16.0	B
7.43.	$SiF^+ + e^- + \#PR(B) + \#R\_CF_2(S) \rightarrow SiF + \#CF_2 + \#CO + 2\#H_2 + \#R\_C(S)$	1.0	0.047	16.0	B
7.44.	$SiF_2^+ + e^- + \#PR(B) + \#R\_CF_2(S) \rightarrow SiF_2 + \#CF_2 + \#CO + 2\#H_2 + \#R\_C(S)$	1.0	0.066	16.0	B
7.45.	$SiF_3^+ + e^- + \#PR(B) + \#R\_CF_2(S) \rightarrow SiF_3 + \#CF_2 + \#CO + 2\#H_2 + \#R\_C(S)$	1.0	0.085	16.0	B
	Ion assisted etch, H and CF_2 sites				
7.46.	$CF_3^+ + e^- + \#PR(B) + \#R\_H(S) + \#R\_CF_2(S) \rightarrow CF_3 + \#CHF_2 + \#CO + 2\#H_2 + \#R\_C(S) + \#R(S)$	1.0	0.069	16.0	B
7.47.	$CF_2^+ + e^- + \#PR(B) + \#R\_H(S) + \#R\_CF_2(S) \rightarrow CF_2 + \#CHF_2 + \#CO + 2\#H_2 + \#R\_C(S) + \#R(S)$	1.0	0.050	16.0	B
7.48.	$CF^+ + e^- + \#PR(B) + \#R\_H(S) + \#R\_CF_2(S) \rightarrow CF + \#CHF_2 + \#CO + 2\#H_2 + \#R\_C(S) + \#R(S)$	1.0	0.031	16.0	B
7.49.	$CHF_2^+ + e^- + \#PR(B) + \#R\_H(S) + \#R\_CF_2(S) \rightarrow CHF_2 + \#CHF_2 + \#CO + 2\#H_2 + \#R\_C(S) + \#R(S)$	1.0	0.051	16.0	B
7.50.	$CHF^+ + e^- + \#PR(B) + \#R\_H(S) + \#R\_CF_2(S) \rightarrow CHF + \#CHF_2 + \#CO + 2\#H_2 + \#R\_C(S) + \#R(S)$	1.0	0.032	16.0	B
	$O_2^+ + e^- + \#PR(B) + \#R\_H(S) + \#R\_CF_2(S) \rightarrow O_2 + \#CHF_2 + \#CO$	1.0	0.032	16.0	B

7.51.	$+2\#H_2 +\#R\_C(S)+\#R(S)$				
7.52.	$O^+ + e^- + \#PR(B) +\#R\_H(S) +\#R\_CF_2(S) \rightarrow O+\#CHF_2 +\#CO +2\#H_2 +\#R\_C(S)+\#R(S)$	1.0	0.016	16.0	B
7.53.	$CO^+ + e^- + \#PR(B) +\#R\_H(S) +\#R\_CF_2(S) \rightarrow CO+\#CHF_2 +\#CO +2\#H_2 +\#R\_C(S)+\#R(S)$	1.0	0.028	16.0	B
7.54.	$H^+ + e^- + \#PR(B) +\#R\_H(S) +\#R\_CF_2(S) \rightarrow H+\#CHF_2 +\#CO +2\#H_2 +\#R\_C(S)+\#R(S)$	1.0	0.001	16.0	B
7.55.	$H_2^+ + e^- + \#PR(B) +\#R\_H(S) +\#R\_CF_2(S) \rightarrow H_2+\#CHF_2 +\#CO +2\#H_2 +\#R\_C(S)+\#R(S)$	1.0	0.002	16.0	B
7.56.	$F^+ + e^- + \#PR(B) +\#R\_H(S) +\#R\_CF_2(S) \rightarrow F+\#CHF_2 +\#CO +2\#H_2 +\#R\_C(S)+\#R(S)$	1.0	0.019	16.0	B
7.57.	$Si^+ + e^- + \#PR(B) +\#R\_H(S) +\#R\_CF_2(S) \rightarrow Si+\#CHF_2 +\#CO +2\#H_2 +\#R\_C(S)+\#R(S)$	1.0	0.028	16.0	B
7.58.	$SiF^+ + e^- + \#PR(B) +\#R\_H(S) +\#R\_CF_2(S) \rightarrow SiF+\#CHF_2 +\#CO +2\#H_2 +\#R\_C(S)+\#R(S)$	1.0	0.047	16.0	B
7.59.	$SiF_2^+ + e^- + \#PR(B) +\#R\_H(S) +\#R\_CF_2(S) \rightarrow SiF_2+\#CHF_2 +\#CO +2\#H_2 +\#R\_C(S)+\#R(S)$	1.0	0.066	16.0	B
7.60.	$SiF_3^+ + e^- + \#PR(B) +\#R\_H(S) +\#R\_CF_2(S) \rightarrow SiF_3+\#CHF_2 +\#CO +2\#H_2 +\#R\_C(S)+\#R(S)$	1.0	0.085	16.0	B
7.61.	sputter of graphitized sites $CF_3^+ + e^- + \#R\_C(S) \rightarrow CF_3 + \#C + \#R(S)$	1.0	0.0086	40.0	B
7.62.	$CF_2^+ + e^- +\#R\_C(S) \rightarrow CF_2 + \#C + \#R(S)$	1.0	0.0063	40.0	B
7.63.	$CF^+ + e^- + \#R\_C(S) \rightarrow CF + \#C + \#R(S)$	1.0	0.0039	40.0	B
7.64.	$CHF_2^+ + e^- +\#R\_C(S) \rightarrow CHF_2 + \#C + \#R(S)$	1.0	0.0064	40.0	B
7.65.	$CHF^+ + e^- + \#R\_C(S) \rightarrow CHF + \#C + \#R(S)$	1.0	0.0040	40.0	B
7.66.	$O_2^+ + e^- + \#R\_C(S) \rightarrow O_2 + \#C + \#R(S)$	1.0	0.0040	40.0	B
7.67.	$O^+ + e^- + \#R\_C(S) \rightarrow O + \#C + \#R(S)$	1.0	0.0020	40.0	B
7.68.	$CO^+ + e^- + \#R\_C(S) \rightarrow CO + \#C + \#R(S)$	1.0	0.0035	40.0	B
7.69.	$H^+ + e^- + \#R\_C(S) \rightarrow H + \#C + \#R(S)$	1.0	0.0001	40.0	B

7.70.	$H_2^+ + e^- + \#R\_C(S) \rightarrow H_2 + \#C + \#R(S)$	1.0	0.0002	40.0	B
7.71.	$F^+ + e^- + \#R\_C(S) \rightarrow F + \#C + \#R(S)$	1.0	0.0024	40.0	B
7.72.	$Si^+ + e^- + \#R\_C(S) \rightarrow Si + \#C + \#R(S)$	1.0	0.0035	40.0	B
7.73.	$SiF^+ + e^- + \#R\_C(S) \rightarrow SiF + \#C + \#R(S)$	1.0	0.0059	40.0	B
7.74.	$SiF_2^+ + e^- + \#R\_C(S) \rightarrow SiF_2 + \#C + \#R(S)$	1.0	0.0083	40.0	B
7.75.	$SiF_3^+ + e^- + \#R\_C(S) \rightarrow SiF_3 + \#C + \#R(S)$	1.0	0.0106	40.0	B
	sputter of open sites				
7.76.	$CF_3^+ + e^- + \#PR(B) + \#R(S) \rightarrow CF_3 + 2\#H_2 + \#CO + \#R\_C(S)$	1.0	0.210	36.0	B [f]
7.77.	$CF_2^+ + e^- + \#PR(B) + \#R(S) \rightarrow CF_2 + 2\#H_2 + \#CO + \#R\_C(S)$	1.0	0.152	36.0	B [f]
7.78.	$CF^+ + e^- + \#PR(B) + \#R(S) \rightarrow CF + 2\#H_2 + \#CO + \#R\_C(S)$	1.0	0.094	36.0	B [f]
7.79.	$CHF_2^+ + e^- + \#PR(B) + \#R(S) \rightarrow CHF_2 + 2\#H_2 + \#CO + \#R\_C(S)$	1.0	0.155	36.0	B [f]
7.80.	$CHF^+ + e^- + \#PR(B) + \#R(S) \rightarrow CHF + 2\#H_2 + \#CO + \#R\_C(S)$	1.0	0.097	36.0	B [f]
7.81.	$O_2^+ + e^- + \#PR(B) + \#R(S) \rightarrow O_2 + 2\#H_2 + \#CO + \#R\_C(S)$	1.0	0.097	36.0	B [f]
7.82.	$O^+ + e^- + \#PR(B) + \#R(S) \rightarrow O + 2\#H_2 + \#CO + \#R\_C(S)$	1.0	0.049	36.0	B [f]
7.83.	$CO^+ + e^- + \#PR(B) + \#R(S) \rightarrow CO + 2\#H_2 + \#CO + \#R\_C(S)$	1.0	0.085	36.0	B [f]
7.84.	$H^+ + e^- + \#PR(B) + \#R(S) \rightarrow H + 2\#H_2 + \#CO + \#R\_C(S)$	1.0	0.0031	36.0	B [f]
7.85.	$H_2^+ + e^- + \#PR(B) + \#R(S) \rightarrow H_2 + 2\#H_2 + \#CO + \#R\_C(S)$	1.0	0.0061	36.0	B [f]
7.86.	$F^+ + e^- + \#PR(B) + \#R(S) \rightarrow F + 2\#H_2 + \#CO + \#R\_C(S)$	1.0	0.058	36.0	B [f]

[f] Yields scaled by ion mass, based on Graves' experimental data on Ar ion sputter of photoresist.

7.87.	$Si^+ + e^- + \#PR(B) + \#R(S) \rightarrow Si + 2\#H_2 + \#CO + \#R\_C(S)$	1.0	0.085	36.0	B [f]
7.88.	$SiF^+ + e^- + \#PR(B) + \#R(S) \rightarrow SiF + 2\#H_2 + \#CO + \#R\_C(S)$	1.0	0.143	36.0	B [f]
7.89.	$SiF_2^+ + e^- + \#PR(B) + \#R(S) \rightarrow SiF_2 + 2\#H_2 + \#CO + \#R\_C(S)$	1.0	0.201	36.0	B [f]
7.90.	$SiF_3^+ + e^- + \#PR(B) + \#R(S) \rightarrow SiF_3 + 2\#H_2 + \#CO + \#R\_C(S)$	1.0	0.259	36.0	B [f]

7.91. Comparisons with Experiment

For C_2F_6 plasma etch of photoresist, the experimental data available for mechanism development are etch rate data in Reactors II and IB.

For Reactor II, three sets of etch rate data, taken at different times, were available [20]. Figure 56 shows that, unfortunately, data for a certain set of conditions (1400 W plasma power, 6.5 mTorr, 40 sccm) in Data Set 1 turned out to be significantly lower than etch rates in Data Set 2 taken under the same conditions. This shows that, although the within-run uncertainty (indicated by the error bars) in the photoresist etch rates is estimated to be ~15%, the between-run uncertainty is much larger, on the order of a factor of 3 – 4. The magnitudes of the data in Set 3 were generally consistent with Data Set 2, although there were no overlapping sets of identical conditions for direct comparison. Data Set 1 preceded the others in time, so we chose to adjust the model to agree with the magnitude of the etch rates in Data Sets 2 and 3.

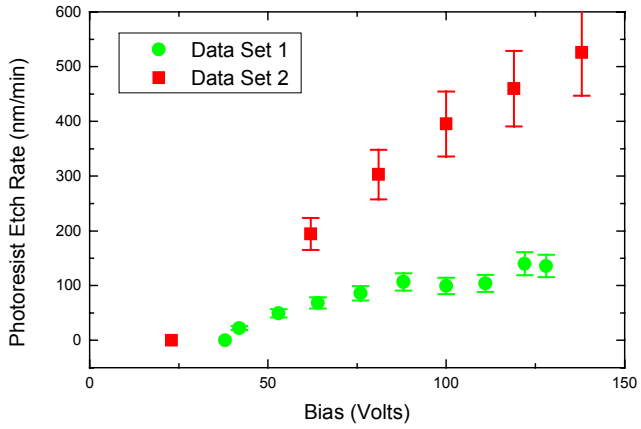

Figure 56. Photoresist etch rates from two data sets for C_2F_6 show large between-run uncertainties in Reactor II.

Figure 57 shows photoresist etch rates as a function of bias voltage for three different C_2F_6 flow rates in Reactor II, 1400 W, 6.5 mTorr. The simulations successfully reproduce the decrease in etch rate at lower bias, although the dependence is somewhat shallower than observed. The simulations also reproduce the small difference in etch rate between 30 sccm and 40 sccm, with a larger difference between 10 sccm and 30 sccm. These data are from Data Sets 2 and 3, so the model has been adjusted to match the general magnitudes of the etch rates. In contrast, the experiments in Figure 58 are from Data Set 1 (40 sccm), so the etch rates from the model are expected to be substantially higher. In Figure 58(a), the simulations successfully reproduce the observed lack of a power dependence between 1400 W and 600 W plasma power at 6.5 mTorr, along with the drop between 600 W and 400 W. At 20 mTorr, Figure 58(b), the simulations show more of a difference between 1400 W and 1000 W plasma power than is observed.

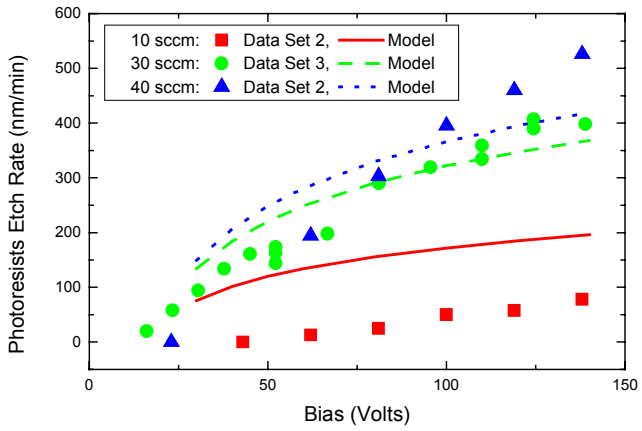

Figure 57. Photoresist etch rates for C_2F_6 as a function of bias power for three different flow rates in Reactor II. Data Sets 2 and 3, between-run uncertainty ×3-4.

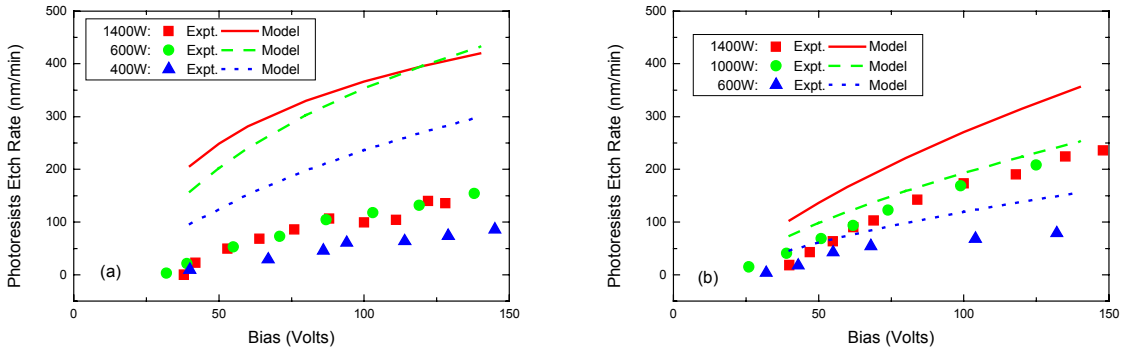

Figure 58. Photoresist etch rates for C_2F_6 as a function of bias power for three different powers in Reactor II. (a) 6.5 mTorr, (b) 20 mTorr. Data Set 1, between-run uncertainty ×3-4. Model expected to be high.

Figure 59 shows photoresist etch rates as a function of power and pressure plotted two ways for 30 sccm C_2F_6 and 100 V bias. These experiments are from Data Set 3, so the magnitudes of the etch rates in the simulations should match them. The comparisons between simulation and experiment in Figure 59 (a) and (b) for photoresist are quite similar to those shown for oxide etching in Figure 11 and Figure 12, respectively. Although many of the trends agree, the results of the simulations generally have much stronger dependencies than experiment, especially as a function of pressure.

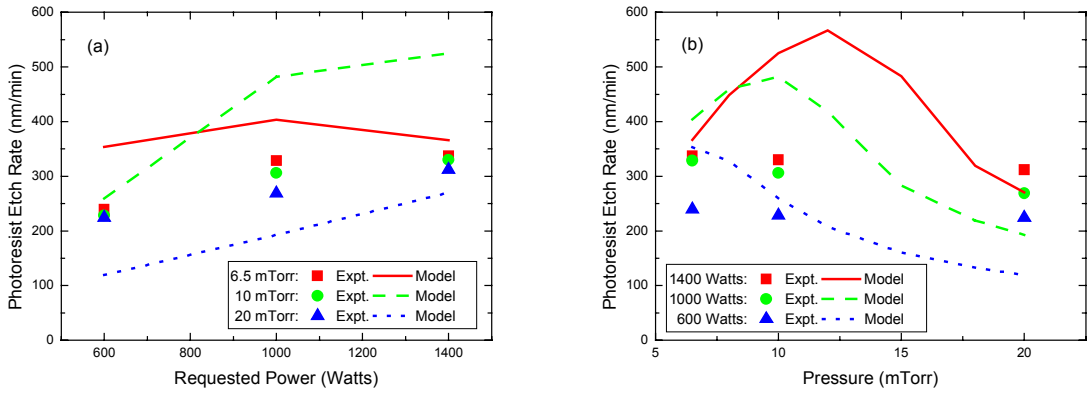

Figure 59. Photoresist etch rates for C_2F_6 as a function of (a) power and (b) pressure in Reactor II. Data Set 3, between-run uncertainty ×3-4.

Etch selectivities can be calculated for both experiment and model from the ratio of the oxide and photoresist etch rates. Figure 60 shows selectivities resulting from the oxide etch rates in Figure 11(b), Figure 12 and Figure 59, 30 sccm C_2F_6, 100 V bias, Reactor II. The selectivities from the simulations match experiment quite well in magnitude, and agree that there should be only a minor changes with power and pressure. For these selectivities, the models also tend to show smaller variations than experiment, in contrast with the comparisons for the underlying etch rates, where the model often showed much larger variations than experiment. In particular, both the oxide and photoresist etch rates showed substantial maxima in their pressure dependencies at high power, but the selectivity has a much smaller variation. This suggests that the cause of the discrepancies in the etch rate are rooted in an aspect of the simulations common to both oxide and photoresist etching, rather than a chemical reaction specific to one of the materials.

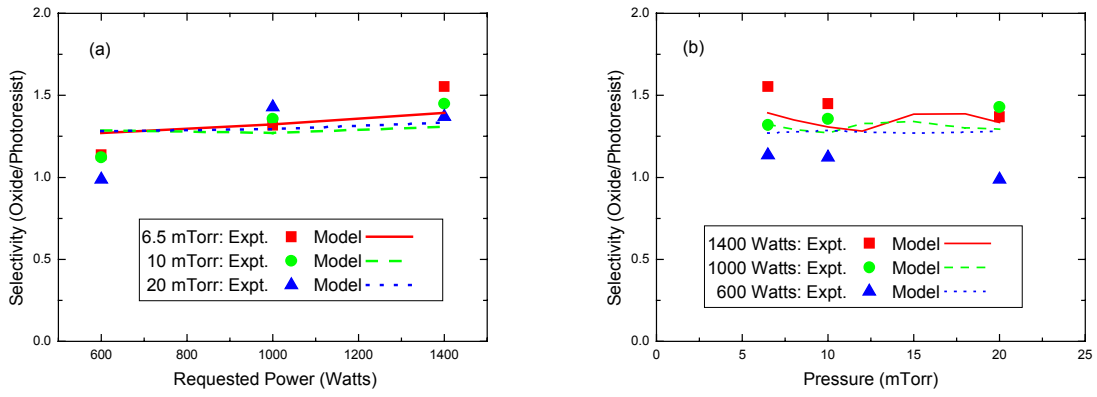

Figure 60. Selectivities for oxide etching over photoresist etching for C_2F_6 as a function of (a) power and (b) pressure in Reactor II. Data Set 3.

Figure 61 shows selectivities as a function of bias voltage for three different flow rates in Reactor II, 6.5 mTorr, 1400W, data sets 2 and 3. Selectivities are only calculated using etch rates from the same data set to avoid the complications of the large between-run uncertainties in the photoresist etch rates. In this case, model and experiment agree that the selectivity should decrease with increasing bias, and the magnitudes agree well at the higher flow rates. However, the experimental selectivities at 10 sccm are higher than those at the higher flows rates, whereas the simulations show very little dependence on flow rate (a ~20% decrease between 10 and 40 sccm). Note that the low bias experiments (and thus the simulations) were only done for 30 sccm.

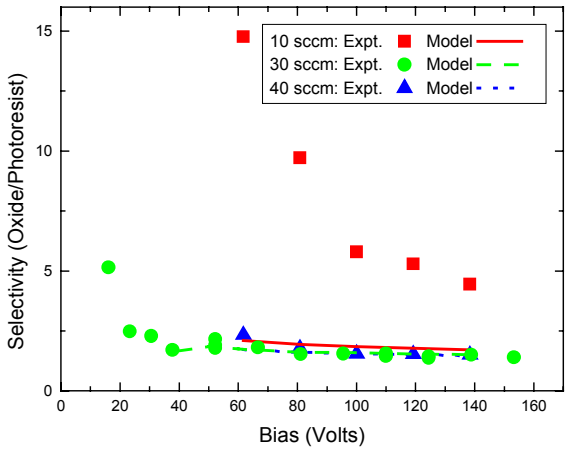

Figure 61. Selectivities for oxide etching over photoresist etching for C_2F_6 as a function of bias voltage in Reactor II. Data Sets 2 and 3.

For Reactor IB, photoresist etch rate data were available for blanket photoresist and patterned wafers over a range of conditions [15]. The data set for blanket photoresist is significantly larger, and thus received more attention. Figure 62 shows a comparison between model and experiment for blanket photoresist etch rates. The experimental conditions are the same as used for C_2F_6 plasma etch of oxide, and are listed in Table 6. Note that runs 8-13 are repeats of the same conditions, which gives some idea of the uncertainty in the experiments. Overall, the simulations agree quite well with experiment. For run 7, the lowest bias power point, the simulations give a finite etch rate, but it is too small to show up clearly on the plot.

Within this data set, there are subsets of runs that illustrate etch rate trends with specific variables. Figure 63(a) shows the photoresist etch rates as a function of plasma power, 15 mTorr, 85 Watts bias, 10 sccm. The simulations agree very well with the experiment in this case for both the absolute magnitude of the etch rates and the trend of decreasing etch rate with increasing power. Note that, as for other chemical systems in this report, the etch rates shown in Figure 59(a) for Reactor II show the opposite trend of increasing etch rate with increasing power. There are also four other data pairs where only the power is changed. In these cases, as the power is increased, the observed etch rates show trends of ↓↑↓↑ for these data pairs, whereas the simulations show ↓↓↓↓.

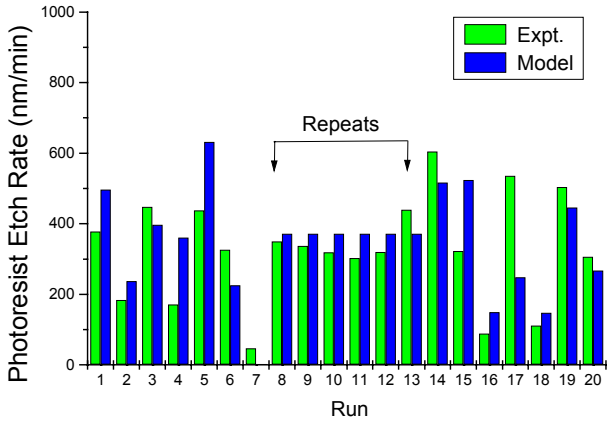

Figure 62. Blanket photoresist etch rate comparisons between model and experiment for C_2F_6 in Reactor IB. Experimental conditions given in Table 6. Data generally in order of increasing power.

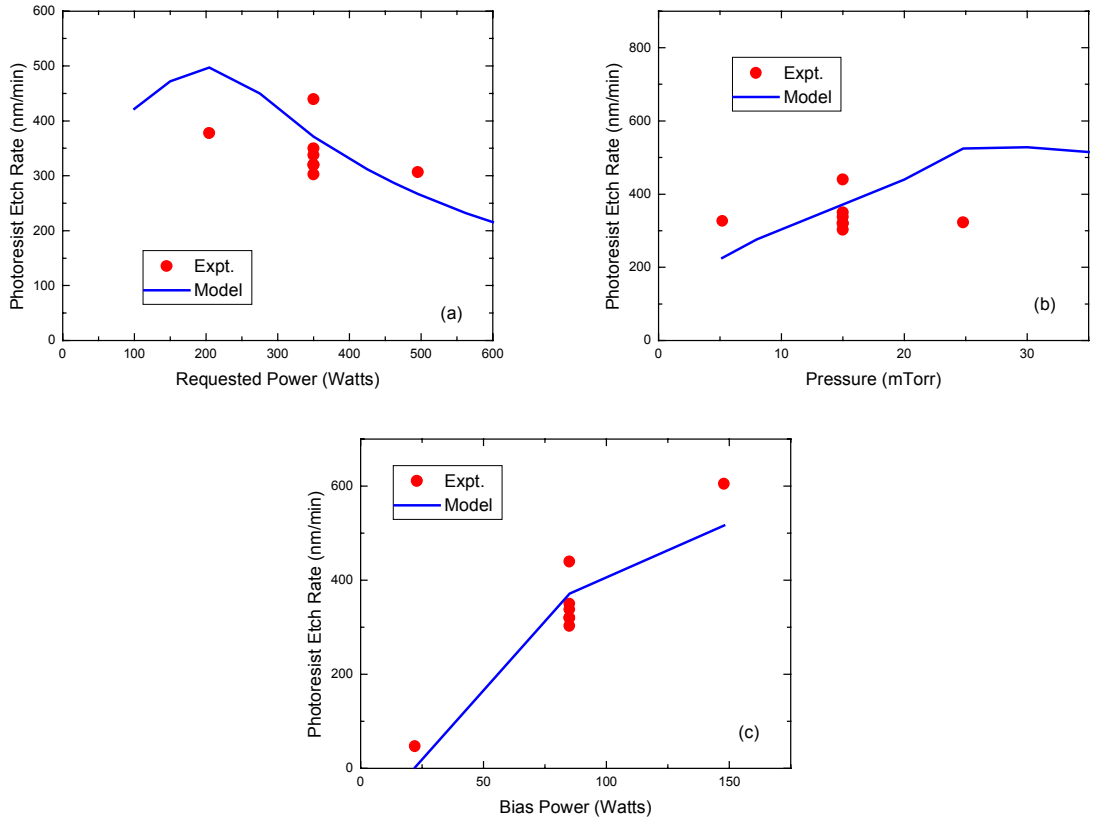

Figure 63. Blanket photoresist etch rates for C_2F_6 as a function of (a) plasma power, (b) pressure, and (c) bias power, in Reactor IB.

The agreement for the pressure dependence shown in Figure 63(b) is not as good as for the power dependence. The experiments are fairly independent of pressure while the model increases somewhat. There are also four other data pairs in which only the power is changed. In these cases, as the pressure is increased, the observed etch rates show no change for these data pairs, whereas the simulations show an increase or are flat. The agreement for the bias dependence shown in Figure 63(c) is excellent. In addition to the comparisons shown, there are four pairs of runs in which only the bias power differs. In all four cases, an increase in bias power is accompanied by a substantial increase in the etch rate.

For Reactor IB, etch rate data were also available for patterned wafers with 15% of the wafer open. Figure 64 shows comparisons between model and experiment for both the photoresist and oxide etch rates for this data set. The experimental conditions are given in Table 20.

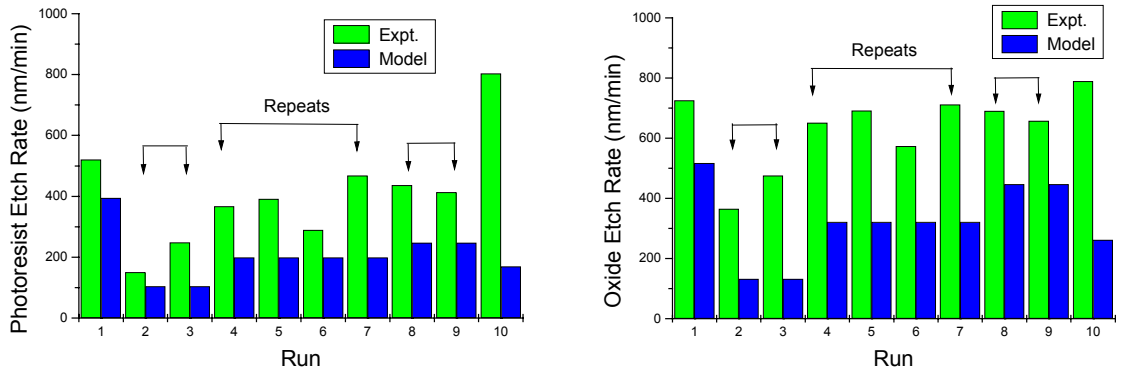

Figure 64. Patterned photoresist and oxide etch rate comparisons between model and experiment for C_2F_6 in Reactor IB. Experimental conditions given in Table 20. Data generally in order of increasing power.

Table 20. Conditions for C_2F_6 plasma etching of patterned photoresist and oxide shown in Figure 64 for Reactor IB.

Run No.	**Plasma Power** (Watts)	**Pressure** (mTorr)	**Bias Power** (Watts)
1	235	6	150
2-3	400	2	75
4-7	400	6	75
8-9	400	10	75
10	575	6	150

For these patterned wafers, the experimental etch rates are consistently higher than the simulations, even though the simulations and experiments agree quite well for blanket etch of these materials, as shown in Figure 6 for oxide and Figure 62 for photoresist. The disagreement could result from something wrong in either the experiments or the simulations. Simulations run for blanket etch of oxide and photoresist for the conditions in Table 20 give etch rates that are close (within 2% for photoresist and 10% for oxide) to those obtained for the patterned material. In the models, loading effects (reactant depletion) and the presence of different etch products thus appear to be too small to explain the observed disagreement. The discrepancy could also result from experimental between-run irreproducibility, of the sort seen in Figure 56 for photoresist etching in Reactor II. Unfortunately, there are no common sets of experimental conditions between Table 6 and Table 20, so direct comparisons between the experiments could not be made.

Although the patterned data set is smaller than the blanket data sets, there are a few cases where only one experimental parameter is altered. Figure 65 shows patterned photoresist etch rates as a function of (a) plasma power at 6.5 mTorr, 150 W bias power, and (b) pressure at 400 W plasma power, 75 W bias power. Figure 65(a) shows that the experimental etch rate increases with plasma power, whereas the simulations show a clear decrease, although the magnitude of the changes are comparable. In the case of the pressure dependence, Figure 65(b) for the patterned wafer shows that model and experiment agree that an increase in pressure will increase the etch rate, although the simulations are lower overall.

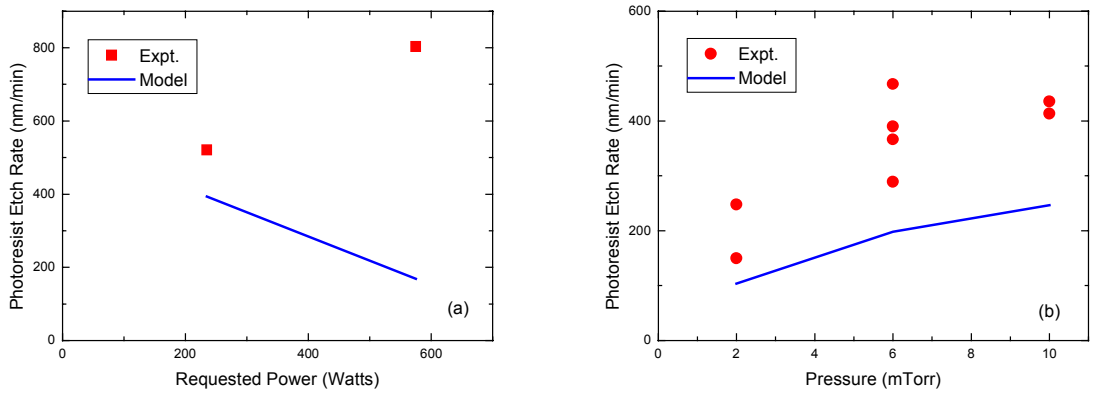

Figure 65. Patterned photoresist etch rates for C_2F_6 as a function of (a) plasma power, and (b) pressure, in Reactor IB.

A closer look at the blanket and patterned photoresist data, however, shows apparent disagreements amongst the experimental data itself. Figure 63(a) shows that blanket photoresist etch rates decrease with increasing plasma power in reactor IB, while Figure 65(a) shows patterned photoresist etch rates that increase with increasing plasma power in the same reactor. Likewise, the pressure dependence for blanket photoresist in Figure 63(b) shows very little dependence, whereas the patterned photoresist data in Figure 65(b) shows a clear increase.

These differences in experimental trends will be explored more below, and may be indicative of a chemical complexity that is not captured well by the current models.

Figure 66 shows the various sets of experimental photoresist etch rate data as a function of (a) plasma power and (b) pressure. This view of the data clearly shows that in Reactor IB, the experimental etch rates shift from a negative dependence on plasma power at low bias powers, to a positive dependence at high bias powers (explored in the patterned data only). Similarly, the pressure dependence is shown to be generally small, except at low pressures (explored in the patterned data only) where it is strongly positive. Thus, some of the differences observed between the blanket and patterned photoresist etch data can be explained by the different areas of parameter space covered by these data sets. Figure 67 shows experimental oxide etch rate data for Reactor IB plotted in the same manner. These data show many of the same features as the photoresist data, but not as clearly.

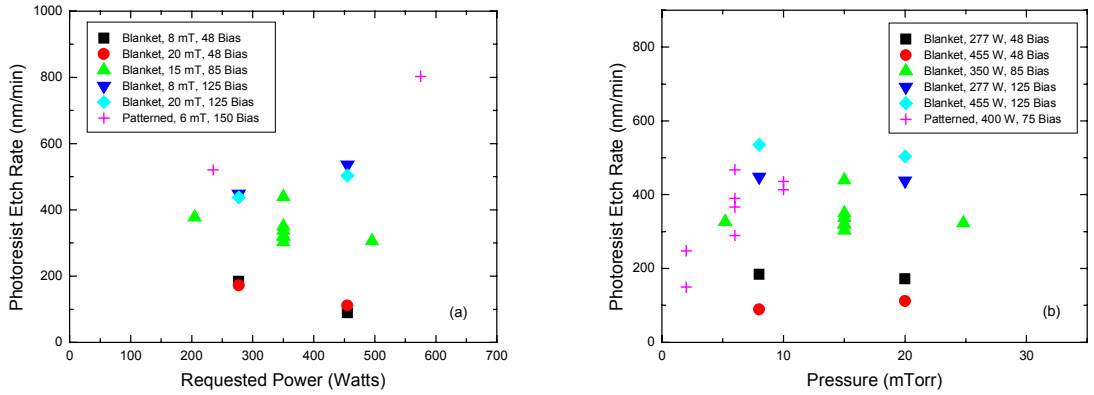

Figure 66. Experimental photoresist etch rates for C_2F_6 show different (a) power and (b) pressure dependencies at different conditions in Reactor IB.

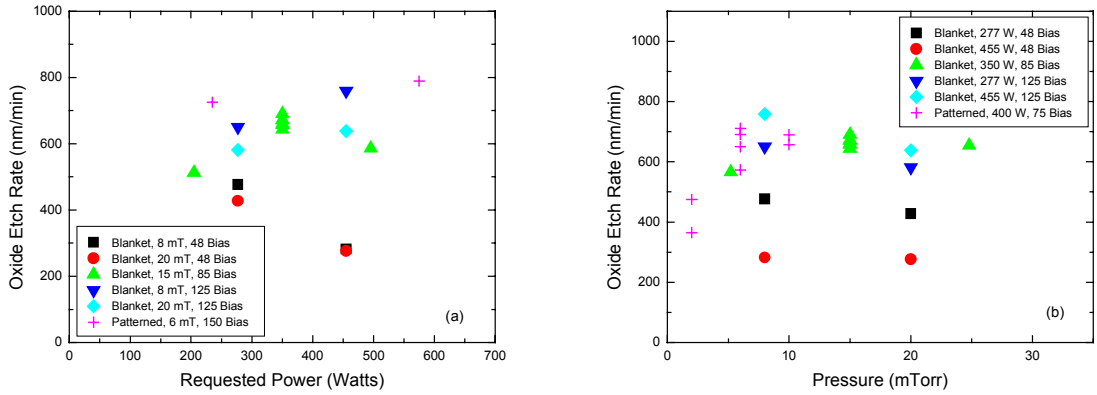

Figure 67. Experimental oxide etch rates for C_2F_6 show different (a) power and (b) pressure dependencies at different conditions in Reactor IB.

Figure 68 shows results of the photoresist simulations corresponding to the experimental data in Figure 66, while Figure 69 show oxide etch simulations corresponding to Figure 67. The simulations do not reproduce the shift from negative to positive plasma power dependencies observed in the experiments as the bias power increases, although there is a hint of it in Figure 69(a). The model does, however, show a shift from negative to positive plasma power dependencies at low plasma powers. For the pressure dependencies, the model primarily shows increasing etch rates with increasing pressures over most of the range covered by the experiments, with leveling-off or a change to a negative dependence occurring at much higher pressures than observed experimentally. The way in which trends depend on the values of other parameters points out the complexity of this system. These graphs suggest directions for further mechanism improvement, but that work falls outside the scope of this project.

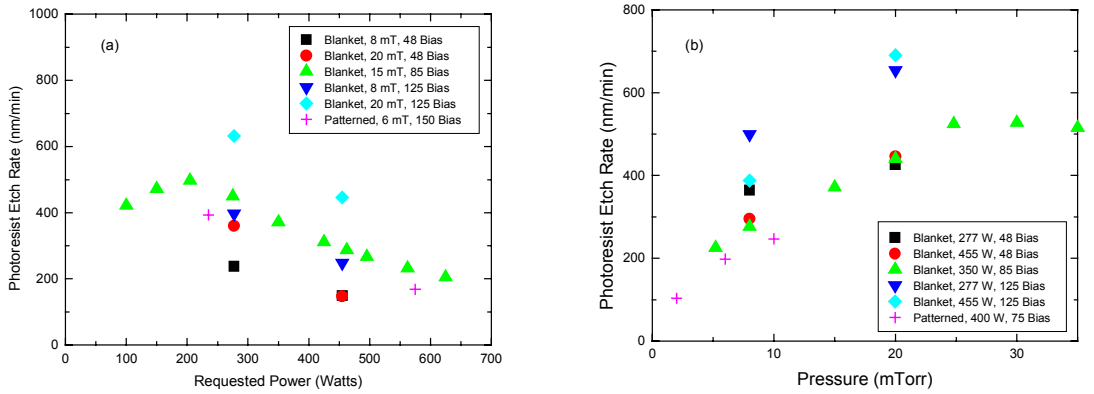

Figure 68. Simulated photoresist etch rates for C_2F_6 show less difference in (a) power and (b) pressure dependencies for different conditions in Reactor IB.

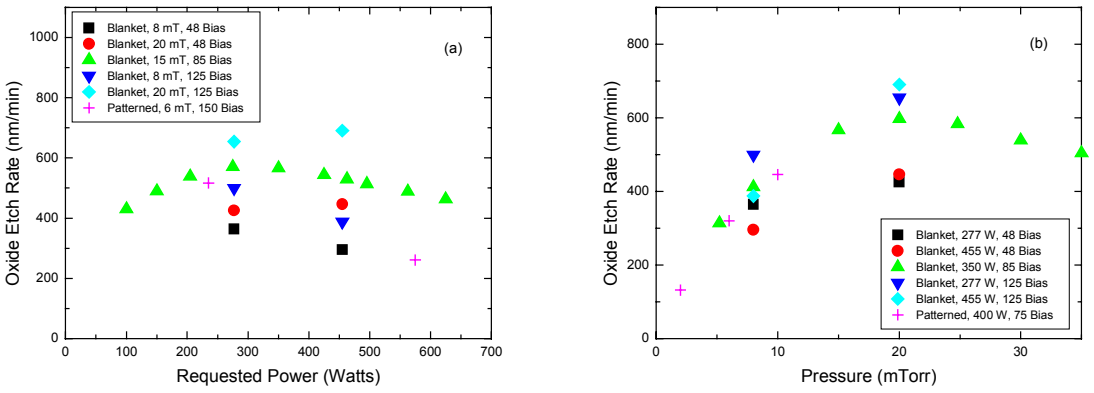

Figure 69. Simulated oxide etch rates for C_2F_6 show less difference in (a) power and (b) pressure dependencies for different conditions in Reactor IB.

Selectivities were also calculated for the etch rate data in Reactor IB. The blanket photoresist etch rates were compared with blanket oxide etch rates. For the patterned wafers, photoresist and oxide etch rates were taken from the same run.

Figure 70 shows selectivities based on the blanket etch rate data. The overall agreement between model and experiment is quite good. Note that the model result for Run 7 has been truncated in the plot; the calculated selectivity in this case was unphysically inflated by a very low photoresist etch rate obtained from the simulations for that run.

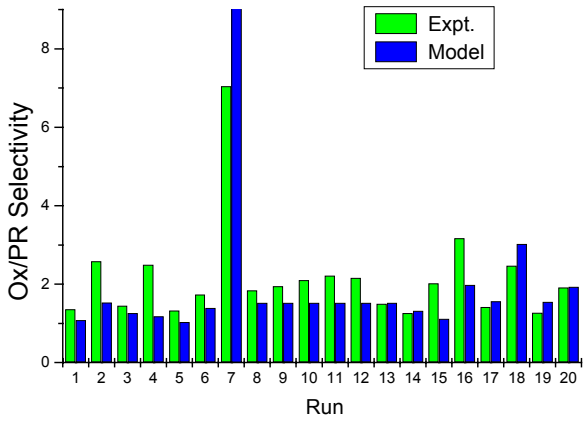

Figure 70. Selectivity comparisons between model and experiment for blanket wafers in C_2F_6, Reactor IB. Experimental conditions given in Table 6. Data generally in order of increasing power.

Figure 71 shows more detailed plots of the selectivity as a function of (a) plasma power, (b) pressure, and (c) bias power. These are derived from the data shown in Figure 7 through Figure 9 for oxide etching and Figure 63 for photoresist etching. The excellent agreement between model and experiment for the plasma power and bias power dependencies merely reflect the excellent agreement between model and experiment for the underlying etch rates. Note that the lowest bias point in Figure 71(c) is Run 7, where the raw selectivity from the simulations is actually much higher and has been truncated to keep the plot reasonable. The agreement between model and experiment for the pressure dependence is not quite as good as for the power and bias dependencies, and is comparable to the agreement between model and experiment for the underlying etch rates. For reactor IB, we did not see the kind of cancellation of errors that we saw in Figure 60 for Reactor II, where the agreement between model and experiment for the selectivities was much better than that for the etch rates.

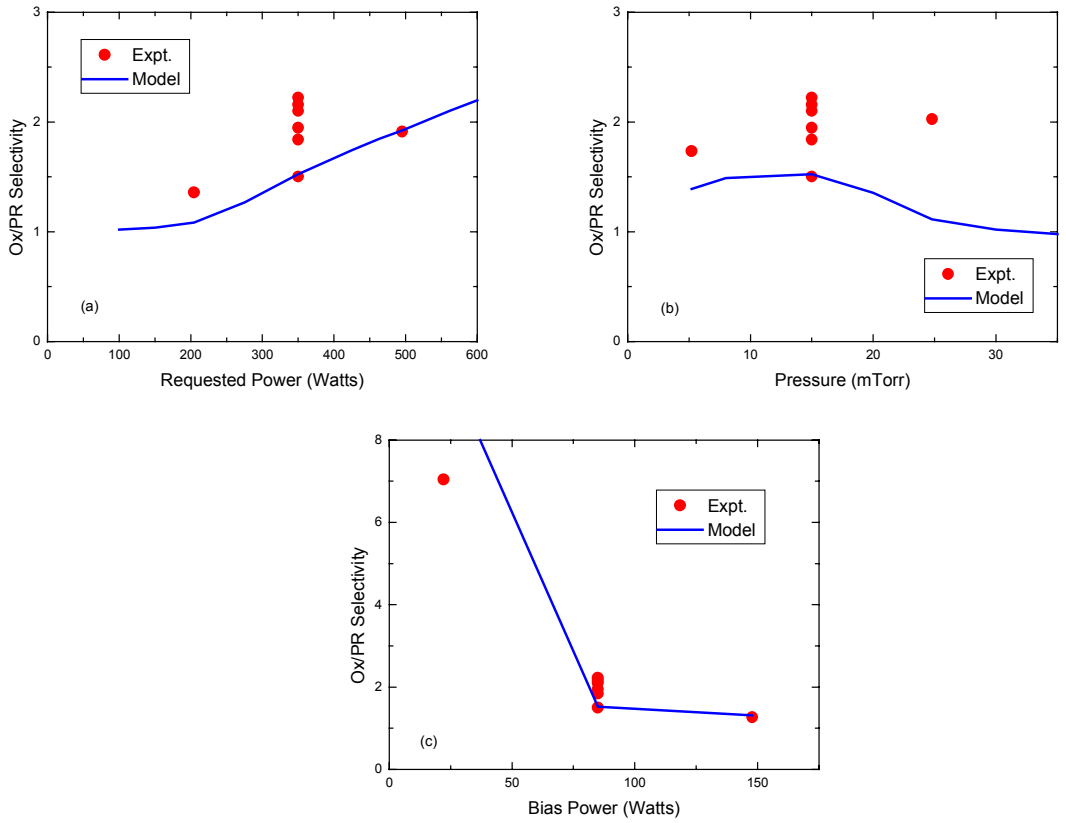

Figure 71. Selectivities for blanket wafers in C_2F_6, Reactor IB. Dependence on (a) plasma power, (b) pressure, and (c) bias power.

Figure 72 shows selectivities based on the patterned wafer etch rate data. Again, the overall agreement between model and experiment appears quite good. Figure 73 shows the cases where only one parameter was varied. In Figure 73(a), model and experiment disagree on the direction of the dependence on plasma power, although model and experiment agree well for the corresponding case in Figure 71(a) for the blanket etches. This just reflects the disagreement seen for the photoresist etch rates in Figure 65(a). This is one of the cases, discussed above, where the experimental trends in the blanket and patterned etch rates disagreed, possibly because of differences in the other operating parameters. The pressure dependence in Figure 73(b) shows disagreement between model and experiment; the experimental selectivity decreases slightly with increasing pressure, while the simulations show a slight increase. The patterned wafer data were taken at generally lower pressures than the blanket wafer data, but we note that Figure 71(b) suggests increasing etch rates with increasing pressure for both model and experiment at the lower pressures.

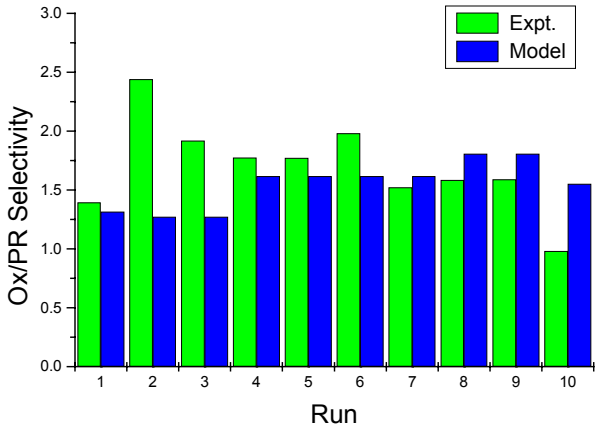

Figure 72. Selectivity comparisons between model and experiment for patterned wafers in C_2F_6, Reactor IB. Experimental conditions given in Table 20. Data generally in order of increasing power.

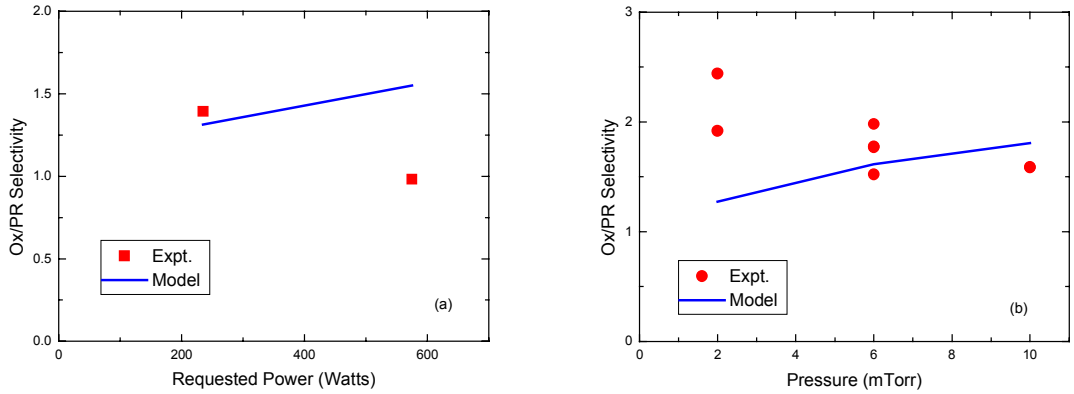

Figure 73. Selectivities for patterned wafers in C_2F_6, Reactor IB. Dependence on (a) plasma power and (b) pressure.

8. CHF_3 Etch of Photoresist

There is a small amount of experimental etch rate data for CHF_3 plasma etch of photoresist in Reactor II [20], so simulations were done for comparisons. The reaction mechanism used is exactly the same as used for C_2F_6 plasma etch of photoresist, described in section 7.1. No fitting was done to this set of data; the reaction mechanism in Table 19 was fit to the C_2F_6 photoresist etch data only. These simulations thus represent an extension of the model to new territory.

Figure 74 shows photoresist etch rates as a function of plasma power for three different combinations of pressure and CHF_3 flow rate at 100 V Bias. These data correspond to Data Set 2 for C_2F_6 plasma etching of photoresist, discussed in section 7.2, so it is significant that the simulations reproduce the magnitude of the etch rates, even though there is evidence for a large between-run uncertainty in the experimental values. The simulations do not reproduce the "humped" power dependence seen in these experimental data sets, although it might be able to be reworked to do so, as the simulations show both positive and negative power dependencies at different conditions.

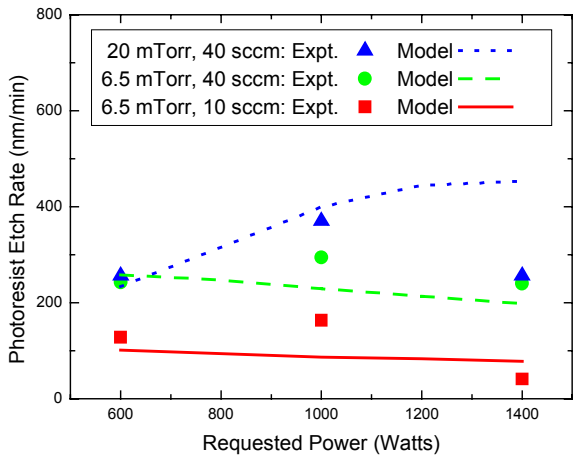

Figure 74. Photoresist etch rates for CHF_3 as a function of power for different pressures and flow rates in Reactor II. Data Set 2, between-run uncertainty ×3-4.

Figure 75 shows selectivities calculated from the photoresist etch rates shown in Figure 74 and oxide etch rates shown in Figure 32. For the CHF_3 etching of oxide, there are two sets of measurements, leading to two sets of experimental selectivities. These are indicated by open and closed points, and give some idea of the experimental reproducibility. The simulations successfully reproduce the general magnitudes of the selectivities, as well as the trend of increasing selectivity with increasing power and the general order of the data. They do not, reproduce the large increase in selectivity observed at high plasma power, low pressure and low flow rate.

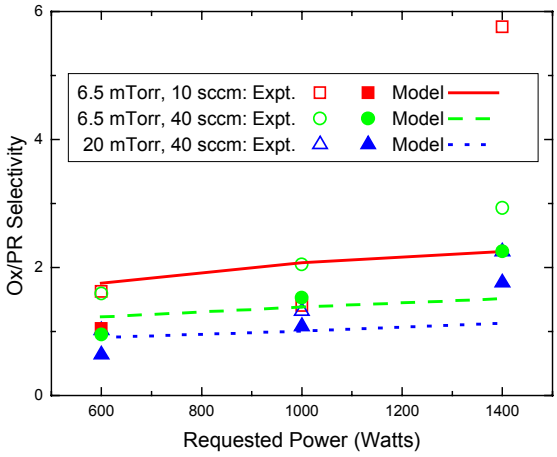

Figure 75. Selectivities for CHF_3 as a function of power for different pressures and flow rates in Reactor II. Open and closed symbols represent older and newer set of data.

9. C_4F_8 Etch of Low-k Dielectrics

The silicon semiconductor industry is now exploring dielectric materials that have lower dielectric constants (k) than silicon dioxide. A wide variety of organic and inorganic materials are being considered, including porous silica materials. The latter are chemically closely related to silicon dioxide, although they are often applied as a liquid and generally contain organic ligands such as ethoxy or methoxy groups. They are being etched with many of the same fluorocarbon plasma reactors and processes that have developed for oxide etching.

As a first exploration of low-k dielectric etching, we treat these porous materials as if they were stoichiometric SiO_2, as the suppliers do not provide quantitative information on the elemental composition of the material. In the simulations, we use the reaction mechanism described in section 6 for C_4F_8 etch of silicon dioxide with no changes, and alter only the density of the material being etched to reflect the reported porosity.

These simulations, though very simplified, give an idea of the extent to which the chemistry of these materials are dominated by their silica character. Areas of disagreement may be indicative either of the effects of hydrocarbon groups in these films, or of their very high surface area to volume ratios, which also are not accounted for in these simulations.

For this system, we have only a limited number of etch rate measurements in Reactors IB and II, and no diagnostic measurements, for comparison with the simulations. Figure 76 shows etch rates in Reactor IB [15] as a function of bias power (26 sccm C_4F_8, 15 mTorr, 400 W plasma power) for two different porous silica materials: (a) a material labeled B56 with 40% porosity, and (b) a material labeled PPO/P123 hydroxylated with 50% porosity. Note that the negative experimental etch rates indicate that polymer deposition from the plasma is occurring rather than etching. The simulations do a surprisingly good job of reproducing the general magnitude of the etch rates and the general trend, given the level of approximation involved. Also remember that the reaction mechanism for the C_4F_8 plasma etch of oxide was developed to give etch rates that were higher than experiment for Reactor IB, and lower than experiment for Reactor II.

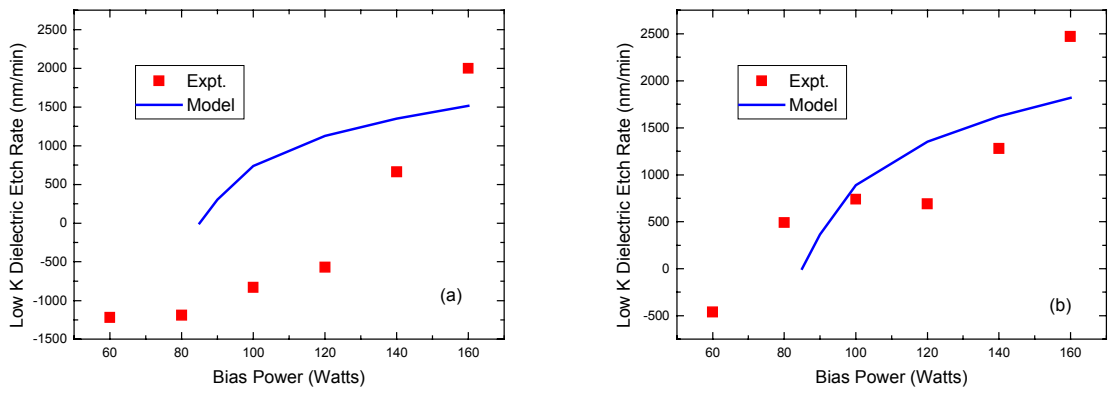

Figure 76. Low-k dielectric etch rate dependence for C_4F_8 in Reactor IB. (a) 40% porosity (b) 50% porosity.

Figure 77 shows etch rates in Reactor II [20] as a function of gas mixture (40 sccm total of C_4F_8 + O_2, 1400 W,-100 V bias) for two different low-k dielectric materials with (a) 67% porosity, and (b) 41% porosity, as well as (c) silicon dioxide. Gas mixture dependencies were generally not included in the mechanism development and validation process (although Figure 23 includes some data for SiF as a function of gas mixture for C_2F_6 etch of oxide), so this represents an extension of the model into a new region of parameter space. The simulations show the anticipated overall decrease in etch rate as the C_4F_8 is replaced by O_2. The fact that the simulations give lower overall etch rates than experiment for all three cases is to be expected, given the way the mechanism was built. The experimental data in (a) clearly show a peak in the etch rates for the low-k materials that is not seen in the oxide etch rates in (c). Although the model shows something of a maximum at ~40% O_2 for 20 mTorr, this feature is not evident at 6.5 mTorr, and is present for both the porous materials and the oxide at the higher pressure. This represents a real difference between these materials that the simulations do not reproduce.

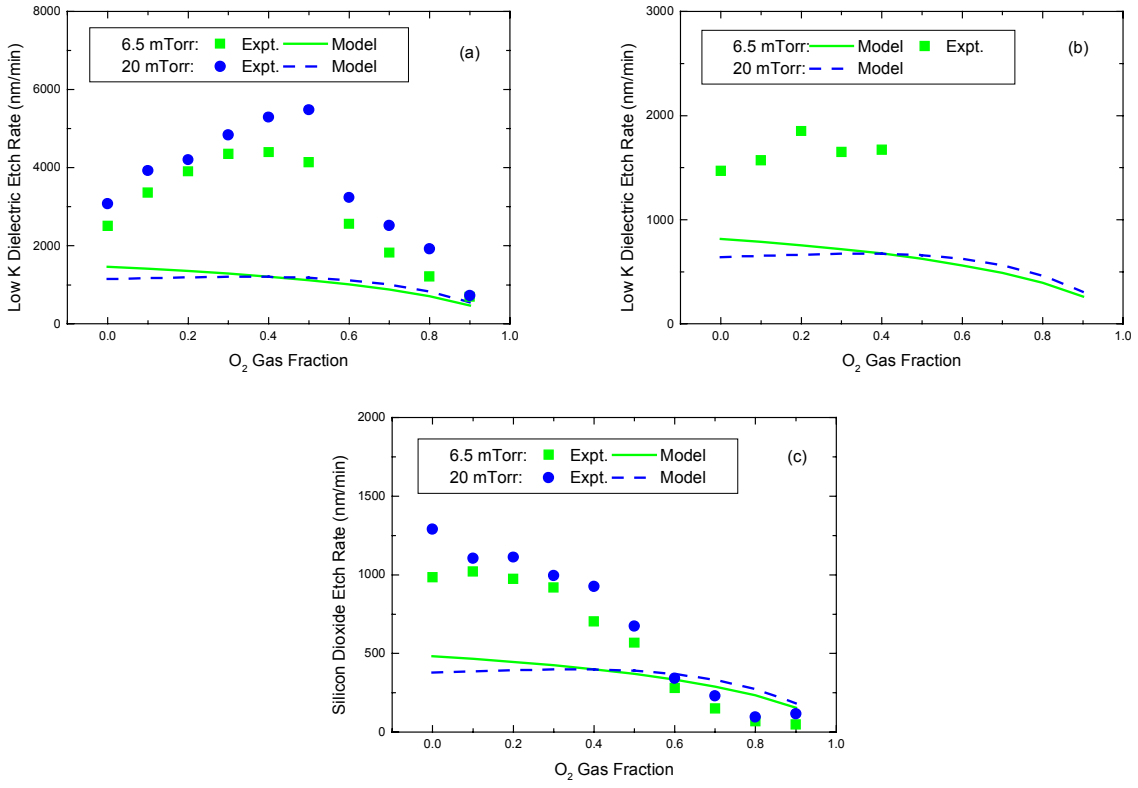

Figure 77. Etch rate dependence for C_4F_8 in Reactor II on O_2 gas fraction. (a) 67% porosity low-k dielectric, (b) 41% porosity low-k dielectric, (c) silicon dioxide.

10.Summary

We have developed a detailed set of gas-phase and surface chemical reaction mechanisms that describe a variety of fluorocarbon plasma etching processes. These mechanisms were developed using and tested against experimental etch rate data in three different reactors as well as a number of diagnostic measurements using 0D simulations. The diagnostic experiments included measurements of absolute electron and negative ion densities, relative densities measurements of CF, CF_2, SiF and SiF_2 radical species, gas temperatures, ion current densities, and mass spectrometric measurements of relative ion densities.

The core of the chemistry is contained in the reaction mechanism for the C_2F_6 plasma etching of silicon dioxide. This mechanism includes 28 gas-phase species and 132 gas-phase reactions, plus surface reactions for both silicon and oxide surfaces that involves 6 surface species and 85 surface reactions. The gas phase reactions include electron impact reactions (vibrational and electronic excitation, ionization, dissociation, dissociative ionization, and dissociation attachment) as well as electron attachment, charge exchange and ion-neutralization reactions. The surface reactions include direct etching by F atoms, adsorption of atoms and radicals, ion-enhanced etching by all positive ions in the system, ion neutralization on open sites, ion deposition, ion sputtering, and radical abstraction of surface species. Additional sets of gas and surface reactions are added to this base set of reactions to extend the mechanism to CHF_3 or C_4F_8 plasmas, or to the etching of photoresist.

The simulations compare very well to the experimental measurements over a broad range of parameter space. They can reproduce many, but not all of the measured quantities and trends. These plasma systems are quite complex, however, with apparently contradictory trends being reported for different plasma reactors (i.e. opposite directions for etch rate dependencies on a parameter such as plasma power), so it is not surprising that not all of the experimental measurements can be matched. In some cases, worse fits to a particular set of experiments were accepted in order to achieve a better fit to the overall set of data.

The models give a number of insights into the chemistry occurring in these plasma systems, some of which are listed here. 1) The preponderance of the input gases (C_2F_6, CHF_3, or C_4F_8) are dissociated by the plasma, so it is important to include a fairly complete set of reactions for these fragments. This also means that most of the molecules in the plasma that collide with the surfaces will be reactive radicals rather than the starting species. 2) Etch products can represent a significant fraction of the molecules in the gas phase, so it is important to include electron impact reactions for such species in order to get the correct plasma behavior. 3) Ion-assisted reactions involving surface fluorine and surface fluorocarbon species are responsible for SiO_2 etching – spontaneous etching by F atoms is not important. Depending on the reactor and conditions being used, the etch rate can either be limited by the flux of ions on the surface (strongly bias dependent), or limited by the supply of etchant species (strongly gas-flow rate dependent). 4) F atoms are formed by a multitude of reaction pathways in these plasmas – there is no "dominant pathway". In particular, electron impact dissociation of the SiF_x etch products can represent a significant source of "recycled" F atoms for further etching. 5) C_4F_8 plasmas are much more polymerizing than C_2F_6 or CHF_3 plasmas, so additional reactions of C_2F_4 surface species were needed to reproduce the observed etch rate behaviors. 6) For photoresist etching,

the simulations are limited by the simplified treatment of the materials as well as the large between-run uncertainties in some of the experimental data sets used to develop the models. Nonetheless, the simulations were sometimes able to reproduce selectivities better than the underlying etch rates. 7) Treating silica-based low-k dielectric materials as reduced-density SiO_2 is too simplified a treatment. Better simulations may need either to explicitly address the high surface area to volume ratio of these materials, or to account for the presence of organic groups (ethoxy or methoxy groups) in the material.

The success of these simulations show that it is possible to model these complex plasma systems with an approach based on the underlying fundamental chemistry and physics. Our work on C_2F_6, CHF_3 and C_4F_8 plasma etch of oxide is clearly more complete and mature than the work on photoresist etching, and the work on low-k dielectrics is at a very preliminary stage. The modular nature of the mechanisms shows how they can serve as a firm foundation for future work on related systems.

References

1. P. Ho, J. E. Johannes, R. J. Buss, and E. Meeks, submitted to JVSTA.

2. E. Meeks and P. Ho, Thin Solid Films **365,** 334 (2000).

3. E. Meeks and P. Ho, "Plasma Modeling", Chapter 3 in "Advanced Plasma Processing Technologies", edited by R. J. Shul and S. J. Pearton, Springer-Verlag, Heidelberg, (2000).

4. R. J. Kee, F. M. Rupley, J. A. Miller, M. E. Coltrin, J. F. Grcar, E. Meeks, H. K. Moffat, A. E. Lutz, G. Dixon-Lewis, M. D. Smooke, J. Warnatz, G. H. Evans, R. S. Larson, R. E. Mitchell, L. R. Petzold, W. C. Reynolds, M. Caracotsios, W. E. Stewart, and P. Glarborg, , "Chemkin Collection, vers. 3.02", Reaction Design, Inc., (1997).

5. M. W. Chase, C. A. Davies, J. R. Downey, D. J. Frurip, R. A. McDonald, and A. N. Syverud, *J. Phys. Chem. Ref. Data, Supplement No. 1 ,* **14,** 1 (1985) .

6. B. McBride, S. Gordon, and M. Reno, "CET/93PC, Chemical Equilibrium with Transport Properties", NASA Lewis Research Center, 1993. Available from COSMIC, the NASA Software Technology Transfer Center.

7. E. Meeks and J. W. Shon, IEEE Trans. Plasma Sci. **23**, 539 (1995).

8. E. Meeks, H. K. Moffat, J. F. Grcar and R. J. Kee, "AURORA: A Fortran Program for Modeling Well Stirred Plasma and Thermal Reactors with Gas and Surface Reactions", Sandia National Laboratories Report SAND96-8218, 1996.

9. P. A. Miller, G. A. Hebner, K. E. Greenberg, P. D. Pochan, and B. P. Aragon, J. Resch. Natl. Int. Standard. Technol. **100,** 427 (1995).

10. P. J. Hargis Jr., K. E. Greenberg, P. A. Miller, J. B. Gerardo, J. R. Torczynski, M. E. Riley, G. A. Hebner, J. R. Roberts, J. K. Olthoff, J. R. Whetstone, R. J. Van Brunt, M. A. Sobolewski, H. M Anderson, M. P. Splichal, J. L. Mock, P. Bletzinger, A. Garscadden, R. A. Gottscho, G. Selwyn, M. Dalvie, J. E. Heidenreich, J. W. Butterbaugh, M. L. Brake, M. L. Passow, J. Pender, A. Lujan, M. E. Elta, D. B. Graves, H. H. Sawin, M. J. Kushner, J. T. Verdeyen, R. Horwath, and T. R. Turner, Rev. Sci. Inst. **65,** 140 (1994).

11. G. A. Hebner and P. A. Miller, J. Appl. Phys., **87,** 7660 (2000).

12. G. A. Hebner, J. Appl. Phys., **89,** 900 (2001).

13. G. A. Hebner and I. C. Abraham, "Characterization of Electron and Negative Ion Density in Fluorocarbon Containing Inductively-Driven Plasma", submitted to J. Appl. Phys.

14. G. A. Hebner, "Spatially Resolved SiF and SiF_2 Densities in Inductively Driven Discharges Containing C_2F_6 and C_4F_8", submitted to J. Appl. Phys.

15. W. L. Perry, K. Waters, M. Barela, G. Van Ullen, and H. M. Anderson, in preparation. H. M. Anderson, private communication.

16. Karla Water, "Infrared Diode Laser Absorption Spectroscopy Measurement of Gas Phase Radicals in C_4F_8 Discharges for Plasma Model Validation", Masters Thesis in Chemical Engineering, University of New Mexico, 2000.

17. T. E. F. M. Standaert, M. Schaepkens, N. R. Rueger, P. G. M. Sebel, and G. S. Oehrlein, J. Vac. Sci. Technol. A **16**, 239 (1998).

18. M. Schaepkens, T. E. F. M. Standaert, N. R. Rueger, P. G. M. Sebel, G. S. Oehrlein, and J. M. Cook, J. Vac. Sci. Technol. A **17,** 26 (1999).

19. E. Meeks, P. Ho, A. Ting and R. J. Buss, J. Vac. Sci. Technol. A **16**, 2227 (1998).

20. G. S. Oehrlein and coworkers, private communication.

21. L. G. Christophorou and J. K. Olthoff, J. Phys. Chem. Ref. Data **27,** 1 (1998).

22. M. Hayashi, *Gaseous Dielectrics V,* edited by L. Christophorou and D. Bouldin, (Pergamon, New York, 1987).

23. H. U. Poll and J. Meichsner, Contrib. Plasma Phys. **27,** 359 (1987).

24. L. G. Christophorou, J. K. Olthoff, and M. V. V. S. Rao, J. Phys. Chem. Ref. Data **25,** 1341 (1996).

25. V. McKoy, private communication.

26. W. L. Morgan, Kinema Corporation, private communication.

27. V. Tarnovsky, P. Kurunczi, D. Rogozhinikov and K. Becker, Int. J. Mass. Spectrom. Ion Processes **128,** 181 (1993).

28. R. J. W. Henry, P. G. Burke, and A.-L. Sinfailam, Phys. Rev. **178,** 218 (1969).

29. K. S. Baliyan and A. K. Bhatia, Phys. Rev. A **50,** 2981 (1994).

30. T. R. Hayes, R. C. Wetzel and R. S. Freund, Phys. Rev. A **35,** 578 (1987).

31. Nagpal, Garscadden, Liptak and Clark, unpublished data, as cited by W. L. Morgan.

32. T. R. Hayes, R. J. Shul, R. A. Baiocchi, R. C. Wetzel and R. S. Freund, J. Chem. Phys. **89,** 4035 (1988).

33. R. J. Shul, T. R. Hayes, R. C. Wetzel, R. A. Baiocchi and R. S. Freund, J. Chem. Phys. **89,** 4042 (1988).

34. T. R. Hayes, R. C. Wetzel, R. A. Baiocchi and R. S. Freund, J. Chem. Phys. **88,** 823 (1988).

35. Y. Itikawa, A. Ichimura, K. Onda, K. Sakimoto, K. Takayanagi, Y. Hatano, M. Hayashi, H. Nishimura, and S. Tsurubuchi, J. Phys. Chem. Ref. Data **18,** 23 (1989).

36. S. A. Lawton and A. V. Phelps, J. Chem. Phys. **69,** 1055 (1978); A. V. Phelps, Collision Data Compilation, http://jilawww.colorado.edu/www/research/colldata.html

37. P. C. Cosby, J. Chem. Phys. **98,** 9560 (1993).

38. Y. Itikawa and A. Ichimura, J. Phys. Chem. Ref. Data **19,** 637 (1990).

39. J. E. Land, J. Appl. Phys. **49,** 5716 (1976).

40. P. C. Cosby, J. Chem. Phys. **98,** 7804 (1993).

41. D. Rapp and P. Englander-Golden, J. Chem. Phys. **43,** 1464 (1965).

42. V. G. Anicich, J. Phys. Chem. Ref. Data **22,** 1469 (1993).

43. B. M. Smirnov, *Negative Ions,* (McGraw-Hill, New York, 1982).

44. D. L Flamm, V. M. Donnelly, and J. A. Mucha, J. Appl. Phys. **52,** 3633 (1981).

45. D. L. Flamm, C. J. Mogab, and E. R. Sklaver, J. Appl. Phys. **50,**. 6211 (1979).

46. D. C. Gray, I. Tepermeister, and H. H. Sawin, J. Vac. Sci. Technol. B **11,** 1243 (1993).

47. J. W. Butterbaugh, D. C. Gray and H. H. Sawin, J. Vac. Sci. Technol. B **9,** 1461 (1991).

48. J. C. Greaves and J. W. Linnett, Trans. Faraday Soc. **54,** 1323 (1958).

49. Ganesh Rajagopalan, SEMATECH, private communication.

50. R. Jayaraman, R. T. McGrath, and G. A. Hebner, J. Vac. Sci. Technol. A **17**, 1545 (1999).

51. I. C. Abraham, *Infrared Absorption Spectroscopy of Neutral Fragment Molecules and Other Species in Halocarbon Plasma Discharges*, PhD Thesis, University of Wisconsin-Madison, 1999.

52. W. L. Perry, H. M. Anderson, M. Schaepkens, G. S. Oehrlein, I. Abraham, and C. Woods, in preparation.

53. M. J. Kushner and D. Zhang, J. Appl. Phys. **88,** 3231 (2000).

54. R. K. Janev, W. D. Langer, K. Evans, Jr., and D. E. Post, Jr., *Elementary Processes in Hydrogen-Helium Plasmas,* (Springer-Verlag, NewYork, 1987).

55. H. Yasuda, *Plasma Polymerization*, Academic Press, Orlando, 1985.

56. R. J. Buss, J. Appl. Phys, **59,** 2977 (1986).

57. F. Greer, J. W. Coburn, and D. B. Graves, private communication.